Statistical methods for ambient noise characterisation, modelling and suppression: theory and applications for surface microseismic monitoring.

Claire Emma Birnie

Submitted in accordance with the requirements for the degree of
Doctor of Philosophy

The University of Leeds
School of Earth and Environment

May 2018

The candidate confirms that the work submitted is her own, except where work which has formed part of jointly authored publications has been included. The contribution of the candidate and the other authors to this work has been explicitly indicated below. The candidate confirms that appropriate credit has been given within the thesis where reference has been made to the work of others . The Journals' permission and copyright information is supplied in Appendix A.

The work in Chapter 2 of the thesis has appeared in publication as follows:
Birnie, C., Chambers, K., Angus, D. and Stork, A.L., 2016. Analysis and models of pre-injection surface seismic array noise recorded at the Aquistore carbon storage site. *Geophysical Journal International*, 206(2), pp.1246-1260. doi:10.1093/gji/ggw203

The concepts and methodologies used in this paper were conceived and matured with the support of the co-authors. I performed the data processing and noise analysis, implemented the noise modelling methodology, and wrote the manuscript. Both the investigative research and the manuscript were improved through the comments and suggestions of the co-authors.

The work in Chapter 3 of the thesis is a manuscript under review :
Birnie, C., Chambers, K., Angus, D, and Stork, A., *under review*, Effect of noise on microseismic event detection and imaging procedures using ICOVA statistical noise modelling method. *Journal of Applied Geophysics*

The ideas and methodologies used in this paper were developed alongside the co-authors. I generated the synthetic datasets, performed the data processing and analysis, and wrote the manuscript. Both the investigative research and the manuscript were improved through the comments and suggestions of the co-authors.

The work in Chapter 4 of the thesis has appeared in publication as follows:
Birnie, C., Chambers, K. and Angus, D., 2017. Seismic arrival enhancement through the use of noise whitening. *Physics of the Earth and Planetary Interiors*, 262, pp.80-89. doi:10.1016/j.pepi.2016.11.006

Kit Chambers initially suggested to investigate inverting our noise modelling operator for noise suppression. I investigated the idea, developed an algorithm and applied it to a range of semi-synthetic datasets prior to documenting the findings in the manuscript. Both the investigative research and the manuscript were improved through the comments and suggestions of the co-authors.

that no quotation from the thesis may be published without proper acknowledgement

Acknowledgements

"Teamwork is the secret that makes common people achieve uncommon results."
- Ifeanyi Onuoha

And what a team we made! Firstly, I could not have asked for a better supervisory team who have been beside me every step while still ensuring I 'roamed free' both literally and metaphorically. Dr Doug Angus, your continual support and encouragement whilst allowing me to direct the project as I wished gave me the confidence to grow into the researcher I have become - for that I will always be grateful. Dr Kit Chambers, for the innumerable hours you spent understanding the methodologies, developing codes and critiquing manuscripts, thank you! It has been a pleasure working alongside you and you taught me to keep asking questions (and the importance of version control).

A special thanks goes to my examiners, Roger Clark and Mike Kendall, whose great feedback served to further polish this manuscript. In particular, the vast number of papers Roger sourced really helped to enrich the literature review and hopefully make it an interesting read. Tom Lynch and Lisa Roach, thank you for the great times we had whilst organising the UKCCSRC specialist meeting and for always finding time for a coffee and chat, it made the world of a difference. Anna Stork, thank you for all your comments and support, and for taking aspects of my research into your other studies. Richard Rigby, thank you for always being on hand to help with all my software needs, for answering my many questions, and for all you have taught me. While I probably won't miss the emails asking me to kill my jobs, I will miss your enthusiasm and willingness to help. To my UWA hosts, Ben Witten and Jeff Shragge, thank you for the wonderful Ozzy memories.

Finally, to my family - Mum and Dad, from proof-reading papers, to explaining mathematical formulas, to ensuring I had food on the table. My university degrees are a testament of your love, support and encouragement. Thank you! And, to my wonderful husband, who puts up with an endless stream of noise, and the occasional discussion of noise in seismic data. Thank you for refusing to let me believe that I couldn't do this; for the evenings spent scouring books, editing papers, and debugging codes; and for always putting a smile on my face.

Abstract

An ever-present feature in seismic data, noise affects outcomes of processing and imaging algorithms, causing uncertainty in the interpretation of results. Despite abundant evidence that noise is not white, stationary or Gaussian, these assumptions are commonly made when generating noise models and processing data. While synthetic seismic datasets have evolved to include geological complexities, a standardised approach to incorporating realistic noise does not yet exist. The aim of this work is to introduce a noise modelling methodology that avoids the above assumptions.

A statistical analysis of three months of pre-injection noise from the vertical components of a 50 station, *c.*2.5km-wide, cross-shaped array at the Aquistore CO_2 storage site, characterises noise sources originating from wellsite activity and passing traffic. A covariance modelling approach is then devised to generate realistic noise models that have close similarity to the recorded noise in both the time and frequency domain, with $> 65\%$ noise realisations having $> 50\%$ probability of arising from the same distribution as the recorded noise. The modelling procedure is finally applied to two cases: benchmarking and development of microseismic inversion algorithms on synthetic datasets; and noise suppression.

In the former, the source location is correctly estimated at a signal-to-noise ratio of 0.1 with white, Gaussian noise (WGN) but 0.5 was required for realistic noise. Then, applying a microseismic source inversion algorithm, datasets with realistic noise identify pitfalls unobserved under WGN conditions. Thus, in both cases, a WGN assumption gives a misleadingly favourable assessment of efficacy. In the latter, a noise whitening technique that utilises the inverse of the covariance matrix reduces the total noise energy by a factor of 3.5, allowing both imaging of additional microseismic events and greater confidence in identified events.

The proposed techniques are illustrated on passive surface data, but offer future applications in both active and passive seismic monitoring.

Contents

List of Figures

List of Tables

Nomenclature

List of acronyms

CO_2 Carbon dioxide

CONV CONVolution-based modelling method

COVA COVAriance modelling method

DSI Diffraction Stack Imaging

E-W East-West

EDW Event Detection Window

HOSA Higher Order Spectral Analysis

ICOVA Isolated COVAriance modelling method

ILMA Iterative Location and Mechanism Analysis

IPW Independent Patch Whitening procedure

LPF Linear Prediction Filter

LTA Long-Time-Average

MWW Mann-Whitney-White

N-S North-South

PSD Power Spectral Density

RCW Rolling Covariance Whitening procedure

RMS Root-Mean-Square

RNW Rolling Noise Whitening procedure

RTI Reverse Time Imaging

SNR Signal-to-Noise Ratio

SS Semi-Synthetics

STA Short-Time-Average

STA/LTA Short-Time-Average to Long-Time-Average

STFT Short Time Fourier Transform

WGN White, Gausian Noise

List of symbols

$<>$ Expectation estimator

α Whitening scaling factor

$\bar{N}$ Scaled noise data

$\bar{S}$ Scaled waveform data

$\hat{\boldsymbol{d}}$ Data patches with mean subtracted

$\tilde{\boldsymbol{D}}$ Modelled noise patch

$\tilde{\boldsymbol{d}}$ Modelled patch vector

$\tilde{\boldsymbol{x}}$ Whitened realisation of recorded data

$\boldsymbol{b}$ A random vector of Gaussian white noise with unit variance and zero mean

$\boldsymbol{C}$ Covariance matrix

$\boldsymbol{C}^{1/2}$ Lower triangular of Covariance matrix

$\boldsymbol{D}$ Data matrix of patch vectors

$\boldsymbol{d}$ Noise patch vector for COVA modelling

$\boldsymbol{g}$ Random Gaussian trace

$\boldsymbol{n}$ Modelled trace

$\boldsymbol{t}$	Period of recorded noise
$\boldsymbol{x}$	A realisation of recorded data
μ	Mean
μ_i	ith mathematical moment
$A_{i,j}$	Amplitude of a trace j at time point i
D	Combined noise and waveform data
$E[\cdot]$	Expectation operator
K	Number of realisations for COVA modelling
N	Noise data
$n(t)$	Noise
N_t	Number of time samples in window for COVA modelling
n_t	Number of time points
N_x	Number of traces for COVA modelling
n_x	Number of stations
$RMS_{Array}(A)$	RMS of amplitudes computed from all receivers
$RMS_{Station}(A_j)$	RMS of amplitudes for a single station
S	Waveform data
$s(t)$	Desired signal
X	Fourier transform of a time-series x
x	Data point
$x(t)$	Recorded signal
X^*	Complex conjugate of X
$\gamma_{2_{ex}}$	Excess kurtosis
$\hat{b}^2$	Bicoherence

$\hat{t}^2$ Tricoherence

σ Standard deviation

$RMS_{Array}(N)$ Array RMS derived from the noise data

$RMS_{Array}(S)$ Array RMS derived from the waveform data

$RMS_{Station}(N_j)$ Station RMS computed from trace j of the noise data

$RMS_{Station}(S_j)$ Station RMS computed from trace j of the waveform data

γ_1 Skewness

γ_2 Kurtosis

Chapter 1

Introduction

1.1 Aim

Synthetic seismic datasets are commonly used to aid interpretation, test hypotheses and as benchmarking tools for evaluating the robustness of active and passive processing and imaging algorithms. Significant effort has been spent on generating challenging synthetics based on realistic geologies and medium properties, for example the Marmousi model (*Lailly and Versteeg*, 1990). However, a similar effort has yet to be made on the incorporation of realistic noise, which provides an ever-present complication in recorded seismic datasets. Excluding the case of semi-synthetics, incorporated noise is often based on a single statistical phenomenon that assumes noise is time and space invariant, despite extensive literature showing that this is not the case (*Ulrych et al.*, 2009).

The separation of signal and noise is a central issue in seismic data processing (*Ulrych et al.*, 1999). The majority of processing, imaging and inversion techniques are formulated on noise-free data and benchmarked under the assumption of data contaminated with additive White, Gaussian Noise (WGN). For example, *Jurkevics and Wiggins* (1984)'s critique of deconvolution methods focus on how the methods handle incoherent WGN without any investigation into the handling of coherent noise. Whilst the study of *Eisner et al.* (2009) on uncertainty in microseismic monitoring specifically states: 'The surface and downhole location techniques...work flawlessly in a homogeneous isotropic medium that is free of noise' and only extends to testing the effect of noise using WGN. Techniques developed and tested in this manner are likely to fail if coherent noise is present in the data. In imaging procedures this can result in the introduction of artifacts, while in inversion procedures this can lead to errors in the estimated velocity model and predicted source parameters (*Forghani-Arani*, 2013).

Noise is a particular problem in microseismic monitoring due to the characteristically

low Signal-to-Noise Ratio (SNR). This often results in events being unidentifiable on individual traces (*Xuan and Sava*, 2010). The masking of events by noise introduces uncertainty into identifying event arrival times (*Bardainne et al.*, 2009, *Maxwell*, 2014) with numerous studies outlining that the presence of noise, alongside errors in the velocity model, are the most significant obstacles in producing interpretable images from microseismic records (*Eisner et al.*, 2008, *Witten and Artman*, 2011, *Woith et al.*, 2014).

Using surface microseismic monitoring as a testbed, this thesis aims to provide a standard procedure for the generation and incorporation of realistic noise into synthetic datasets. The realistic noise is obtained through statistical characterisation of pre-recorded noise. The benefits of adding realistic noise to synthetics are illustrated for both benchmarking and development of various microseismic monitoring algorithms. Furthermore, utilising the knowledge of the noise modelling procedure, a noise suppression technique is developed that can be tailored to the specific noise properties observed in a dataset and adapt as the noise properties evolve throughout the duration of the recording.

1.2 Background

Noise can be defined as "everything other than the desired signal", and when applied to time series $x(t)$, noise is often introduced as an addition to an ideal noise free time series,

$$x(t) = s(t) + n(t), \tag{1.1}$$

where t denotes recording time, $s(t)$ the noise free time series and, $n(t)$ the recorded noise.

While this is valid from a mathematical point of view, the definition of noise changes according to the disciplinary context. For example, in physics noise is a disturbance obscuring or reducing the clarity of the data while in computer science it is irrelevant or meaningless data (*Meunier*, 2011). Even within geophysics, noise can have different connotations: in active seismics, noise is typically any signal recorded other than the primary reflections, while in microseismic monitoring, noise is typically anything other than the direct arrivals from the microseismic events.

Noise is both coherent and random, with the coherent component often masquerading as signal (*Ulrych et al.*, 1999). The separation between signal and noise is one of the dominant issues in microseismic monitoring resulting in errors in velocity models and source parameters (*Forghani-Arani et al.*, 2013). This is in part because inversion algorithms are designed for either noise-free signals or for signals where noise present is

assumed to be additive, white and Gaussian (*Vavryčuk*, 2007). However, *Ulrych et al.* (2009)'s postulates of noise state that:

1. Signal and noise are always correlated to some extent,
2. Noise is never white, and
3. Noise is seldom, if ever, Gaussian.

Therefore, as noise is not white and/or Gaussian, such algorithms can only perform optimally if noise is suppressed or at least whitened before they can be applied. In other words, if complete separation between signal and noise is not achieved prior to applying the algorithm, then it will be difficult to establish the degree of confidence one might have in any of the resulting interpretations.

While generally expressed as a single term, as illustrated in equation 1.1, in reality noise arises from a number of different sources each with their own spatio-temporal properties. For example, a passing car will create an energy burst across receivers with a distinct moveout pattern, however, instrument noise will be spatially independent. The majority of noise suppression techniques work by exploiting the characteristics of a noise signal that differentiate it from the desired signal. In the following I discuss a variety of noise signals, detailing their individual characteristics. I further discuss the current state of the creation of synthetic datasets and different approaches to their incorporation of noise. Finally, I conclude with an overview of noise suppression techniques that have been developed to suppress the vast range of different noise signals present in seismic data.

1.2.1 Noise in surface microseismic datasets

Seismic noise arises from a variety of activities, some dependent on human interactions and others completely independent. For characterisation purposes, noise sources have been separated into five categories:

1. natural background noise,
2. cultural noise,
3. medium-induced noise,
4. instrument noise, and
5. algorithm noise,

excluding any noise arising from acquisition related issues, such as poorly planted and/or clamped geophones or incorrect instrument response corrections. Figure 1.1 provides an illustration of these noise categories and the noise sources in which they contain.

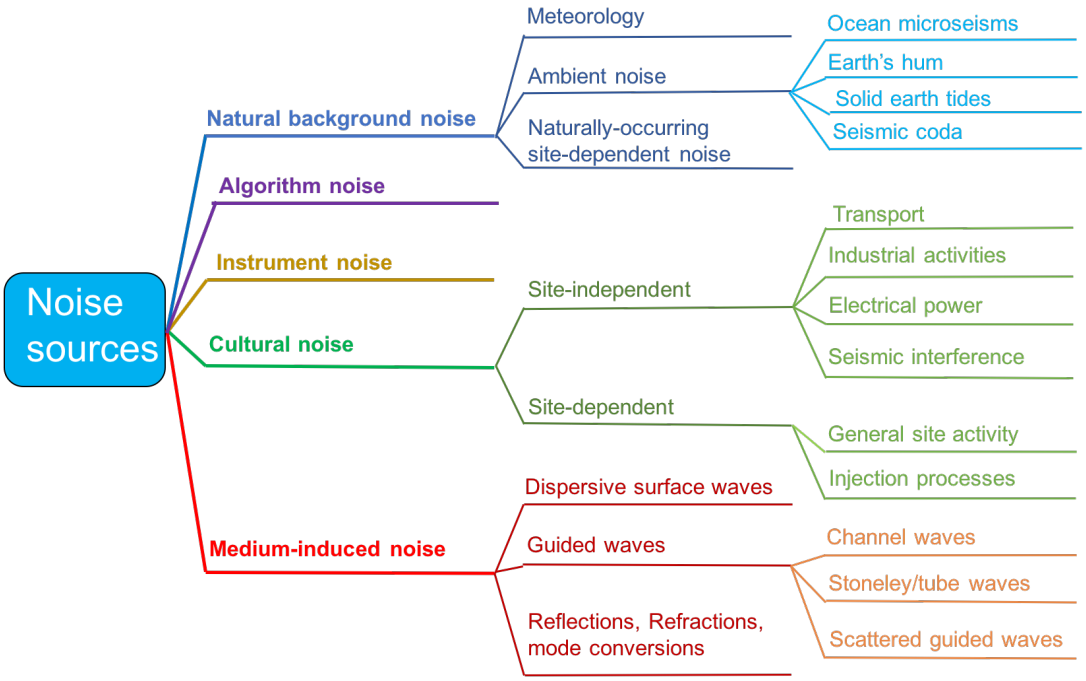

Figure 1.1: *A typology of noise sources.*

Natural background noise

Natural background noise is strongly affected by geographical location of the seismic array and, by definition, is unaffected by the presence of industrial activity (*McNamara et al.*, 2009). As shown in Figure 1.1, background noise can be split into 3 sub-sections: ambient seismic noise, meteorological noise and naturally-occurring, site-dependent noise.

In some studies the term ambient noise is used to describe both cultural and natural background noise, however this is not the view taken here. Ambient noise, as defined here, contains signals from microseisms, the Earth's "hum", solid earth tides and seismic coda, where the first three sources consist mostly of surface waves (*Friedrich et al.*, 1998). *Hasselmann* (1963) considered three possible origins of microseisms: (1) the interaction of the coast and ocean-waves proposed by *Wiechert* (1904); (2) atmospheric pressure fluctuations proposed by *Gherzi* (1924); and (3) nonlinear interactions between ocean waves proposed by *Longuet-Higgins* (1950). Similar to the origin of microseisms, the origin of the Earths "hum" is debated with the majority of studies associating it with atmospheric turbulence (*Kobayashi and Nishida*, 1998, *Nishida et al.*, 2000, *Ekström*, 2001, *Nishida et al.*, 2002) while others believe the excitation source lies under the oceans (*Ekstrom and Ekstrom*, 2005, *Romanowicz et al.*, 2005, *Webb*, 2007). Solid earth tides are excited by the interactions of the Earth with the sun and the moon, and fluctuate on a daily timescale. Finally, seismic coda consists of waves created from a seismic source, typically with a magnitude greater than M4, that have been scattered

or reflected at least once due to small-scale inhomogeneities (*Weaver*, 2005, *Aki and Chouet*, 1975). Due to anelastic absorption along their travel path there is an absence of high frequency waves in the late coda limiting the frequency band to 1-10Hz (*Aki*, 1969). As noted in Table 1.1, the frequency bandwidths of these noise signals are lower than would be considered in the typical surface microseismic monitoring scenario (approximately 10-60Hz).

Table 1.1: *Ambient noise properties*

Ambient noise source	Period (s)	Frequency (Hz)
Primary band microseisms	10-20	0.05-0.1
Secondary band microseisms	5-10	0.1-0.2
Earth's hum	20-40	0.025-0.05
Solid Earth tides	12-24 hours	12-23 µHz
Seismic coda	0.1-1	1-10

Meteorological noise results both from wind and precipitation. Seismic wind noise is one of the least understood phenomena in land seismic acquisition and, in extreme cases, severe degradation of the SNR has resulted in the suspension of seismic recording (*Bland and Gallant*, 2001). *Nørmark* (2011) observed that due to surface roughness and the logarithmic wind profile, surface wind speed is significantly lower than the standard wind speed measured at 10 meters above the surface, as such the resulting noise is characterized by a steady noise level dependent on the wind speed. *Barajas-Olalde and Jeffreys* (2014) confirmed the sensitivity of 3-component geophones to wind noise and the spatial correlation of wind between sensors by measuring the spectral characteristics of wind. They concluded that the horizontal component is more sensitive to wind noise than the vertical component and that for every 10cm the geophone is buried there is a 10dB reduction in wind noise. They also observed a correlation of higher noise amplitudes with increasing wind speeds supporting *Nørmark* (2011)'s claim that noise level is dependent on wind speed.

The level of wind noise is highly related to the area in which the instrument is placed. At around 1Hz, seismic noise in the oceans is produced locally by wind-generated waves (*Wilcock et al.*, 1999). Comparing noise data from two experiments, *Wilcock et al.* (1999) observed that 1Hz noise levels are well correlated with local sea-surface-wind speeds derived from satellite observations. Figure 1.2(a) illustrates that the power of the P-wave noise is highly correlated with offshore wind speed inferring that the P-waves are excited by distant ocean winds. *Zhang et al.* (2009) studied two remote land seismic stations and after applying beamforming techniques they also determined that in the bandwidth of 0.6-2Hz a significant amount of the noise consists of continuous P-waves originating offshore. Considering distance away from the coast, *Wilcock et al.* (1999) observed that there is a 10dB drop in the 1Hz noise level 100km inland.

Another significant influence of the site location on the level of wind noise is the amount and type of vegetation present. This can influence the overall noise level or introduce fluctuations in the noise. *Schilke et al.* (2014) considered stations extending across a wooded area and a field; they observed no significant changes in the overall noise level but fewer fluctuations in the noise were observed at the stations located in the field. They thus proposed that this is due to the absence of tree roots transmitting wind energy into the ground. *El-Kaseeh et al.* (2010) acquired a 2D line during a period of strong winds where the line transversed fields full of tall crops (Figure 1.2(b)). The resulting high frequency noise in the data has been attributed to the strong winds blowing through the crops. To conclude the discussion on the effect of vegetation on wind noise, it is important to acknowledge that while tree roots can cause a secondary noise source excited by wind, the presence of trees can also act as a windbreak lowering the overall wind speed in an area (*Kainkwa and Stigter*, 1994). *Heisler and Dewalle* (1988) proposed the wind reduction ratio to investigate wind speed reduction within a sparse tree canopy relative to that in the open. They observed that windspeed reductions of 20% and above may extend to a horizontal distances of 25 times the height of the windbreak, while reductions are observable at horizontal distances of up to 50 times the windbreaks height.

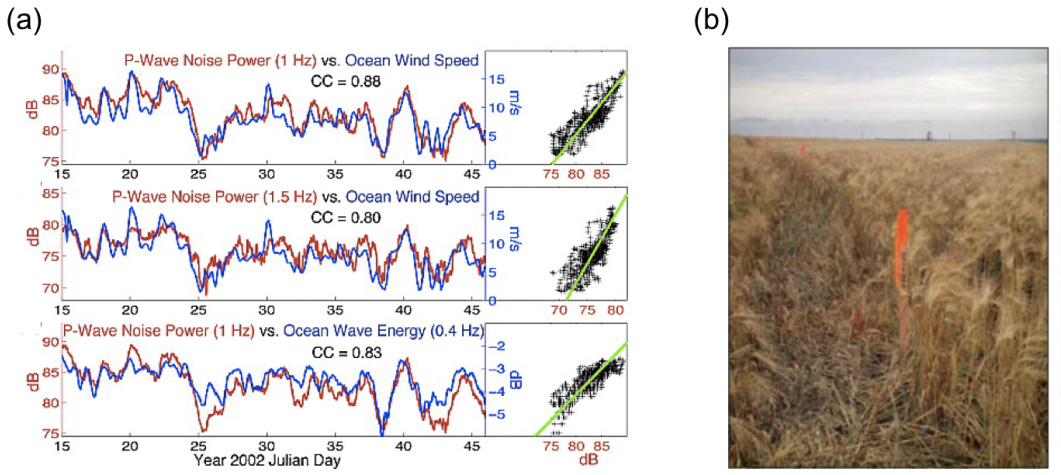

Figure 1.2: *Effect of site location on wind noise levels. (a) Correlation between ocean wind speed and on-shore seismic p-wave noise power (figure 4(c-e) from Zhang et al. (2009)), and (b) photograph of seismic survey though field of high vegetation that experienced significant levels of high frequency noise attributed to wind blowing through the crops (Figure 2 from El-Kaseeh et al. (2010))*

In contrast to wind, the characteristics of noise due to precipitation has been not considered to the same extent. However, *Nørmark* (2011)'s study used sledge-mounted geophones to determine the characteristics of rain-generated noise. As the geophones recorded a distinct signal per raindrop, rain-generated noise is localised and non-

repeating. Similar to the benefits it brought for wind noise levels, field experiments concluded that by burying the geophones noise levels due to rain can be reduced by between 7.7 and 8.6 dB/0.1 m (*Dean*, 2017).

Heavy precipitation is a common trigger for mass flows in steep mountainous regions, generating a secondary noise source. A significant effort has been focussed on characterising seismic signals related to the various types of mass flows such as debris flows (*Huang et al.*, 2007), landslides (*Yamada et al.*, 2013), avalanches (*Bessason et al.*, 2007) and lahars (*Tuñgol and Regalado*, 1996, *Walsh et al.*, 2016). *Tuñgol and Regalado* (1996) computed the threshold of rainfall over which lahars along the Sacabio River are generated to be 0.3 mm/minute for 30 minutes while *Walsh et al.* (2016) noted the Te Maari lake breakout lahar was preceded by several weeks of rainfall. The seismic signals of debris flows were characterised by *Huang et al.* (2007) who highlighted the different properties between the surge front and the flow tail. The overall seismic frequency of flows typically ranges from 10 to 100 Hz with dominant frequencies of 10 to 30 Hz for the surge front and 60 to 80 Hz for the flow tail. This difference in dominant frequencies has been attributed to larger stones being accumulated at the front of the flow.

The final sub-category of natural background noise encompasses all remaining noise sources naturally arising from the environment in which the sensors are placed. These include but are not limited to wildlife, landforms and naturally occurring phenomena. The Australian National Seismograph Network has frequent observations of kangaroos bounding by, so much so they have concluded that kangaroos hop at one hop per second (*Owen*, 2003). *Burtin et al.* (2008) analysed one-year of data collected on an array that follows the trans-Himalayan Trisuli River. Comparing the seismic noise with meteorological and hydrological data, they concluded that while river-induced seismic noise is partly generated by stream turbulence, this did not fully explain the observed lag between the seismic noise amplitude and the water level. This lag was better explained if a significant portion of the noise was caused by ground vibrations generated by bed load transport. As well as wildlife and landforms, other natural phenomena can introduce noise into a seismic recording. During the Taurid meteor shower in 2003, 22 stations from the Center for Earthquake Research and Information Cooperative Seismic Network observed the sonic boom associated with a bolide (i.e., an extremely bright meteor) (*Langston*, 2004). Other examples of natural phenomena observed on seismic records include *Pino et al.* (2004)'s study on the high frequency seismic observations of a tsunami induced by a submarine slump at the Stromboli volcano in Sicily and *Yuan et al.* (2005)'s long period seismic observations of the Indian Ocean tsunami triggered by the 26 December 2004 Sumatra-Andaman earthquake. *Yuan et al.* (2005) focussed on long-period (>1000 s) signals on the horizontal components of the sensor which arrived at the same time as the tsunami and could not be attributed to seismic surface

waves, whereas *Pino et al.* (2004) focussed on the bandwidth of 0.5 - 3 Hz.

Cultural noise

There are two main categories of cultural noise. The first arises from the daily activities of people, for example cars travelling along a road, and is sometimes referred to as microtremors. The second is instead generated by on-site activity, for example a diesel generator providing an on-site power source. The first category contains sources independent of site activity and therefore outwith the control of the surveying company. Noise in this category is highly dependent on site location and it is the result of sources arising from people's daily lives and local industrial activities.

Noise sources from daily activities typically fall into the categories of transportation, electrical power transportation/consumption and recreational activities. Each mode of transport creates a different noise signal. A number of studies have focussed on the seismic signature of traffic noise. Table 1.2 (adapted from *Peck* (2008)) displays the frequency ranges within which road traffic signals are dominant and, as shown in Chapter 2, the signal from a passing vehicle exhibits a Doppler shift. *Butler* (1975) identified that each pass of a car produces a different ground motion spectra, which he contributed to the inconsistencies in the road surface, i.e., the car passing over different bumps in the road on each pass. *Coward et al.* (2003) also attributed rapid fluctuations in road noise to varying axle loads caused by an uneven road surface.

Table 1.2: *Frequency content of road noise, adapted from Peck (2008)*

Study	Location	Frequency range (Hz)
Butler (1975)	Alabama	2 - 50
Long (1993)	Georgia	1 - 50
Holub (1997)	Czech Republic	3 - 25
Schofield et al. (2000)	Washington	1 - 50
Lombaert and Degrande (2001)	The Netherlands	5 - 40
Coward et al. (2003)	Australia	5 - 30

The propagation of ground vibrations from rail transportation has also been well studied due to concerns of potential damage of passing trains on the surrounding areas. Figure 1.3 (adapted from *Kouroussis et al.* (2014)) illustrates the ground vibrations of the tram system in Brussels while *Lombaert et al.* (2015) provides a comprehensive overview on railway-induced ground vibration covering rail transport from underground railway lines, to light rail systems, to high speed train networks, with a particular focus on the effect of the ground vibrations on the surrounding area. Trains create vibrations which are transmitted through the soil and interact with the foundations of adjacent buildings, resulting in disturbance from vibrations (180 Hz) and re-radiated noise (1200 Hz) (*Degrande et al.*, 2006). As shown by *Green et al.* (2017), noise associated with

public transport has a strong diurnal variation. Considering a receiver placed above a London Underground station, noise levels were seen to drop by 20 dB during the short night time period in which the underground was not operating. Interestingly, ground-bourne vibrations are not the only noise source generated by passing rail traffic. The arrival of electric trains is often observed by the electrical interference noise generated by their power supply prior to the detection of ground motion (*Clark*, 2018).

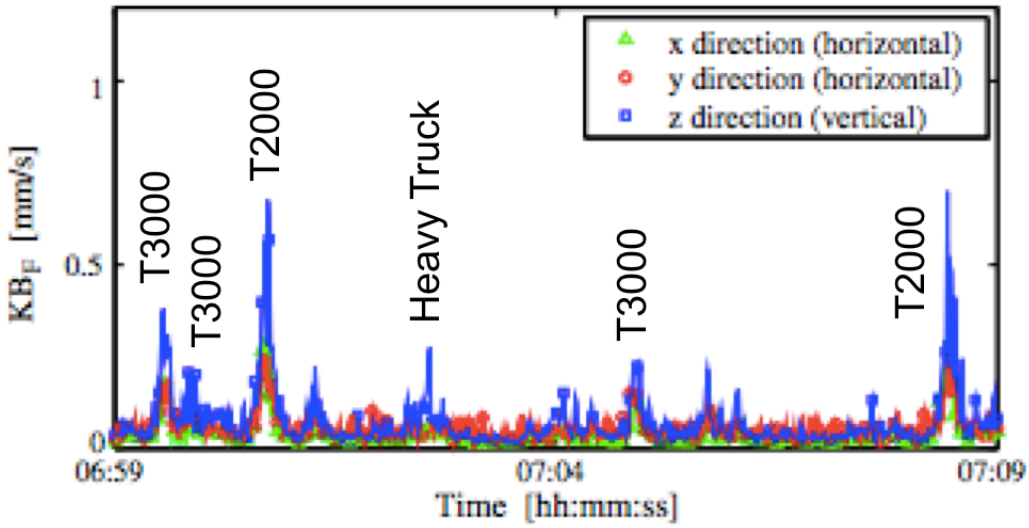

Figure 1.3: *Recorded ground vibrations from a time period in which the passing of two types of trams, T3000 and T2000, and a heavy truck were observed (adapted from Figure 5 of Kouroussis et al. (2014)).*

Finally, *Riahi et al.* (2013) studied noise from the airport at Long Beach, California. By considering the seismic power, takeoffs and landings were identified as well as computing acceleration and takeoff/landing velocity for two aircraft, $1m/s^2$ acceleration with a takeoff velocity of $80m/s$ and a touchdown velocity of $69m/s$ with a deceleration of $1.8m/s^2$. On a more sombre note, a number of studies have detected and located plane crashes based on the seismic signals of their impact being recorded on nearby seismic stations (*Aspinall and Morgan*, 1983, *Johnston*, 1987, *Alavès*, 2012). In the tragic events that occurred on September 11 2001, seismologists identified both crashes and the subsequent collapses of the Twin Towers (*Kim et al.*, 2001). Recorded on stations with distances from the towers ranging from 34 km to 428 km, the computed local magnitudes of the collapses was 2.1 and 2.3 for the first and second collapse respectively, with the surface waves being the largest seismic wave observed at the stations.

Transportation of power is also a source of seismic noise - power line noise originates from electromagnetic interference between the power lines and the surveying sensors, signal lines or digitizer and is observed at a single frequency (50Hz or 60Hz) depending

on country of the site (*Bland*, 2006). Power line noise and its harmonics lie directly within the optimum frequency range of seismic surveys making their suppression necessary (*Xia and Miller*, 2000). It is worth noting that alongside electrical noise, high voltage power lines can also emit audible noise caused by a discharge of energy that occurs when the electrical field strength on the conductor surface is greater than the breakdown strength of the air surrounding the conductor (*Dent*, 2013).

The final sources of noise arising from the daily activities of people are those arising from recreational activities. A handful of studies have considered vibrations induced by rock concerts and music festivals (*Erlingsson and Bodare*, 1996, *Green and Bowers*, 2008, *Bertero et al.*, 2012, *Díaz et al.*, 2017). *Bertero et al.* (2012) observed Rayleigh waves resulting from the coordinated jumping of spectators while *Díaz et al.* (2017) observed that during the "Encores" part of the Bruce Springsteen concert each song had a specific frequency content, as shown in Figure 1.4. Sporting events have also been associated with large amounts of seismic noise. The most famous of these must be the 'Beast Quake' where the local Seahawk team obtained an unlikely win on 8 January 2011. The roar and stomping of the "tens of thousands" of feet generated vibrations heard at a strong motion station a block away (*Vidale*, 2011). Figure 1.5 adapted from *Malone et al.* (2015) highlights the difference in the 'Beast Quake' with a more recent 'Dance Quake' where the crowd were recorded dancing and jumping in time to their chant 'Dee-Fence-Now'. A similar experience was observed in Barcelona at the 2015 Champions League final, with all 3 FC Barcelona goals producing distinct bursts in the seismic signal recorded by a nearby sensor (*Díaz et al.*, 2017).

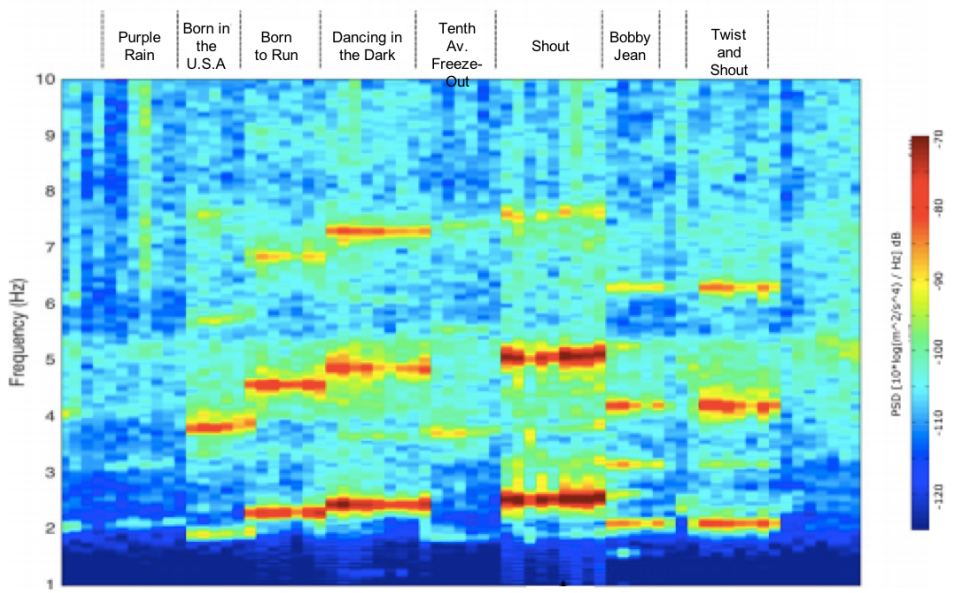

Figure 1.4: *Amplitude spectra for Encore of a Bruce Springsteen concert with songs displayed along the top x-axis (adapted from Figure 5 of Díaz et al. (2017))*

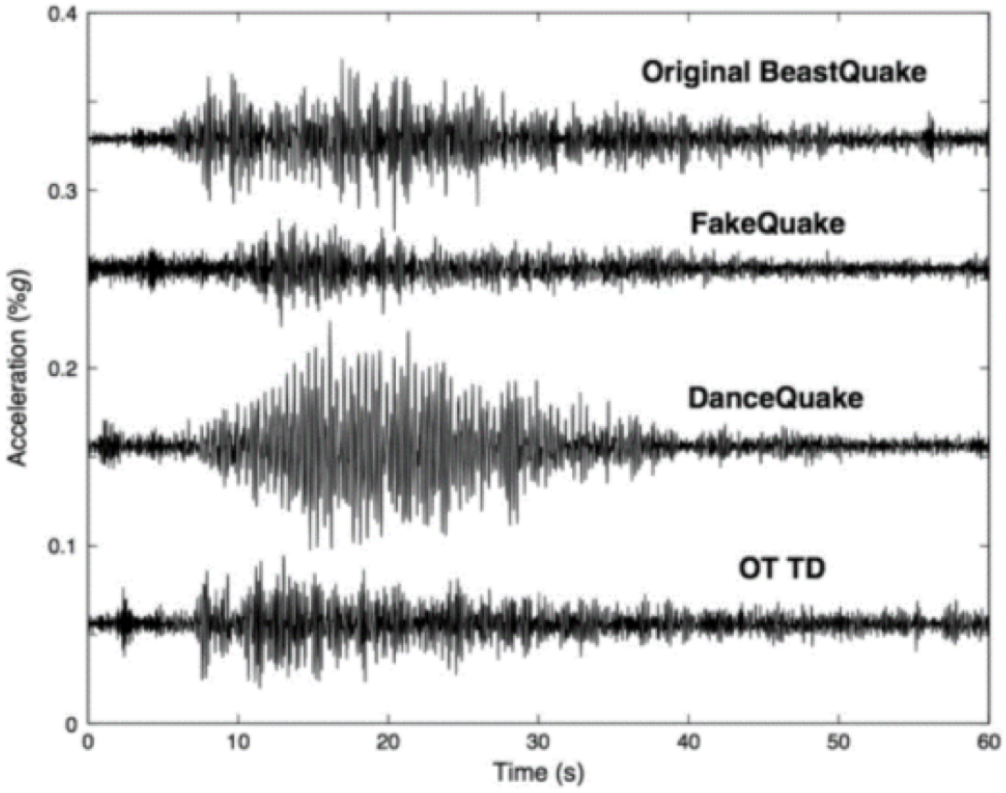

Figure 1.5: *Comparison of quakes observed at the Seahawk's stadium, including the original Beast Quake of 2011 and a Dance Quake from fans jumping and chanting in rhythm. (Figure 1 from Malone et al. (2015))*

Local industrial processes include activities and machinery, which can range from small-scale, independent farmers to large-scale, mining activities. Starting at the small-scale, *Shalev et al.* (2002) observed the movements of Maasai and their herds on their array. Large machinery, such as wind turbines, transfer energy into the ground generating ground-borne vibrations, both during operation and when parked (*Butt and Ishihara*, 2012). For wind turbines, induced ground vibrations are observed to differ with wind speed, both in terms of amplitude and frequency content (*Legerton et al.*, 1996, *Schofield*, 2001) and can propagate up to 10 km or more (*Styles et al.*, 2005). Despite the potential to propagate a significant distance, vibrations decay rapidly away from the turbine dropping by a factor of 100 over 200 metres for a small (50 kW) turbine (*Westwood et al.*, 2015). As well as direct coupling with the ground, other large machinery, such as military jets and spaceships, are air-borne noise sources. In particular, the sonic boom of aircraft produces a small but detectable ground motion (*Cates and Sturtevant*, 2002, *Wurman et al.*, 2011). *Grover* (1973) concluded that infrasonic waves from Concorde flights propagated to at least 300 km. Another example of a sonic boom being heard was on the re-entry of the space shuttle "Atlantis" which was observed on a number of receivers in the Western United States as well as by mil-

lions of people(*de Groot-Hedlin et al.*, 2008). The resulting double sonic boom from the re-entry was detected on stations hundreds of kilometers away from the shuttle trajectory.

Other noise sources from outwith the site's control include noise created from seismic interference of other man-made seismic events occurring during recording For example, *Verdon et al.* (2016) observe seismicity related to nearby potash mining activity. If this event arrives at the same time as the desired signal it may mask it and cause extreme difficulty in extraction of the desired signal from the other seismic event. This is a prominant issue in marine acquisition where multiple surveys are being acquired simultaneously resulting in 'cross-talk' (*Akbulut et al.*, 1984, *Gulunay et al.*, 2004), however in active land seismic surveys simultaneous sources are utilised to cover more ground than traditionally possible (*Stone and Bouska*, 2013). For land microseismic monitoring, these sources should be suppressed as much as possible prior to imaging.

The second category of cultural noise originates from noise created from on-site processes. This is considered to be the main noise source from surface microseismic monitoring due to the presence of active hydraulic pumps. To some extent this can be controlled. However, it is not always possible to reduce all on-site noise. *Hardage* (2000) states that the only way to avoid severe cultural noise is to create as quiet an environment as possible. His suggestions are to remove all non-vital equipment and processes whilst recording, for example removing the drill rig prior to a borehole survey. Noise can arise from almost all on-site activities, from driving along the array line to running a generator, an example of some on-site noise source signals is given in Figure 1.6. In the hydraulic fracturing case, an obvious source of significant noise arises from the fracture treatment itself, for this reason surface sensors are rarely placed in the immediate vicinity of the wellhead. *Drew et al.* (2012) and *Schilke et al.* (2014) both investigated the effect of pumping on the level of noise recorded on both surface and borehole arrays. Considering a single surface receiver line of approximately 1095 m projected away from the treatment wellhead *Schilke et al.* (2014) observed that there was a increase in the root-mean-square (RMS) noise level of an order of magnitude at the stations closest to the treatment wellhead in comparison to the stations furthest away, where the closest station is approx. 60 m from the wellhead. *Drew et al.* (2012) also observed a correlation between noise level and distance from the wellhead particularly in the shallow borehole arrays. However, they went one step further and considered the effect of the different stages of treatment to which he concluded that there was no significant change in noise level between treatment stages.

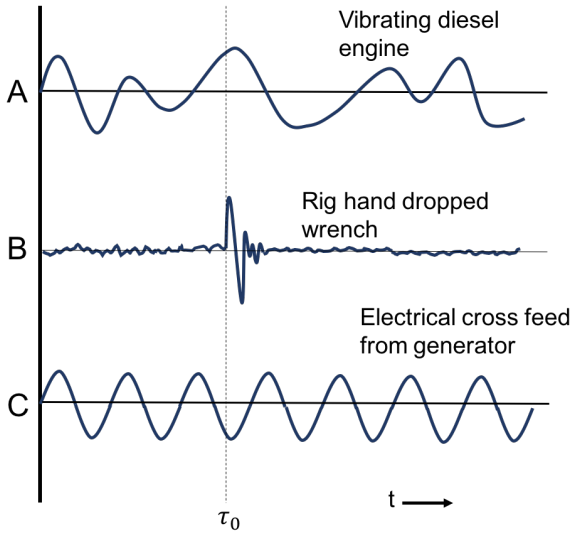

Figure 1.6: *Schematic of on-site cultural noise source signatures (Adapted from Hardage (2000))*

Medium-induced noise

A large proportion of seismic noise originates from previously created seismic energy being altered as it passes through the subsurface. This noise comes in the form of mode conversions, reflections, refractions, guided waves and dispersive surface waves. *Lamb* (1904) highlights the problem of mode conversion and reflection that occurs when a wave arrives at an interface. For example, when a P-wave encounters an interface both a P- and a S-waves are reflected and transmitted in accordance with Snell's law for the kinematic part of the wavefield (*Budden*, 1961), as illlustrated in Figure 1.7(a), and Knot-Zoeppritz equation for its dynamic part (i.e., amplitude variation with offset) (*Knot*, 1899, *Zoeppritz*, 1919).

An exception occurs when a wave arrives at normal incidence to the interface in which case no mode conversion occurs however the same mode energy is still both transmitted and reflected. Figure 1.7(b) illustrates a critically refracted wave, also known as an interface or head wave, whose energy travels along the interface between a low velocity layer above a higher velocity layer. According to Huygens Theory of Wavelets (*Gabrielov and Palamodov*, 1968), the critically refracted wave acts as a source for new secondary wave fronts and ray paths exiting at angles equal to the critical angle.

Another example of seismically-generated noise is that of guided waves, where waves are 'guided' along an interface. These waves can be split into three categories:

1. channel waves,
2. Stoneley or tube waves, and
3. scattered guided waves.

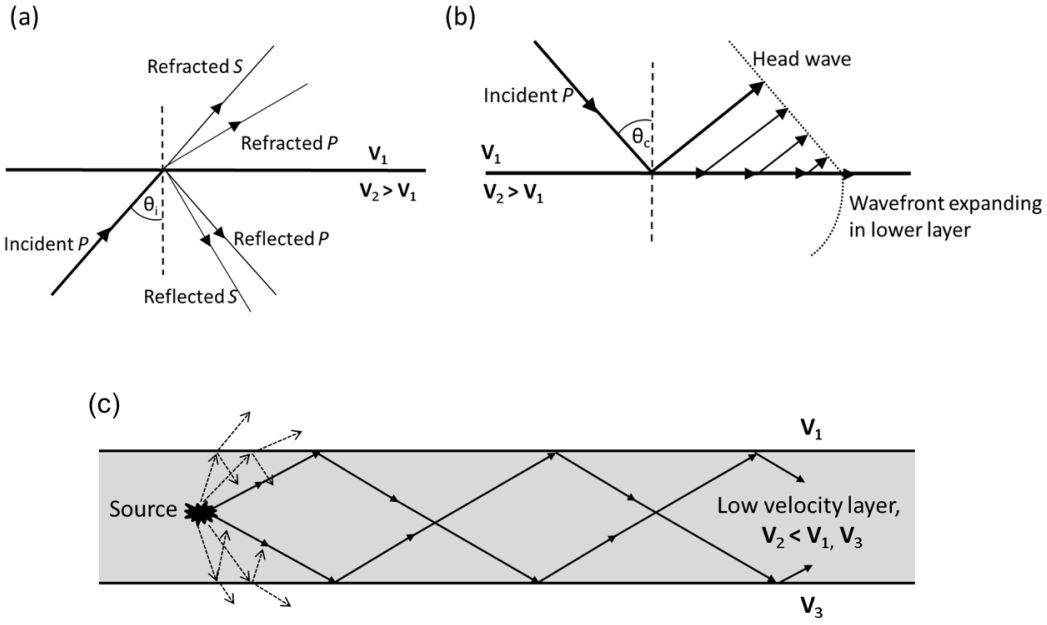

Figure 1.7: *Schematic illustration of (a) wave mode conversion and reflection at an interface,(b) production of head waves from an incident ray at the critical angle, and (c) entrapment of channel waves in a low velocity layer. Rays are annotated as lines with arrows describing their direction of travel while wave fronts are illustrated as dotted lines without arrows.*

Channel waves are formed by waves being trapped in a low velocity, low Q zone, such as a fault zone (*Li et al.*, 1994). This zone acts in a similar manner to an optical fibre with low angle rays being trapped within the layer as illustrated in Figure 1.7(c). Tube waves carry energy along the axis of the fluid-filled borehole and allow very little energy to be transmitted into the formation resulting in amplitudes degrading a lot slower than is typical for body waves as they cannot expand spherically (*Hardage*, 2000). Tube waves are especially difficult to suppress by digital filtering as they span the same frequency content as their original seismic source. The last type of such waves is scattered guided waves that are trapped in low velocity, near-surface layers and are scattered by local heterogeneities, for example large boulders or karsts (*Ernst et al.*, 2002).

Another form of medium-induced noise that propagates along the near-surface is ground roll. Ground roll is a surface wave whose vertical component is composed of dispersive Rayleigh waves with different frequency components travelling at different speeds (*Kahrizi et al.*, 2014). It is a form of coherent noise with a characteristically low frequency and high amplitude. Suppression of ground roll can be achieved reasonably well either during acquisition or pre-processing for instance, using specific array patterns (*Morse and Hildebrandt*, 1989), polarization methods (*Perelberg and Hornbostel*, 1994) or linear filters (*Herrmann and Russell*, 1990). Whilst ground roll consists of Rayleigh waves, another form of waves that propagate along the subsurface are Love waves.

Observed on the horizontal components of a geophone, these can arise from coupling between a source of energy and the ground, for example due to traffic (*Nakata et al.*, 2011) or from an explosion (*Aki and Tsai*, 1972).

The final form of medium-induced noise that will be discussed here is that related to the influence of the geological setting in which the geophone is planted, commonly referred to as site-effects. This includes the distortion of seismic waves, including attenuation, amplification and scattering, in the near-surface rocks (*Abercrombie*, 1997). Sediments caused the amplification of The Michoacan, Mexico earthquake by a factor of 10 whilst also significantly prolonging the duration of the observed effects of the earthquake (*Celebi et al.*, 1987). Near-surface attenuation is also a known problem with *Abercrombie* (1995) computing that 90% of attenuation of an earthquake 15km from the site occurred in the upper 3km of the subsurface.

Instrument noise

Self-noise of an instrument limits the smallest signals which can be detected (*Evans et al.*, 2010), while weak seismic signals may be masked or distorted by the self-noise of an instrument (*Tasič and Runovc*, 2012). This is a particular issue for recording in areas with very low seismic noise such as Deep Springs, California (*Gurrola et al.*, 1990). Ground motions at such sites are of the order of tenths of nanometers of displacement and nano-gs of acceleration therefore significant consideration must be given to the recording instrument to minimise the possibility of self-noise masking the seismic signals (*Rodgers*, 1992). Self-noise is the sum of noises arising from the following 6 sources:

1. Suspension (Brownian) noise,
2. Johnson (thermal) noise from the coil and damping,
3. Electronic (voltage and current) noise from the preamplifier,
4. Cross-axis sensitivity,
5. Parametric effects, and
6. Suspension resonances,

where the first three are well characterised and the final three less so.

Suspension noise arises from the Brownian motion of a mass in a spring-mass system. The Power Spectral Density (PSD) of suspension noise can be derived from the expression for suspension noise given by *Aki and Richards* (1980),

$$S_{nn} = 16\frac{\pi kT\zeta f_o}{M}, \tag{1.2}$$

Where S_{nn} is the PSD of suspension noise and a constant, k is Boltzmanns constant, T is room temperature, ζ is the damping ratio of the spring/mass system, M is the

mass, and f_o is the systems resonant frequency. In a comparison of three seismometers, *Rodgers* (1992) concluded that only for one instrument did the suspension noise become a significant fraction of the total noise. This was attributed to the instruments small mass (0.0728 kg) and high damping ratio (0.8)

Johnson noise is the electronic noise (random voltage) generated by the thermal agitation of electrons. The PSD of Johnson noise can be described as,

$$J_{nn} = 4kTR \tag{1.3}$$

where J_{nn} is the PSD of Johnson noise and R is the resistance of the system. *Rodgers* (1992) argues that one of the reasons for keeping circuit resistances as low as possible is that even at 'small' resistances, such as 0.5 k-ohm, Johnson noise nearly equals the voltage noise at the input of a low noise operational amplifier. As Johnson noise is only present in dissipative elements of a circuit, ideal capacitors and inductors generate no Johnson noise (*Riedesel et al.*, 1990).

Voltage and current noise are both identified at the input of the preamplifier. While voltage noise represents the variation in voltage between the positive and negative inputs with respect to the nominal value, the current noise describes the fluctuations of the current at each input with respect to the nominal current value of the circuit. These two noises are connected via the impedance of the resistor (i.e., Ohms Law) and, depending on the magnitude of the impedance, one of the two dominates the other.

The remaining three sources of self-noise include: cross axis sensitivity, parametric effects, and suspension resonances. Cross-axis sensitivity is when a pendulum is out of equilibrium, it also becomes sensitive to the acceleration along the direction perpendicular to the axis of sensitivity (*Graizer and Kalkan*, 2008). Parametric effects arise from accelerations at right angles to the direction of pendulum motion (*Rodgers*, 1966). Finally, suspension resonances limit the upper frequency range of seismometers however these should typically occur at higher frequencies than those of interest. *Rodgers* (1992) measured and numerically modelled self-noise of 3 different instruments, excluding the less well characterised noise sources. As there was a high similarity between the measured and numerically modelled results, he concluded that it is possible to get accurate self-noise levels without including the final 3 sources.

Algorithm noise

The analysis so far has focused on physical noise sources that affect seismic data since the very beginning when the data is acquired. However, the output that we can generally interpret and use to make decisions is the product of many processing steps where

each of them is carried out by a computer, often in the form of an algorithm. These have the opportunity to introduce a number of different noise sources, the main one being: round-off error, the number generated by the machine versus the exact mathematical value. Depending on the magnitude of the input signal and the instruments precision consideration should be made on the precision (i.e., single versus double) of floating-point format used for the input, output and local variables of an algorithm.

With modern computers round-off noise is becoming more irrelevant and is generally much smaller than other sources of noise. However, in some algorithms this may not be so irrelevant, especially if multiple small rounding errors have the opportunity to accumulate. An example of this phenomenon is well-known to happen in finite-difference modelling of partial differential equations (*Courant et al.*, 1967, *Lilla*, 1997, *Hayashi et al.*, 2001, *Kristek et al.*, 2010). More precisely, a finite-difference scheme is stable if the errors made at one time step of the calculation are not magnified as the computations progress through time; if the error decays and eventually damps out, the scheme is said to be stable. This has led to the well-known Courant Friedrichs-Lewy (CFL) condition (as shown in equation 1.4) that defines the maximum allowed time step (d_t) based on the maximum velocity (v_{max}) and spatial sampling (d_x) for the wave equation and should always be checked prior to modelling seismic data, as was done for the modelling in Chapters 3 and 4.

$$d_t <= \frac{0.606 * d_x}{v_{max}} \tag{1.4}$$

Another field in which numerical precision should be taken into account is the solution of linear systems, or equivalently the inversion of matrices. In fact, the inversion of matrices that present very small eigenvalues, although still possible in theory, will generally lead to unstable numerical solutions. More specifically, the condition number (i.e., ratio between highest and smallest eigenvalue) is a diagnostic measure of the ill-posedness of the numerical inverse problem (*Cheney and Kincaid*, 2012). A large body of literature describes this phenomenon and possible ways to prevent numerical instabilities, for example Tikhonov regularisation (*Tikhonov et al.*, 2013, *Tarantola*, 2005). The addition of a small identity matrix prior to Cholesky decomposition in the noise modelling procedure outlined in Chapter 2 is an example of a case where regularisation is required.

Finally, to treat seismic data by means of a computer the elastic waves that are recorded by geophones will need to undergo an analogue to digital transformation. While an analogue signal is a continuous signal by definition, a digital signal has a finite sampling rate. The choice of such sampling rate defines the maximum (or Nyquist) frequency of the analogue signal that can be perfectly reconstructed from the digital signal: this is the well-known Shannon-Nyquist theorem, $f_{Nyq} = 1/2d_t$. Anti-aliasing filters are

applied to remove frequencies close-to and above the Nyquist frequency, in order to prevent them from overlapping within the desired bandwidth. As a typical sampling rate of seismic data is 4 milliseconds, the maximum frequency is 125 Hz.

1.2.2 Noise in synthetic datasets

Synthetic datasets are commonly used as a benchmarking tool for testing inversion and imaging algorithms as they allow comparison between the estimated solution and a known one. Over the years these datasets have grown more complex in terms of geology and waveform properties, as previous assumptions required to make problems computationally solvable are questioned. A widely-used dataset is the Marmousi synthetic dataset whose criteria were that the synthetic data were so complex that the assumptions on which conventional processing relied should not hold, while the model was still to be geologically plausible (*Bourgeois et al.*, 1991). Table 1.3 details other well-known, open-source synthetic datasets and it highlights the reasons behind their creation. Whilst there have been great advancements in the modelling and waveform section of synthetic datasets, there has yet to be a dataset created to challenge the commonly-used WGN assumption.

There have been advances in the incorporation of realistic noise into synthetic datasets, with techniques ranging from no influence of recorded noise, to some reliance on recorded noise, to direct incorporation of the recorded noise. The modelling method of distributed surface sources (*Sylvette et al.*, 2006) is a theoretical approach, that is independent of recorded noise. The resulting noise models have similar characteristics to field measurements however are unlikely to capture the complexities of noise arising due to geologic, geographic, and meteorological influences (*Dean et al.*, 2015). *Pearce and Barley* (1977) proposed a technique that involves convolving a sample of recorded noise with broad-band white noise creating coloured, Gaussian noise. However the main drawback is that this approach requires noise to be stationary and therefore also fails to capture the full complexity of noise. The modelling technique proposed in Chapter 2 is a statistical modelling method based on properties extracted from segments of recorded noise. The resulting noise models are shown to have a close similarity to recorded noise and allow for 'tailoring' of the noise models and the incorporation of noise signals on the full spectrum of stationarity. However, the technique requires noise statistics obtained from recorded noise prior to modelling and therefore is dependant on the availability of such data.

A non-modelling approach is that of semi-synthetic datasets which are created by adding noise from a passive dataset directly to synthetic traces (*Wang et al.*, 2008). In recent years this approach has been gaining popularity, particularly in the microseismic monitoring community where noise is exceptionally troublesome. *Forghani-Arani*

Table 1.3: *An overview of synthetic datasets developed which contain realistic, difficult challenges observed within field datasets.*

Dataset	Brief description	Reference
Marmousi	A dataset designed to break the reliance on the common assumptions of conventional processing whilst remaining geologically plausible.	*Bourgeois et al.* (1991)
Marmousi2	Elastic version of Marmousi made possible due to improvement in computational power.	*Martin et al.* (2006)
SEAM Phase I (subsalt)	Focussing on the deep water Gulf of Mexico, the dataset aims to address the challenges of subsalt imaging in Tertiary basins.	*Fehler and Keliher* (2011)
SEAM Phase II (land)	The dataset focusses on complexities that arise in land seismic surveys, such as high density and areal extensive acquisition geometries, near surface complexities, and fractured reservoir characterisation.	*Oristaglio* (2012)
SEAM Life of Field (in prog.)	In development, this is the first fully multidisciplinary reference dataset designed for the testing of interpretation procedures and software used in reservoir management.	*Oristaglio* (2016)
SMAART Pluto 1.5	Designed for wave-field investigations such as multiple suppression and depth imaging, the dataset is based on a deep water sub-salt prospect in the Gulf of Mexico.	*Stoughton et al.* (2001)
SMAART Sigsbee 2A	Based on the Sigsbee escarpment in the deep water Gulf of Mexico, the dataset focusses on illumination issues due to the complex salt body in the subsurface.	*Paffenholz et al.* (2002a)
SMAART Sigsbee 2B	Using the same structural model as SMAART Sigsbee 2A but with an increase of the velocity contrast at the water bottom (to a normal level) introduces significant internal and free-surface multiples.	*Paffenholz et al.* (2002b)

et al. (2012) used a semi-synthetic dataset to test their noise suppression algorithms for surface arrays, while *Chambers et al.* (2010) used semi-synthetics to test the ability of surface arrays for microseismic monitoring. Whilst providing a true incorporation of realistic noise, the dependence on the data selected to represent the noise is a major drawback. The available data segments are of finite length and do not allow for any 'tailoring' of the data, for example having a car pass the recording site at the same time as injection occurs.

Whilst these studies represent progression towards the inclusion of realistic noise in synthetic datasets, each technique has advantages and disadvantages, and no technique has yet to become the established method of incorporating realistic noise into synthetic datasets. The ultimate goal would be to not only propose a method for the incorporation of realistic noise but for the creation of open-source synthetic datasets that have been developed to break the reliance of the WGN assumption in seismology.

1.2.3 Noise suppression

By understanding a noise signal's unique characteristics and how these differ from those of the signal of interest, techniques can be developed that suppress the noise by exploiting such characteristics. Historically a number of suppression techniques have been developed in order to mitigate the effect of random, spike-like, and coherent noise signals. Generally these techniques can be split into three fundamental methodologies: transformation, adaptive subtraction, and projection.

Transformation techniques apply an operation which aims at transforming the noise while keeping the signal intact. Mean filtering is probably the simplest approach falling under this category and deals with random noise. It is a linear smoothing operator which reduces the high frequencies in the data, commonly assumed to be dominated by noise rather than signal (*Hall*, 2007). Being a linear operator, the mean filter works by convolution with a moving window of user defined size n over a portion of the signal of interest; the average value of the input signal within this window is assigned to the output signal at the center of the window. While the coefficients of the mean filter are constant throughout the extent of the filter, other common smoothing filters can have Gaussian or Triangular shape. As all samples (including outliers) have equal influence on the computation of the mean statistic, trimming the distribution of the signal within the selected window prior to computing the mean can ensure that extreme values have no influence on the output result. When this approach is applied to mean filtering, the filter becomes non-linear and it is generally referred to as α-Trimmed Mean filter (ATM), where α indicates the proportion of the distribution being truncated on either side of the median value. For $\alpha = 0$ (i.e., no truncation applied) ATM becomes a simple mean filter, while in the case of $\alpha = 0.5$ such filter is effectively extracting the median

value within the window of analysis (*Hoeber et al.*, 2006). Such a filter is commonly referred to as median filter and, in contrast to the mean filter, it is particularly effective for the suppression of spike-like noise. For this reason it also represents one of the most commonly used approaches to edge-preserving smoothing of digital images (*Hall*, 2007). In the seismic domain, *Liu et al.* (2008) successfully demonstrated the applicability of time-varying median filters for suppression of both spike-like and random noise on pre-stack noisy land data. While *Liu et al.* (2008)'s approach is an example of 1D implementation of median filters across the time axis, such filters can also be applied in a directional fashion as well as across multiple dimensions (e.g., time and offsets). For example, as discussed in *Duncan and Beresford* (1995), if the median filter is steered along the direction of a coherent wavefield of interest, both random noise and other events with different dips are attenuated. The process works because the median value of a continuous signal (i.e., the wavefield of interest) corrupted by noise is given approximately by the signal itself.

However, it is not always possible to perfectly isolate the signal of interest from noise. Combining transformation filters with adaptive subtraction techniques, sometimes referred to as match filtering, can provide a more robust approach to the suppression of coherent noise. Adaptive subtraction works by adaptively matching the initial noise model to the data to generate a better noise estimation prior to subtracting the enhanced model from the data (*Abma et al.*, 2005). *Hardage* (1983) and *Duncan and Beresford* (1995) both use dip-oriented median filters to isolate unwanted coherent wavefields (e.g., downgoing wavefields in VSP data) and subsequently subtract the filtered data from the original data in an adaptive manner. Other common applications of adaptive subtraction in processing of active seismic data are multiple attenuation (*Claerbout*, 1985) and simultaneous source separation (*Spitz et al.*, 2008) where the initial noise models are created using physics-based approaches; and the use of minimum power filters (*Douglas*, 1998) where the noise models are created based on statistics and used to compute the necessary spatial filters.

Projection techniques instead work by projecting the data onto a different domain, removing the noise and transforming back to the original domain. An example of one such technique is the use of filtering in the frequency-wavenumber (f-k) domain to remove scattered guided waves by exploiting the characteristically low velocity of the near surface (*Yilmaz*, 2001). Alternatively, if a Fourier transform is applied only to the time axis, filtering can be performed in the so-called f-x domain (*Canales et al.*, 1984, *Gulunay et al.*, 1986). This method lies its foundation on the idea that seismic wavefields with linear moveout manifest themselves in the f-x domain as superposition of harmonics. This justifies the use of prediction error filters in the spatial direction of the f-x domain to optimally extract linear features and suppress random noise. More specifically, for each frequency, an auto-regressive (AR) filter is predicted from and

applied to the spectrum of the data across multiple offsets. Finally the filtered spectrum for all frequencies is transformed back to the time-space domain. More recently, a variety of techniques commonly used in the field of image processing have also been applied to seismic data with the aim of enhancing the spatial coherence of seismic data. These techniques are based on the idea that seismic data (e.g., a common shot gather or a common midpoint gather) can be seen as a matrix $\mathbf{X}$ with N_t rows and N_x columns, where N_t and N_x are the number of time and space samples, respectively. One technique of such type is Singular Value Decomposition (SVD) filtering which decomposes the seismic data into a weighted linear combination of its eigenvectors, where the weights are represented by its eigenvalues:

$$\mathbf{X} = \mathbf{U}\Sigma\mathbf{V}^T = \sum_{i=1}^{N_x} \sigma_i \mathbf{u}_i \mathbf{v}_i^T \tag{1.5}$$

and where $\Sigma = diag\{\sigma_1, \sigma_2, ...\sigma_{N_x}\}$ is the matrix of eigenvalues and, $\mathbf{U} = [\mathbf{u}_1, \mathbf{u}_2, \cdots, \mathbf{u}_{N_x}]$ and $\mathbf{V} = [\mathbf{v}_1, \mathbf{v}_2, \cdots, \mathbf{v}_{N_x}]$ are the matrices of eigenvectors. (Where each eigenvector u_i is a column vector of size $N_t \times 1$ and each eigenvector v_i is a column vector of size $N_x \times 1$.)

By taking the first K eigenvectors of the original data, the data is partially restored as follows:

$$\hat{\mathbf{X}} = \sum_{i=1}^{K} \sigma_i \mathbf{u}_i \mathbf{v}_i^T \tag{1.6}$$

In other words, the strongest eigenvalues are retained as they are responsible for the generation of the part of the data with greater spatial coherence, while small eigenvalues are discarded as they are associated with the incoherent component of the data. SVD filtering can thus be seen as a multi-channel filtering method where each filtered trace maintains a certain degree of coherence with immediately neighbouring traces (*Freire and Ulrych*, 1988). As explained in *Bekara and Van der Baan* (2006), SVD works by finding a projection such that the signal component of the data belongs to a subspace which is orthogonal to the noise subspace. However, note that the orthogonality property of this projection is strictly valid only if the signal and the noise are uncorrelated.

Another eigen-decomposition technique called Independent Component Analysis (ICA) uses higher order statistics to look beyond uncorrelatedness and searches for statistical independence between the signal and noise. While applying an initial SVD on the covariance matrix of the data, ICA goes a step beyond by keeping the K largest eigenvectors and using them as *sources* for a source separation problem that is solved by using higher order statistics of the data (*Hyvärinen et al.*, 2001). Finally, another approach to noise suppression based on SVD is the so-called Cadzow filtering (*Cadzow*, 1988). Similar to f-x filtering, the original seismic data is initially transformed into the

f-x domain. At every temporal frequency, the N_x available samples are rearranged into a matrix $\mathbf{A}$ of size $m \times n$ where m is chosen to make the matrix as square as possible (ideally $m = n/2$). SVD is applied to the matrix, the first K largest eigenvalues are retained, and the matrix is rearranged into its original dimensions. This method has proven superior to f-x filtering and other projection techniques in preserving the strongest coherent components while suppresing the lower coherency components, generally attributed to noise (*Trickett et al.*, 2008).

Noise whitening is an example of a transformation technique which aims to transform coloured and/or coherent noise to incoherent, white noise. One produce of such a kind is proposed by *Liu et al.* (2017) which uses autocorrelation-based filters for microseismic event enhancement. By computing and stacking the autocorrelation function for each trace, a windowed version of the stack is used to define the denoising filter's impulse response prior to a truncation window being applied to the zero-lag region. This technique effectively suppresses uncorrelated noise without the requirement of knowing relative time offsets. However, it does not tackle noise correlation in space. In Chapter 4 an alternative approach to noise whitening is proposed. This technique differs from the previous one in that it considers correlation in both time and space simultaneously and it effectively reduces the coherency of noise in both directions. Utilising the covariance of the data, this technique aims to both reduce the overall noise level and whiten the remaining noise such that it conforms closer to the WGN assumption - an assumption under which a large number of algorithms are developed. Noise correlated in time and/or space is shown to be efficiently suppressed with the remaining noise transformed to contain little to no remaining correlation in either time or space.

The aim of any noise suppression technique is to efficiently remove noise whilst leaving the signal intact. To do this successfully it is important to have a clear understanding of the properties of both the signal of interest and the noise present. As detailed above, different noise signals require different suppression techniques so there is no one hard and fast solution to noise removal other than to identify the noise signals present in the data and design a processing flow incorporating all the necessary removal techniques.

To conclude, it is important to note that one person's noise is another person's signal. The majority of 'noise' has travelled through the subsurface and therefore contains information about the subsurface. In conventional seismic applications surface waves contain useful information about the near surface properties (*Socco et al.*, 2010) while multiples offer increased illumination and resolution of the subsurface (*Ravasi*, 2015). In passive monitoring, the Earth's ambient vibrations offer the opportunity to undertake tomography studies that are difficult to achieve with traditional seismic methods (*Nicolson et al.*, 2012), while the incorporation of primary reflections in microseismic monitoring results in a reduced source location uncertainty (*Belayouni et al.*, 2015). It is not just subsurface knowledge that can be gained from turning noise into signal.

Recordings of thunder on seismic recordings offer opportunities to gain a better understanding of the atmospheric electrical phenomenon of lighting (*Kappus and Vernon*, 1991). While *Riahi and Gerstoft* (2015) highlight the benefits of utilising low cost, seismic sensors for traffic monitoring. These studies illustrate the wealth of information that has up to now remained hidden in the noise.

1.3 Thesis Layout

Figure 1.8 provides a flow chart of the layout of this thesis, together with a summary of the main findings. Chapter 2 addresses the current state of noise models available for incorporating into synthetic dataset production. Through the use of a noise analysis of passive data collected at the Aquistore carbon dioxide (CO_2) storage site, this paper highlights the variability of noise and proposes a statistical modelling method to generate noise models which can portray all the separate noise signals present in a field dataset.

The ability to generate realistic noise models has many benefits, the first being the ability to test algorithms under realistic conditions whilst using synthetic datasets. Utilising the Isolated COVAriance (ICOVA) noise modelling method of Chapter 2, Chapter 3 highlights the ability of testing algorithms under realistic conditions through the comparison of how synthetic datasets with WGN and ICOVA noise perform on standard microseismic event detection and location procedures - as well as on an in-development moment tensor imaging algorithm. Using a semi-synthetic dataset to benchmark the results that would be expected if the images were run on a field dataset, the results highlighted that ICOVA noise provides a close comparison to the results obtained using recording noise, whereas the WGN results were prone to both over- and under-performing depending on the algorithm in question.

Another benefit is that by understanding the noise well enough to model it then suppression should be an achievable goal. Chapter 4 addresses this by building on the theory of Chapter 2; the inversion of the modelling procedure proves to be a robust tool for noise suppression, allowing imaging of microseismic events at previously unobtainable SNRs and reduce the overall noise level by a factor of 3.5.

The thesis concludes with a discussion on the future of the techniques developed in Chapters 2-4. Chapter 5 highlights the areas of future development required prior to the proposed techniques becoming common-place in the creation of synthetic datasets and gaining a place in geophysicists' noise-suppression arsenal.

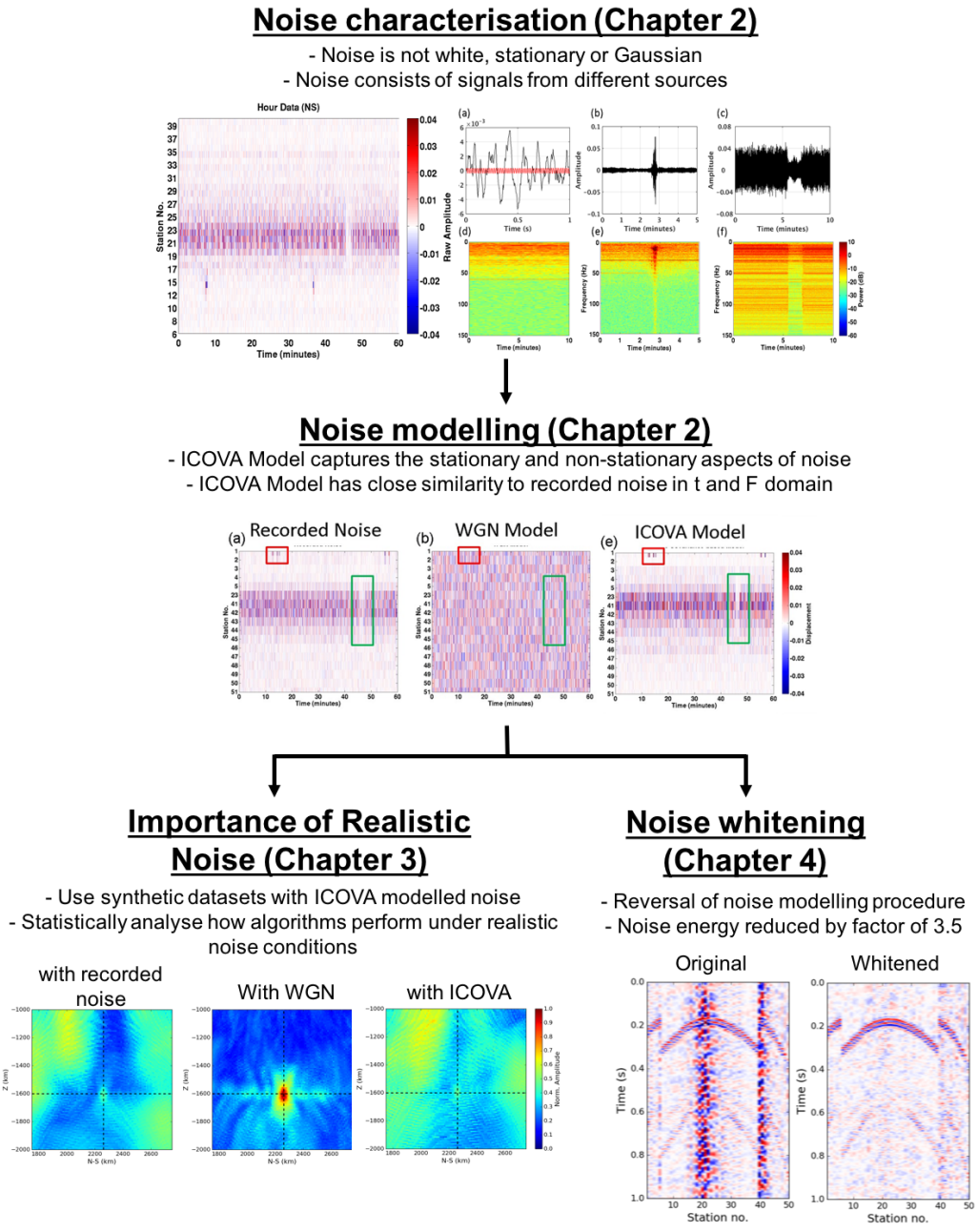

Figure 1.8: *Visual workflow and summary of the main findings of this thesis.*

References

Abercrombie, R. E. (1995), Earthquake source scaling relationships from- 1 to 5 ml using seismograms recorded at 2.5-km depth, *Journal of Geophysical Research: Solid Earth*, *100*(B12), 24,015–24,036. 1.2.1

Abercrombie, R. E. (1997), Near-surface attenuation and site effects from comparison of surface and deep borehole recordings, *Bulletin of the Seismological Society of America*, *87*(3), 731–744. 1.2.1

Abma, R., N. Kabir, K. H. Matson, S. Michell, S. A. Shaw, and B. McLain (2005), Comparisons of adaptive subtraction methods for multiple attenuation, *The Leading Edge*, *24*(3), 277–280. 1.2.3

Akbulut, K., O.-K. Saeland, P. Farmer, and T. Curtis (1984), Suppression of seismic interference noise on gulf of mexico data, in *1984 SEG Annual Meeting*. 1.2.1

Aki, K. (1969), Analysis of the seismic coda of local earthquakes as scattered waves, *Journal of geophysical research*, *74*(2), 615–631. 1.2.1

Aki, K., and B. Chouet (1975), Origin of coda waves: source, attenuation, and scattering effects, *Journal of geophysical research*, *80*(23), 3322–3342. 1.2.1

Aki, K., and P. Richards (1980), Quantitative seismology: Theory and methods, *W. H. Freeman, New York*. 1.2.1

Aki, K., and Y.-B. Tsai (1972), Mechanism of love-wave excitation by explosive sources, *Journal of Geophysical Research*, *77*(8), 1452–1475. 1.2.1

Alavès, N. (2012), Emergency management: Seismology to minimise aircraft crash location search time, Ph.D. thesis, University of Glasgow. 1.2.1

Aspinall, W., and F. Morgan (1983), A fatal aircraft crash detected by seismographs, *Bulletin of the Seismological Society of America*, *73*(2), 683–685. 1.2.1

Barajas-Olalde, C., and A. Jeffreys (2014), Seismic wind noise experiments using a portable wind tunnel, in *76th EAGE Conference and Exhibition 2014*. 1.2.1

Bardainne, T., E. Gaucher, F. Cerda, D. Drapeau, et al. (2009), Comparison of picking-based and waveform-based location methods of microseismic events: Application to a fracturing job, in *2009 SEG Annual Meeting*, Society of Exploration Geophysicists. 1.1

Bekara, M., and M. Van der Baan (2006), Local svd/ica for signal enhancement of pre-stack seismic data, in *68th EAGE Conference and Exhibition incorporating SPE EUROPEC 2006*. 1.2.3

Belayouni, N., A. Gesret, G. Daniel, and M. Noble (2015), Microseismic event location using the first and reflected arrivals, *GEOPHYSICS*, *80*, WC133–WC143. 1.2.3

Bertero, R. D., A. Lehmann, J. Mussat, and S. Vaquero (2012), Vibrations in neighborhood buildings due to rock concerts in stadiums, *Journal of Structural Engineering*, *139*(11), 1981–1991. 1.2.1

Bessason, B., G. Eiríksson, Ó. Thórarinsson, A. Thórarinsson, and S. Einarsson (2007), Automatic detection of avalanches and debris flows by seismic methods, *Journal of Glaciology*, *53*(182), 461–472. 1.2.1

Bland, H. C. (2006), An analysis of passive seismic recording performance, *CREWES Research Report*, *18*. 1.2.1

Bland, H. C., and E. V. Gallant (2001), Wind noise abatement for 3-c geophones, *Tech. rep.*, CREWES Research Report. 1.2.1

Bourgeois, A., M. Bourget, P. Lailly, M. Poulet, P. Ricarte, and R. Versteeg (1991), Marmousi, model and data, *The Marmousi Experience*, pp. 5–16. 1.2.2, 1.3

Budden, K. G. (1961), *The wave-guide mode theory of wave propagation*, Logos Press. 1.2.1

Burtin, A., L. Bollinger, J. Vergne, R. Cattin, and J. Nábělek (2008), Spectral analysis of seismic noise induced by rivers: A new tool to monitor spatiotemporal changes in stream hydrodynamics, *Journal of Geophysical Research: Solid Earth*, *113*(B5). 1.2.1

Butler, J. M. (1975), A study of seismic road noise, Ph.D. thesis, Georgia Institute of Technology. 1.2.1, 1.2

Butt, U. A., and T. Ishihara (2012), Seismic load evaluation of wind turbine support structures considering low structural damping and soil structure interaction, *European wind energy association annual event*, pp. 16–19. 1.2.1

Cadzow, J. A. (1988), Signal enhancement-a composite property mapping algorithm, *IEEE Transactions on Acoustics, Speech, and Signal Processing*, *36*(1), 49–62. 1.2.3

Canales, L. L., et al. (1984), Random noise reduction, in *1984 SEG Annual Meeting*, Society of Exploration Geophysicists. 1.2.3

Cates, J. E., and B. Sturtevant (2002), Seismic detection of sonic booms, *The journal of the acoustical society of America*, *111*(1), 614–628. 1.2.1

Celebi, M., J. Prince, C. Dietel, M. Onate, and G. Chavez (1987), The culprit in mexico cityamplification of motions, *Earthquake spectra*, *3*(2), 315–328. 1.2.1

Chambers, K., J. Kendall, S. Brandsberg-Dahl, J. Rueda, et al. (2010), Testing the ability of surface arrays to monitor microseismic activity, *Geophysical Prospecting*, *58*(5), 821–830. 1.2.2

Cheney, E., and D. Kincaid (2012), *Numerical mathematics and computing*, Nelson Education. 1.2.1

Claerbout, J. F. (1985), *Fundamentals of geophysical data processing*, Pennwell Books, Tulsa, OK. 1.2.3

Clark, R. (2018), personal communication. 1.2.1

Courant, R., K. Friedrichs, and H. Lewy (1967), On the partial difference equations of mathematical physics, *IBM journal of Research and Development*, *11*(2), 215–234. 1.2.1

Coward, D., D. Blair, R. Burman, and C. Zhao (2003), Vehicle-induced seismic effects at a gravitational wave observatory, *Review of scientific instruments*, *74*(11), 4846–4854. 1.2.1, 1.2

de Groot-Hedlin, C. D., M. A. Hedlin, K. T. Walker, D. P. Drob, and M. A. Zumberge (2008), Evaluation of infrasound signals from the shuttle atlantis using a large seismic network, *The Journal of the Acoustical Society of America*, *124*(3), 1442–1451. 1.2.1

Dean, T. (2017), The seismic signature of rain, *Geophysics*, *82*(5), 1–36. 1.2.1

Dean, T., J. C. Dupuis, and R. Hassan (2015), The coherency of ambient seismic noise recorded during land surveys and the resulting implications for the effectiveness of geophone arrays, *Geophysics*, *80*(3), P1–P10. 1.2.2

Degrande, G., D. Clouteau, R. Othman, M. Arnst, H. Chebli, R. Klein, P. Chatterjee, and B. Janssens (2006), A numerical model for ground-borne vibrations from underground railway traffic based on a periodic finite element–boundary element formulation, *Journal of Sound and Vibration*, *293*(3-5), 645–666. 1.2.1

Dent, R. (2013), What causes the noise emitted from high-voltage power lines–is it static discharge, vibration from the 60-cycle field or something else entirely? 1.2.1

Díaz, J., M. Ruiz, P. S. Sánchez-Pastor, and P. Romero (2017), Urban seismology: on the origin of earth vibrations within a city, *Scientific Reports*, *7*(1), 15,296. 1.2.1, 1.4

Douglas, A. (1998), Making the most of the recordings from short-period seismometer arrays, *Bulletin of the Seismological Society of America*, *88*(5), 1155–1170. 1.2.3

Drew, J., P. Primiero, K. Brook, D. Raymer, T. Probert, A. Kim, and D. Leslie (2012), Microseismic monitoring field test using surface, shallow grid and downhole arrays, in *SEG Expanded Abstracts*, vol. 31. 1.2.1

Duncan, G., and G. Beresford (1995), Median filter behaviour with seismic data, *Geophysical prospecting*, *43*(3), 329–345. 1.2.3

Eisner, L., D. Abbott, W. B. Barker, M. P. Thornton, and J. Lakings (2008), Noise suppression for detection and location of microseismic events using a matched filter, in *2008 SEG Annual Meeting*, Society of Exploration Geophysicists. 1.1

Eisner, L., P. M. Duncan, W. M. Heigl, and W. R. Keller (2009), Uncertainties in passive seismic monitoring, *The Leading Edge*, *28*(6), 648–655. 1.1

Ekström, G. (2001), Time domain analysis of earth's long-period background seismic radiation, *Journal of Geophysical Research: Solid Earth*, *106*(B11), 26,483–26,493. 1.2.1

Ekstrom, G., and S. Ekstrom (2005), Correlation of earth's long-period background seismic radiation with the height of ocean waves, in *AGU Fall Meeting Abstracts*. 1.2.1

El-Kaseeh, G., N. Banik, A. Koesoemadinata, M. Egan, and A. Salama (2010), Seismic feasibility tests in the williston basin to improve reservoir characterization, *first break*, *28*(6). 1.2.1, 1.2

Erlingsson, S., and A. Bodare (1996), Live load induced vibrations in ullevi stadium-dynamic dynamic soil analysis, *Soil Dynamics and Earthquake Engineering*, *15*(3), 171–188. 1.2.1

Ernst, F. E., G. C. Herman, and A. Ditzel (2002), Removal of scattered guided waves from seismic data, *Geophysics*, *67*(4), 1240–1248. 1.2.1

Evans, J. R., F. Followill, C. R. Hutt, R. Kromer, R. L. Nigbor, A. Ringler, J. Steim, and E. Wielandt (2010), Method for calculating self-noise spectra and operating ranges for seismographic inertial sensors and recorders, *Seismological Research Letters*, *81*(4), 640–646. 1.2.1

Fehler, M., and P. J. Keliher (2011), *SEAM Phase 1: Challenges of subsalt imaging in tertiary basins, with emphasis on deepwater Gulf of Mexico*, Society of Exploration Geophysicists. 1.3

Forghani-Arani, F. (2013), Analysis and suppression of passive noise in surface microseismic data, Ph.D. thesis, Colorado School of Mines. 1.1

Forghani-Arani, F., M. Batzle, J. Behura, M. Willis, S. S. Haines, and M. Davidson (2012), Noise suppression in surface microseismic data, *The Leading Edge*, *31*(1496–1501), 1496–1501. 1.2.2

Forghani-Arani, F., M. Willis, S. S. Haines, M. Batzle, J. Behura, and M. Davidson (2013), An effective noise-suppression technique for surface microseismic data, *Geophysics*, *78*(6), KS85–KS95. 1.2

Freire, S. L., and T. J. Ulrych (1988), Application of singular value decomposition to vertical seismic profiling, *Geophysics*, *53*(6), 778–785. 1.2.3

Friedrich, A., F. Krüger, and K. Klinge (1998), Ocean-generated microseismic noise located with the gräfenberg array, *Journal of Seismology*, *2*(1), 47–64. 1.2.1

Gabrielov, A., and V. Palamodov (1968), Huygens principle and its generalizations, *IG Petrovskii, Systems of partial differential equations. Algebraic geometry. Selected papers, Nauka, Moscow*. 1.2.1

Gherzi, E. (1924), Étude sur les microséismes, *Notes Seismol. Obs. Zi-Ka-Wei*, *5*. 1.2.1

Graizer, V., and E. Kalkan (2008), Response of pendulums to complex input ground motion, *Soil Dynamics and Earthquake Engineering*, *28*(8), 621–631. 1.2.1

Green, D. N., and D. Bowers (2008), Seismic raves: Tremor observations from an electronic dance music festival, *Seismological Research Letters*, *79*(4), 546–553. 1.2.1

Green, D. N., I. D. Bastow, B. Dashwood, and S. E. Nippress (2017), Characterizing broadband seismic noise in central london, *Seismological Research Letters*, *88*(1), 113–124. 1.2.1

Grover, F. (1973), Geophysical effects of concorde sonic boom, *Quarterly Journal of the Royal Astronomical Society*, *14*, 141. 1.2.1

Gulunay, N., M. Magesan, and S. Baldock (2004), Seismic interference noise attenuation, *74th Ann. Internat., Mtg., SEG, Expanded Abstracts*. 1.2.1

Gulunay, N., et al. (1986), Fxdecon and complex wiener prediction filter, in *1986 SEG Annual Meeting*, Society of Exploration Geophysicists. 1.2.3

Gurrola, H., J. Minster, H. Given, F. Vernon, J. Berger, and R. Aster (1990), Analysis of high-frequency seismic noise in the western united states and eastern kazakhstan, *Bulletin of the Seismological Society of America*, *80*(4), 951–970. 1.2.1

Hall, M. (2007), Smooth operator smoothing seismic interpretations and attributes, *The Leading Edge*, *26*(1), 16–20. 1.2.3

Hardage, B. A. (1983), *Vertical seismic profiling part a: Principles*, Geophysical Press. 1.2.3

Hardage, B. A. (2000), *Vertical seismic profiling: Principles*, vol. 14, Pergamon. 1.2.1, 1.6, 1.2.1

Hasselmann, K. (1963), A statistical analysis of the generation of microseisms, *Reviews of Geophysics*, *1*(2), 177–210. 1.2.1

Hayashi, K., D. R. Burns, and M. N. Toksz (2001), Discontinuous-grid finite-difference seismic modeling including surface topography, *Bulletin of the Seismological Society of America*, *91*(6), 1750–1764. 1.2.1

Heisler, G. M., and D. R. Dewalle (1988), Effects of windbreak structure on wind flow, in *Windbreak technology*, pp. 41–69, Elsevier. 1.2.1

Herrmann, R. B., and D. Russell (1990), Ground roll: Rejection using adaptive phase-matched filters, *Geophysics*, *55*(6), 776–781. 1.2.1

Hoeber, H., S. Brandwood, and D. Whitcombe (2006), Structurally consistent filtering, in *68th EAGE Conference and Exhibition incorporating SPE EUROPEC 2006*. 1.2.3

Holub, K. (1997), Some man-made sources of the seismic noise, *Acta Montana*, *107*, 83–98. 1.2

Huang, C.-J., H.-Y. Yin, C.-Y. Chen, C.-H. Yeh, and C.-L. Wang (2007), Ground vibrations produced by rock motions and debris flows, *Journal of Geophysical Research: Earth Surface*, *112*(F2). 1.2.1

Hyvärinen, A., J. Karhunen, and E. Oja (2001), *What is independent component analysis?*, Wiley Online Library. 1.2.3

Johnston, A. C. (1987), Air blast recognition and location using regional seismographic networks, *Bulletin of the Seismological Society of America*, *77*(4), 1446–1456. 1.2.1

Jurkevics, A., and R. Wiggins (1984), A critique of seismic deconvolution methods, *Geophysics*, *49*(12), 2109–2116. 1.1

Kahrizi, A., M. Emdadi, and H. Karslı (2014), Efficiency of complex trace analysis to attenuate ground-roll noise from seismic data, *Journal of Applied Geophysics*, *106*, 50–59. 1.2.1

Kainkwa, R., and C. Stigter (1994), Wind reduction downwind from a savanna woodland edge, *NJAS wageningen journal of life sciences*, *42*(2), 145–157. 1.2.1

Kappus, M. E., and F. L. Vernon (1991), Acoustic signature of thunder from seismic records, *Journal of Geophysical Research: Atmospheres*, *96*(D6), 10,989–11,006. 1.2.3

Kim, W.-Y., L. Sykes, J. Armitage, J. Xie, K. Jacob, P. Richards, M. West, F. Waldhauser, J. Armbruster, L. Seeber, et al. (2001), Seismic waves generated by aircraft impacts and building collapses at world trade center, new york city, *Eos, Transactions American Geophysical Union*, *82*(47), 565–571. 1.2.1

Knot, C. (1899), Reflection and refraction of elastic waves with seismological application, *Philos. Mag*, *5*, 64–97. 1.2.1

Kobayashi, N., and K. Nishida (1998), Continuous excitation of planetary free oscillations by atmospheric disturbances, *Nature*, *395*(6700), 357. 1.2.1

Kouroussis, G., N. Pauwels, P. Brux, C. Conti, and O. Verlinden (2014), A numerical analysis of the influence of tram characteristics and rail profile on railway traffic ground-borne noise and vibration in the brussels region, *Science of the Total Environment*, *482*, 452–460. 1.2.1, 1.3

Kristek, J., P. Moczo, and M. Galis (2010), Stable discontinuous staggered grid in the finite-difference modelling of seismic motion, *Geophysical Journal International*, *183*(3), 1401–1407. 1.2.1

Lailly, P., and R. Versteeg (1990), The marmousi workshop-introduction, in *EAEG Workshop-Practical Aspects of Seismic Data Inversion*. 1.1

Lamb, H. (1904), On the propagation of tremors over the surface of an elastic solid, *Philosophical Transactions of the Royal Society of London. Series A, Containing Papers of a Mathematical or Physical Character*, pp. 1–42. 1.2.1

Langston, C. A. (2004), Seismic ground motions from a bolide shock wave, *Journal of Geophysical Research: Solid Earth*, *109*(B12). 1.2.1

Legerton, M., D. Manley, J. Sargent, D. Snow, and P. Styles (1996), Low frequency noise & vibration levels at a modern wind farm, in *International congress on noise control engineering*, pp. 459–462. 1.2.1

Li, Y.-G., K. Aki, D. Adams, A. Hasemi, and W. H. Lee (1994), Seismic guided waves trapped in the fault zone of the landers, california, earthquake of 1992, *Journal of Geophysical Research: Solid Earth (1978–2012)*, *99*(B6), 11,705–11,722. 1.2.1

Lilla, A. d. (1997), Finite difference seismic wave propagation using variable grid sizes, Ph.D. thesis, Massachusetts Institute of Technology. 1.2.1

Liu, E., L. Zhu, A. Govinda Raj, J. H. McClellan, A. Al-Shuhail, S. I. Kaka, and N. Iqbal (2017), Microseismic events enhancement and detection in sensor arrays using autocorrelation-based filtering, *Geophysical Prospecting*. 1.2.3

Liu, Y., C. Liu, and D. Wang (2008), A 1d time-varying median filter for seismic random, spike-like noise elimination, *Geophysics*, *74*(1), V17–V24. 1.2.3

Lombaert, G., and G. Degrande (2001), Experimental validation of a numerical prediction model for free field traffic induced vibrations by in situ experiments, *Soil Dynamics and Earthquake Engineering*, *21*(6), 485–497. 1.2

Lombaert, G., G. Degrande, S. François, and D. Thompson (2015), Ground-borne vibration due to railway traffic: a review of excitation mechanisms, prediction methods and mitigation measures, in *Noise and vibration mitigation for rail transportation systems*, pp. 253–287, Springer. 1.2.1

Long, L. (1993), Measurements of seismic road vibrations. 1.2

Longuet-Higgins, M. S. (1950), A theory of the origin of microseisms, *Philosophical Transactions of the Royal Society of London. Series A, Mathematical and Physical Sciences*, *243*(857), 1–35. 1.2.1

Malone, S., K. Hall, L. Simmons, and J. Vidale (2015), How to recognize a beast quake and a dance quake, *Seismological Research Letters*, *86*(3), 1006–1008. 1.2.1, 1.5

Martin, G. S., R. Wiley, and K. J. Marfurt (2006), Marmousi2: An elastic upgrade for marmousi, *The Leading Edge*, *25*(2), 156–166. 1.3

Maxwell, S. (2014), *Microseismic Imaging of Hydraulic Fracturing: Improved Engineering of Unconventional Shale Reservoirs*, 17, SEG Books. 1.1

McNamara, D., C. Hutt, L. Gee, H. M. Benz, and R. Buland (2009), A method to establish seismic noise baselines for automated station assessment, *Seismological Research Letters*, *80*(4), 628–637. 1.2.1

Meunier, J. (2011), *Seismic acquisition from yesterday to tomorrow*, Society of Exploration Geophysicists. 1.2

Morse, P. F., and G. F. Hildebrandt (1989), Ground-roll suppression by the stackarray, *Geophysics*, *54*(3), 290–301. 1.2.1

Nakata, N., R. Snieder, T. Tsuji, K. Larner, and T. Matsuoka (2011), Shear wave imaging from traffic noise using seismic interferometry by cross-coherenceshear wave imaging from traffic noise, *Geophysics*, *76*(6), SA97–SA106. 1.2.1

Nicolson, H., A. Curtis, B. Baptie, and E. Galetti (2012), Seismic interferometry and ambient noise tomography in the british isles, *Proceedings of the Geologists' Association*, *123*(1), 74–86. 1.2.3

Nishida, K., N. Kobayashi, and Y. Fukao (2000), Resonant oscillations between the solid earth and the atmosphere, *Science*, *287*(5461), 2244–2246. 1.2.1

Nishida, K., N. Kobayashi, and Y. Fukao (2002), Origin of earth's ground noise from 2 to 20 mhz, *Geophysical Research Letters*, *29*(10). 1.2.1

Nørmark, E. (2011), Wind and rain induced noise on reflection seismic data, in *Near Surface 2011-the 17th European Meeting of Environmental and Engineering Geophysics*. 1.2.1, 1.2.1

Oristaglio, M. (2012), Seam phase ii - land seismic challenges, *The Leading Edge*, *31*(3), 264–266. 1.3

Oristaglio, M. (2016), Seam update: Integrated reservoir and geophysical modeling: Seam time lapse and seam life of field, *The Leading Edge*, *35*(10), 912–915. 1.3

Owen, A. (2003), Open all hours for seismic action, in *AusGEO News 70*, Geoscience Australia. 1.2.1

Paffenholz, J., B. McLain, J. Zaske, and P. J. Keliher (2002a), Subsalt multiple attenuation and imaging: Observations from the sigsbee2b synthetic dataset, in *2002 SEG Annual Meeting*, Society of Exploration Geophysicists. 1.3

Paffenholz, J., B. McLain, J. Zaske, and P. J. Keliher (2002b), Subsalt multiple attenuation and imaging: Observations from the sigsbee2b synthetic dataset, in *SEG Technical Program Expanded Abstracts 2002*, pp. 2122–2125, Society of Exploration Geophysicists. 1.3

Pearce, R., and B. Barley (1977), The effect of noise on seismograms, *Geophysical Journal International*, *48*(3), 543–547. 1.2.2

Peck, L. (2008), Overview of seismic noise and it's relevance to personnel detection, *Tech. rep.*, ENGINEER RESEARCH AND DEVELOPMENT CENTER HANOVER NH COLD REGIONS RESEARCH AND ENGINEERING LAB. (document), 1.2.1, 1.2

Perelberg, A. I., and S. C. Hornbostel (1994), Applications of seismic polarization analysis, *Geophysics*, *59*(1), 119–130. 1.2.1

Pino, N., M. Ripepe, and G. Cimini (2004), The stromboli volcano landslides of december 2002: A seismological description, *Geophysical Research Letters*, *31*(2). 1.2.1

Ravasi, M. (2015), Reciprocity-based imaging using multiply scattered waves, Ph.D. thesis, School of Geosciences, The University of Edinburgh. 1.2.3

Riahi, N., and P. Gerstoft (2015), The seismic traffic footprint: Tracking trains, aircraft, and cars seismically, *Geophysical Research Letters*, *42*(8), 2674–2681. 1.2.3

Riahi, N., A. Goertz, B. Birkelo, and E. H. Saenger (2013), A statistical strategy for ambient seismic wavefield analysis: investigating correlations to a hydrocarbon reservoir, *Geophysical Journal International*, *192*(1), 148–162. 1.2.1

Riedesel, M. A., J. A. Orcutt, and R. D. Moore (1990), Limits of sensitivity of inertial seismometers with velocity transducers and electronic amplifiers, *Bulletin of the Seismological Society of America*, *80*(6A), 1725–1752. 1.2.1

Rodgers, P. (1966), A phase sensitive parametric seismometer, *Bulletin of the Seismological Society of America*, *56*(4), 947–959. 1.2.1

Rodgers, P. W. (1992), Frequency limits for seismometers as determined from signal-to-noise ratios. part 1. the electromagnetic seismometer, *Bulletin of the Seismological Society of America*, *82*(2), 1071–1098. 1.2.1, 1.2.1, 1.2.1

Romanowicz, B., J. Rhie, and B. Colas (2005), Insights into the origin of the earth's hum and microseisms. fos 86 (52), fall meet, *Suppl. abstr. S31A-0271*. 1.2.1

Schilke, S., T. Probert, I. Bradford, A. Özbek, and J. Robertsson (2014), Use of surface seismic patches for hydraulic fracture monitoring, in *76th EAGE Conference and Exhibition 2014*. 1.2.1, 1.2.1

Schofield, R. (2001), Seismic measurements at the stateline wind project, *Rept No LIGO T020104-00-/, Laser Interferometer Gravitational Wave Observatory available at http://www. ligo. caltech. edu/docs*. 1.2.1

Schofield, R., M. Ito, E. Mauceli, H. Radkins, C. Gray, G. Moreno, and G. Gonzalez (2000), Source and propagation of the predominant 1-50 hz seismic signal from off-site at ligo-hanford, in *LIGO Scientific Collaboration Meeting, Hanford*. 1.2

Shalev, E., P. E. Malin, and W. McCausland (2002), Cutting costs by locating high production wells: A test of the volcano seismic approach to finding"blind"resources, *Tech. rep.*, Office of Research Support Duke University (US). 1.2.1

Socco, L. V., S. Foti, and D. Boiero (2010), Surface-wave analysis for building near-surface velocity modelsestablished approaches and new perspectives, *Geophysics*, *75*(5), 75A83–75A102. 1.2.3

Spitz, S., G. Hampson, and A. Pica (2008), Simultaneous source separation: A prediction-subtraction approach, in *SEG Technical Program Expanded Abstracts 2008*, pp. 2811–2815, Society of Exploration Geophysicists. 1.2.3

Stone, J., and J. Bouska (2013), Distance separated simultaneous sweeping, providing record-breaking productivity and a step-change in data quality in bp jordan's risha seismic survey, *First Break*, *31*(12), 53–60. 1.2.1

Stoughton, D., J. Stefani, and S. Michell (2001), 2d elastic model for wavefield investigations of subsalt objectives, deep water gulf of mexico, in *SEG Technical Program Expanded Abstracts 2001*, pp. 1269–1272, Society of Exploration Geophysicists. 1.3

Styles, P., I. Stimpson, S. Toon, R. England, and M. Wright (2005), Microseismic and infrasound monitoring of low frequency noise and vibrations from windfarms, *Recommendations on the Siting of Windfarms in the Vicinity of Eskdalemuir, Scotland, Report to MOD/FTI/BWEA, 125pp*. 1.2.1

Sylvette, B.-C., C. Cécile, B. Pierre-Yves, C. Fabrice, M. Peter, K. Jozef, and D. Fäh (2006), H/v ratio: a tool for site effects evaluation. results from 1-d noise simulations, *Geophysical Journal International*, *167*(2), 827–837. 1.2.2

Tarantola, A. (2005), Inverse problem theory and model parameter estimation: Siam, *Tech. rep.*, ISBN 978-0-89871-572-9. 1.2.1

Tasič, I., and F. Runovc (2012), Seismometer self-noise estimation using a single reference instrument, *Journal of seismology*, *16*(2), 183–194. 1.2.1

Tikhonov, A., A. Goncharsky, V. Stepanov, and A. G. Yagola (2013), *Numerical methods for the solution of ill-posed problems*, Springer Science & Business Media. 1.2.1

Trickett, S., et al. (2008), F-xy cadzow noise suppression, in *2008 SEG Annual Meeting*, Society of Exploration Geophysicists. 1.2.3

Tuñgol, N. M., and M. T. M. Regalado (1996), Rainfall, acoustic flow monitor records, and observed lahars of the sacobia river in 1992, *Fire and Mud: Eruptions and Lahars of Mount Pinatubo, Philippines*, pp. 1023–1032. 1.2.1

Ulrych, T., S. Taylor, B. Nedilko, and I. Weir-Jones (2009), Noise , the what , the where and the how to, in *Shiraz 2009 - First International Petroleum Conference & Exhibition*. 1.1, 1.2

Ulrych, T. J., M. D. Sacchi, and J. M. Graul (1999), Signal and noise separation: Art and science, *Geophysics*, *64*(5), 1648–1656. 1.1, 1.2

Vavryčuk, V. (2007), On the retrieval of moment tensors from borehole data, *Geophysical Prospecting*, *55*(3), 381–391. 1.2

Verdon, J. P., J.-M. Kendall, A. C. Horleston, and A. L. Stork (2016), Subsurface fluid injection and induced seismicity in southeast saskatchewan, *International Journal of Greenhouse Gas Control*, *54*, 429–440. 1.2.1

Vidale, J. E. (2011), Seattle 12th man earthquake goes viral, *Seismological Research Letters*, *82*(3), 449–450. 1.2.1

Walsh, B., A. Jolly, and J. Procter (2016), Seismic analysis of the 13 october 2012 te maari, new zealand, lake breakout lahar: Insights into flow dynamics and the implications on mass flow monitoring, *Journal of Volcanology and Geothermal Research*, *324*, 144–155. 1.2.1

Wang, J., F. Tilmann, R. White, H. Soosalu, and P. Bordoni (2008), Application of multichannel wiener filters to the suppression of ambient seismic noise in passive seismic arrays, *The Leading Edge*, *27*(2), 232–238. 1.2.2

Weaver, R. L. (2005), Information from seismic noise, *Science*, *307*(5715), 1568–1569. 1.2.1

Webb, S. C. (2007), The earths humis driven by ocean waves over the continental shelves, *Nature*, *445*(7129), 754. 1.2.1

Westwood, R. F., P. Styles, and S. M. Toon (2015), Seismic monitoring and vibrational characterization of small wind turbines: A case study of the potential effects on the eskdalemuir international monitoring system station in scotland, *Near Surface Geophysics*, *13*(2), 115–126. 1.2.1

Wiechert, E. (1904), Discussion,{Verhandlung der zweiten Internationalen Seismologischen Konferenz}, *Beitrage zur Geophysik*, *2*, 41–43. 1.2.1

Wilcock, W. S., S. C. Webb, and I. T. Bjarnason (1999), The effect of local wind on seismic noise near 1 hz at the melt site and in iceland, *Bulletin of the Seismological Society of America*, *89*(6), 1543–1557. 1.2.1

Witten, B., and B. Artman (2011), Signal-to-noise estimates of time-reverse images, *Geophysics*, *76*(2), MA1–MA10. 1.1

Woith, H., S. Parolai, T. Boxberger, M. Picozzi, Ö. T. Özmen, C. Milkereit, B. G. Lühr, and J. Zschau (2014), Spatio-temporal variability of seismic noise above a geothermal reservoir, *Journal of Applied Geophysics*, *106*, 128–138. 1.1

Wurman, G., E. A. Haering Jr, and M. J. Price (2011), The effect of sonic booms on earthquake warning systems. 1.2.1

Xia, J., and R. D. Miller (2000), Design of a hum filter for suppressing power-line noise in seismic data, *Journal of Environmental & Engineering Geophysics*, *5*(2), 31–38. 1.2.1

Xuan, R., and P. Sava (2010), Probabilistic microearthquake location for reservoir monitoring, *Geophysics*, *75*(3), MA9–MA26. 1.1

Yamada, M., H. Kumagai, Y. Matsushi, and T. Matsuzawa (2013), Dynamic landslide processes revealed by broadband seismic records, *Geophysical Research Letters*, *40*(12), 2998–3002. 1.2.1

Yilmaz, Ö. (2001), *Seismic data analysis*, vol. 1, Society of Exploration Geophysicists Tulsa. 1.2.3

Yuan, X., R. Kind, and H. A. Pedersen (2005), Seismic monitoring of the indian ocean tsunami, *Geophysical research letters*, *32*(15). 1.2.1

Zhang, J., P. Gerstoft, and P. M. Shearer (2009), High-frequency p-wave seismic noise driven by ocean winds, *Geophysical Research Letters*, *36*(9). 1.2.1, 1.2

Zoeppritz, K. (1919), Vii b. über reflexion und durchgang seismischer wellen durch unstetigkeitsflächen, *Nachrichten von der Gesellschaft der Wissenschaften zu Göttingen, Mathematisch-Physikalische Klasse*, *1919*, 66–84. 1.2.1

Chapter 2

Analysis and models of pre-injection surface seismic array noise recorded at the Aquistore carbon storage site

Claire Birnie[1], Kit Chambers [2], Doug Angus [1], and Anna L. Stork [3]

[1] *School of Earth and Environment, University of Leeds, United Kingdom*
[2] *Nanometrics Inc., United Kingdom*
[3] *School of Earth Sciences, University of Bristol, UK*

This chapter is an adaptation of the paper:
Birnie, C., Chambers, K., Angus, D. and Stork, A.L., 2016. Analysis and models of pre-injection surface seismic array noise recorded at the Aquistore carbon storage site. *Geophysical Journal International*, 206(2), pp.1246-1260. doi:10.1093/gji/ggw203

The following adaptations have been made to the submitted version:

1. Figure 2.2 has been edited and enlarged to allow easier identification of receivers and wells, and
2. an additional histogram has been added, to show observed distribution extremes.

Abstract

Noise is a persistent feature in seismic data and so poses challenges in extracting increased accuracy in seismic images and physical interpretation of the subsurface. In this paper, we analyse passive seismic data from the Aquistore carbon capture and storage pilot project permanent seismic array to characterise, classify and model seismic noise. We perform noise analysis for a three month subset of passive seismic data from the array and provide conclusive evidence that the noise field is not white, stationary, or Gaussian; characteristics commonly yet erroneously assumed in most conventional noise models. We introduce a novel noise modelling method that provides a significantly more accurate characterisation of real seismic noise compared to conventional methods, which is quantified using the Mann-Whitney-White statistical test. This method is based on a statistical covariance modelling approach created through the modelling of individual noise signals. The identification of individual noise signals, broadly classified as stationary, pseudo-stationary and non-stationary, provides a basis on which to build an appropriate spatial and temporal noise field model. Furthermore, we have developed a workflow to incorporate realistic noise models within synthetic seismic datasets providing an opportunity to test and analyse detection and imaging algorithms under realistic noise conditions.

2.1 Introduction

Noise is an inevitable feature of seismic data, given that the earth is dynamic, instruments are not perfect and our understanding of physics is still not complete such that even signals originating from the desired source can prove problematic for seismic processing (i.e., mulitples or ground roll) (e.g., *Li et al.*, 1994, *Kahrizi et al.*, 2014). For passive seismic data, noise is even more problematic due to the inherent uncertainty in the temporal and spatial location of seismic events. Furthermore, the masking of relatively weak microseismic events by noise leads to one of the main issues in passive seismic monitoring which is increased uncertainty in identifying event arrivals (*Bardainne et al.*, 2009, *Maxwell*, 2014). The presence of coherent noise in seismic imaging can result in the introduction of artefacts, while in seismic inversion it can lead to errors in the estimated velocity model and predicted source parameters (*Forghani-Arani*, 2013). Synthetic seismic datasets provide a confidence limit under which passive seismic processing and imaging algorithms can be used to accurately identify an event (e.g., *Price et al.*, 2015) and its failure mechanism (e.g., *Trifu et al.*, 2000), such as fracture location, orientation and length. To provide more realistic synthetic seismic data, noise with Gaussian characteristics is commonly added. Over the past few decades, the Gaussian noise assumption has resulted in many techniques being developed specifically to

suppress Gaussian noise (e.g., *Green et al.*, 1966, *Berkner and Wells Jr*, 1998, *Bekara et al.*, 2003). However, the choice of Gaussian noise is mainly to simplify implementation or demonstrate mathematical properties such as optimality and unbiasedness, rather than based upon physical principles. In many ways, Gaussian noise only serves to obscure seismic arrivals or events rather than providing a sufficiently robust test of processing and imaging algorithms.

What is noise? For passive seismic monitoring scenarios, every recorded signal other than the first arrival P and S waves is typically considered noise, such as ambient noise as well as seismic multiples and mode conversions. Ambient noise, sometimes referred to as background noise, originates from a wide range of sources that can be separated into natural processes and anthropogenic activities, dependent on their frequency content (*Gutenberg*, 1958, *Asten*, 1978). Noise below 1 Hz consists of microseisms created by large-scale meteorological events and oceanic waves along the coast (*Asten and Henstridge*, 1984). Between 1 and 5 Hz noise sources are likely to be local meteorological events or urban activity and sources above 5 Hz sources are likely to be urban in origin (*Bonnefoy-Claudet et al.*, 2006). Studies of meteorological noise suggest that wind and rain can have a distinct effect on the noise signature of seismic data (e.g., *Nørmark*, 2011, *Barajas-Olalde and Jeffreys*, 2014). In terms of anthropogenic noise, *Riahi and Gerstoft* (2015) characterised the seismic footprint of traffic and were able to distinguish sources such as trains, aircraft and road traffic. In addition to ambient and urban noise in many oil and gas producing environments there is also production-induced noise resulting from fluid extraction and injection processes. For hydraulic fracture monitoring pumping noise is pervalent, where increased noise levels are observed at stations closer to treatment wells (e.g., *Drew et al.*, 2012, *Schilke et al.*, 2014) broadly above the expected induced seismicity. It should be noted, however, that ambient noise interferometry on passive seismic data has been used increasingly to image subsurface velocity distributions (e.g., *Draganov et al.*, 2004) and recently multiples are being used to improve event location algorithms (e.g., *Belayouni et al.*, 2015).

Noise analyses have also focussed on noise characteristics (rather than their origin) by investigating the stationarity and Gaussianity of the noise field. A stationary time series is defined to have a constant mean and variance while a Gaussian time series must arise from a Gaussian distribution determined by the mean and variance. In this paper, we note that the terms stationarity and 'Gaussianity' refer to a measure by which a time series is stationary or Gaussian, respectively. It is commonly accepted that noise can only be assumed stationary over a short time period (*Riahi et al.*, 2013) due to contamination of stationary background noise by transient phenomena that are non-stationary in both time and space, such as urban seismic noise (*Groos and Ritter*, 2009). Advancements in signal processing have led to the use of noise surrogates to test the stationarity of a time series and provided an index on the strength of stationarity

that a time-series exhibits (*Borgnat et al.*, 2010). The use of surrogates has been applied to study background noise in land-seismic prospecting by *Zhong et al.* (2015) who concluded that background noise is "not strictly stationary" and as the length of time of the sample increases the stationarity decreases.

The assumption that background noise is Gaussian has gone relatively uncontested since *White* (1984) discussed the difficulty in testing unambiguously whether seismic noise is Gaussian. A recent investigation by *Zhong et al.* (2015) used a higher-order spectral analysis method to investigate Gaussianity of background noise with respect to time. They concluded that for periods over 20 seconds noise appears to be Gaussian whereas for periods of the order of 1 second noise is non-Gaussian. *Pierce* (1997) proposed that seismic noise is likely to have heavier tails than a Gaussian distribution and therefore may be more likely to follow an alpha-stable distribution (note that Gaussian distribution is a subset of an alpha-stable distribution with $\alpha = 2$).

Despite the evidence that noise does not conform to the white, Gaussian noise (WGN) assumption (see next section for definitions), the majority of published approaches still use WGN to test the robustness of event imaging and detection algorithms with respect to noise (e.g., *Grion et al.*, 2015, *Berkhout and Blacquière*, 2015, *Shao et al.*, 2015, *Trojanowski and Eisner*, 2015). *Pearce and Barley* (1977) included the effect of noise on synthetic seismograms by convolving a sample of recorded noise with broadband white noise creating coloured, Gaussian noise as opposed to the simple WGN approach. However, this approach only serves to produce a distorted signal by weighting the sampled recorded noise by a signal having Gaussian distribution and so is not meaningful. A more deterministic noise modelling method is that of distributed surface sources where source properties, such as direction, amplitude and source time functions, are randomly distributed (e.g., *Sylvette et al.*, 2006, *Lunedei and Albarello*, 2015, *Dean et al.*, 2015). While this modelling method provides significant improvements on the WGN modelling assumption, it is a theoretical modelling method independent of recorded noise and therefore has limitations to the extent to which it can model the complex properties of recorded noise. This is discussed by *Dean et al.* (2015) who state "Although the modeled data have the same characteristics as the field measurements, it is unlikely that models can be built with the geologic, geographic, and meteorological detail required to create accurate models". A recent advancement in representing realistic noise in synthetic datasets is to directly incorporate a sample of recorded noise into the synthetic dataset (referred to as a 'cut-and-paste' job). This technique leads to a so-called semi-synthetic dataset and can be used for robustness tests as shown by *Chambers et al.* (2010) and *Forghani-Arani et al.* (2012). Although the semi-synthetic approach provides sufficient realism, it does not allow one to modify the temporal and spatial statistical characteristics of noise in a methodological manner. Furthermore, it requires having real noise recorded from the array, where in many cases it may be

desirable to simulate noise levels prior to acquisition.

Since processing and imaging algorithms tend to be tested under a WGN assumption, it is often unclear how an algorithm will handle noise from a field dataset, leading to uncertainty in the accuracy of identified events and their derived properties. In this paper we investigate statistical methods for analysing noise properties and introduce a new modelling approach for seismic noise. We begin with a theoretical description of how noise is characterised before describing three existing techniques for noise simulation. We also propose a new modelling approach (ICOVA) based on the covariance modelling method. We then analyse and compare noise models against observations from three months of passive seismic data collected at the Aquistore carbon storage site. We observe and confirm that noise does not conform to the stationary, white, and Gaussian assumptions typically used by traditional noise modelling methods. We find that whilst the existing approaches fail to adequately simulate the noise characteristics due to their constraining assumptions the new ICOVA modelling approach provides more faithful representations for the noise field. The results of this study have possible implications for the design and implementation of noise cancellation and detection algorithms, the development of more robust noise models as well as improved survey designs. The relevance of more realistic noise modelling is potentially not limited to passive seismic applications and has potential for active source surface reflection and time-lapse seismic applications.

2.2 Theory

The traditional WGN modelling method assumes noise conforms to all of the following statistical properties:

1. **stationary** requiring that the first and second mathematical moments (mean and variance, respectively) are constant over the sample dimension in which stationarity is being determined,
2. exhibits a **white power spectrum** requiring the noise to have a constant power spectral density (PSD), such that energy is distributed equally across all frequencies, and
3. **Gaussian** requiring the noise to have a probability density function equal to that of a single-variate Gaussian distribution and therefore the distribution can be completely described by only the first and second mathematical moments.

The first section discusses the methods used to investigate whether noise conforms to the aforementioned assumptions. The second section details some of the common statistical noise modelling techniques, where we introduce some new techniques to characterise the noise field.

2.2.1 Noise characterisation

If noise is spatially and temporally stationary, the signal should display a constant mean and variance in both space and time coordinates. We compute the mean and variance using a sliding window analysis with a window length of 5 seconds and a window overlap of half the window length. The analysis window is chosen to correspond with those used in surface microseismic applications, which wish to contain a P-wave moveout across the array (1-2 seconds) and allow an additional buffer either side of the window. The window size and overlap enables capturing of any rapid changes in mean and variance in the data. Although a short window increases the computational expense, a longer window would smooth the results and lose important spatial and temporal resolution at the expense of computational efficiency.

To consider whether the noise power spectrum is white, we compute the PSD over an hour period and a short-time Fourier Transform (STFT) using the same sliding window analysis as done with the mean and variance calculations. The PSD characterises the overall power spectrum over a full hour whereas the STFT characterises any changes in the power spectrum over a much smaller time scale. To consider if the total energy is distributed equally across the array, the seismic energy (i.e. the squared amplitude) is computed using the same sliding window analysis as done with the STFT calculation.

The final noise property analysed is the extent to which the seismic noise is Gaussian. We consider only two methods to determine the distribution shape of seismic noise. Both techniques are based on the third and fourth mathematical moments that describe the skewness and kurtosis (i.e., 'peakedness') of a distribution, respectively. The first technique is performed in the time domain and uses the mathematical moments directly, while the second technique is performed in the frequency domain and uses cumulants.

The first technique is the conventional method of statistical moments. The first and second moments are the well known mean and variance, respectively, and the third and fourth moments are skewness and kurtosis, respectively. Skewness (γ_1) and kurtosis (γ_2) are defined:

$$\gamma_1 = \frac{\mu_3}{\sigma^3} = \frac{E[(x-\mu)^3]}{E[(x-\mu)^2]^{3/2}} \tag{2.1}$$

and

$$\gamma_2 = \frac{\mu_4}{\sigma^4} = \frac{E[(x-\mu)^4]}{E[(x-\mu)^2]^2}, \tag{2.2}$$

where x is a data point, μ_i is the ith mathematical moment, and $E[\cdot]$ denotes the expectation operator. For simplicity and to follow common naming conventions, μ is the first mathematical moment (i.e., mean) and σ is standard deviation (i.e., the square root of the second mathematical moment). For a Gaussian distribution, both skewness and excess kurtosis are equal to zero, where excess kurtosis is defined as $\gamma_{2_{ex}} = \gamma_2 - 3$.

The moments are calculated using the same sliding window analysis as performed on the stationarity test for mean and variance.

An extension to the conventional method of statistical moments is the analysis of cumulants and is performed using Higher Order Spectral Analysis (HOSA) and are commonly used in statistical signal processing (e.g., *Bartelt et al.*, 1984, *Walden and Williams*, 1993, *Pflug*, 2000). The HOSA method applied here considers the bispectrum and trispectrum, which are the Fourier transforms of the third- and fourth-order cumulants, respectively. Cumulants are an alternative to mathematical moments and arise from the natural logarithm of the mathematical moments (*Fisher*, 1930). By using cumulants the dependence on lower order moments (i.e., mean and variance) is removed (*Collis et al.*, 1998). The squared magnitude of the normalised bispectrums and trispectrums results in the bicoherence ($\hat{b}^2$) and tricoherence ($\hat{t}^2$), respectively:

$$\hat{b}^2(f_1, f_2) = \frac{|\frac{1}{N}\sum_{i=1}^{N}[X_i(f_1)X_i(f_2)X_i^*(f_1+f_2)]|^2}{\hat{P}(f_1)\hat{P}(f_2)\hat{P}(f_1+f_2)}, \tag{2.3}$$

and

$$\hat{t}^2(f_1, f_2, f_3) = \frac{|\frac{1}{N}\sum_{i=1}^{N}[X_i(f_1)X_i(f_2)X_i(f_3)X_i^*(f_1+f_2+f_3)]|^2}{\hat{P}(f_1)\hat{P}(f_2)\hat{P}(f_3)\hat{P}(f_1+f_2+f_3)}, \tag{2.4}$$

where $\hat{P}(f) = < X(f)X^*(f) >$ (<> denotes the expectation estimator), X is the Fourier transform of a time-series x, and X^* is the complex conjugate of X.

Both equations 2.3 and 2.4 are zero for Gaussian distributions and can reach a maximum of one for non-Gaussian distributions (*Chandran et al.*, 1994). The coherence calculations require N realisations of the distribution and compute a value for every possible frequency combination of f_1 and f_2 for bicoherence and f_1, f_2 and f_3 for tricoherence. To get a single value of coherence with respect to space and time the full coherence array for a time window at one position in space is averaged. The coherence analysis is computed on an hour of data using a 2 second realisation window and 30 realisations per calculation (i.e., one coherence value per minute of data). To provide a benchmark for the computed values, a Gaussian surrogate noise is created using the mean and variance of each data sample used to compute the Gaussianity property. (Note that this method of creating surrogates differs from that commonly used in communication theory which is performed in the frequency domain, see for example *Borgnat et al.* (2010).)

2.2.2 Noise modelling procedures

In this section, we discuss five approaches to statistically model noise. The first two approaches are used already in seismic noise modelling (for example *O'Brien*, 1974, *Pearce and Barley*, 1977) while the remaining three approaches are novel applications to seismic noise modelling adapted from communication theory (for example *Massart et al.*, 1988, *Scharf*, 1991). Excluding WGN, all acronyms of modelling methods are not common acronyms and are only used by the authors.

WGN: The first noise model is a simple White Gaussian Noise (WGN) model. For the WGN model to be comparable to the recorded noise and the other noise models, the amplitude is scaled to fit the expected range of the recorded noise.

CONV: The second noise model, referred to as the CONVolution-based modelling method (CONV), is similar to work by *Pearce and Barley* (1977) and *Zhong et al.* (2015), where a period of recorded noise ($\boldsymbol{t}$) is convolved ($*$) with a random Gaussian trace ($\boldsymbol{g}$) to create a modelled trace ($\boldsymbol{n}$) with the same frequency content as the original recorded trace:

$$\boldsymbol{n} = \boldsymbol{t} * \boldsymbol{g}, \tag{2.5}$$

(bold font indicates a vector quantity). Following *Pearce and Barley* (1977), noise is modelled on a station-by-station basis with the recorded noise separated into 1 minute time segments. *Zhong et al.* (2015) have used this method to create surrogate noise models as a test for stationarity.

COVA: The third modelling method is based on the statistical COVAriance modelling method (COVA) which assumes that noise can be statistically represented as a multivariate Gaussian random field, defined by only a mean and covariance matrix. A synthetic noise patch is created by drawing a random realization from this multivariate Gaussian distribution as illustrated in the work flow in Figure 2.1. The data is divided into recorded noise patches defined by a spatial group of N_x traces, over a finite time window, N_t, with patch dimensions $[N_t \times N_x]$. For computational purposes, this is reshaped to create a patch column vector, $\boldsymbol{d}$, with dimensions $[N_t N_x \times 1]$. To get a good approximation of the mean and covariance matrix, K realisations of the noise are used (i.e., K patches). The patch vectors are horizontally concatenated to create a data matrix, $\boldsymbol{D}$, with dimensions $[N_t N_x \times K]$:

$$\boldsymbol{D} = [\boldsymbol{d}_1 \ \boldsymbol{d}_2 \ \ldots \ \boldsymbol{d}_{K-1} \ \boldsymbol{d}_K]. \tag{2.6}$$

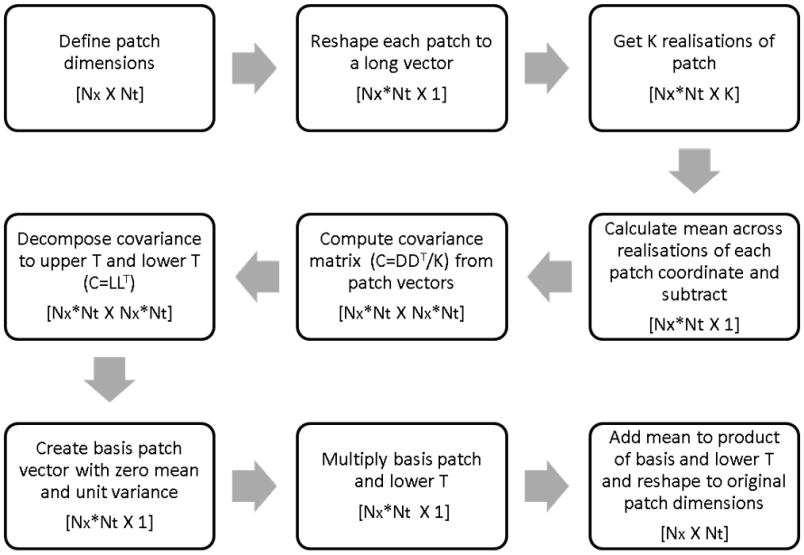

Figure 2.1: *Covariance-based modelling method work flow*

Prior to computing the covariance matrix, the mean, $\boldsymbol{\mu}$, is calculated across the K realisations

$$\boldsymbol{\mu} = \frac{\boldsymbol{D}\mathbf{1}}{K-1}, \tag{2.7}$$

where $\mathbf{1}$ is a unit column vector of length K. The mean is removed from each patch (i.e. $\hat{\boldsymbol{d}} = \boldsymbol{d} - \boldsymbol{\mu}$) and the covariance matrix $\boldsymbol{C}$ is computed using

$$\boldsymbol{C} = \hat{\boldsymbol{D}}\hat{\boldsymbol{D}}^T/K, \tag{2.8}$$

where $\hat{\boldsymbol{D}} = [\hat{\boldsymbol{d}}_1\ \hat{\boldsymbol{d}}_2\ \ldots\ \hat{\boldsymbol{d}}_{K-1}\ \hat{\boldsymbol{d}}_K]$ and $\hat{\boldsymbol{D}}^T$ is the transpose of $\hat{\boldsymbol{D}}$. $\boldsymbol{C}$ is then decomposed into upper and lower triangular matrices through a Cholesky decomposition

$$\boldsymbol{C} = \boldsymbol{C}^{1/2}\boldsymbol{C}^{T/2}. \tag{2.9}$$

The lower triangular matrix $\boldsymbol{C}^{1/2}$ is the square root of the covariance matrix $\boldsymbol{C}$ which is the equivalent of standard deviation for univariate normal distributions. A random vector $\boldsymbol{b}$ of Gaussian white noise with unit variance and zero mean is generated to form the basis of the noise model. To recreate the spatio-temporal correlation observed on the noise patches, $\boldsymbol{d}$, the Gaussian noise vector is multiplied by the lower triangular matrix, $\boldsymbol{C}^{1/2}$, and the product is summed with the mean vector, $\boldsymbol{\mu}$,

$$\tilde{\boldsymbol{d}} = \boldsymbol{C}^{1/2}\boldsymbol{b} + \boldsymbol{\mu}. \tag{2.10}$$

The modelled patch vector $\tilde{\boldsymbol{d}}$ is then reshaped back to the original patch dimensions to produce a modelled noise patch $\tilde{\boldsymbol{D}}$ with the same first and second mathematical moments as a recorded patch $\boldsymbol{d}$. Where the noise field is considered as a single statistical

phenomenon, as opposed to the sum of multiple noise signals, the COVA approach uses time segments of the full-array data to make up the noise realisations.

ICOVA: Alternatively, the noise can be considered as the sum of multiple phenomena that can have their signals isolated and modelled with spatial and temporal patch lengths varying to represent their statistical properties. For each phenomenon (or noise type) we isolate the relevant data and perform a COVA simulation. The final model is generated by summing the results from the different noise types with the final model being referred to as the isolated COVA (ICOVA) model. The ICOVA method requires multiple realisations of each type of noise signal, having the same statistical properties observed across the realisations. To ensure this condition is met a minimum of 200 realisations were used for each identified noise signal model and all realisations were required to have a $> 75\%$ probability of arising from the same distribution. The probability of arising from the same distribution was determined using a Mann-Whitney-White (MWW) test (*Bloomfield*, 2014).

ICOVA-LPF: The final noise modelling method provides an alternative for modelling individual noise signals where they do not arise from a multivariate Gaussian distribution. This method models a single realisation through the use a Linear Prediction Filter (LPF), where the filter coefficients are determined using the autocorrelation method of autoregressive modelling. The LPF method is used on noise signals that were not accurately represented in the ICOVA model and therefore is the sum of noise signals modelled using ICOVA and LPF methods, and is referred to as the ICOVA-LPF model.

2.3 Surface Array Passive Seismic Data

The seismic data analysed in this study comes from the Aquistore carbon dioxide (CO_2) storage site, located in South Saskatchewan, Canada in the northern part of the Williston Basin (*Roach et al.*, 2015). CO_2 is captured at the Boundary Dam power plant to the east of the Aquistore storage site, where some of the CO_2 is transported by pipeline to the site. The CO_2 is injected into a deep saline aquifer at a depth of 3150-3350m to study geological storage of CO_2. Injection started in late April 2015 and the project has injected up to 1000 tonnes per day over an initial injection period of six months.

The permanent passive seismic array consists of 51 buried, vertical component geophones having a cross-shaped geometry as illustrated in Figure 2.2 and has been recording since 25 July 2012. The geophones are 10Hz instruments with a sampling frequency

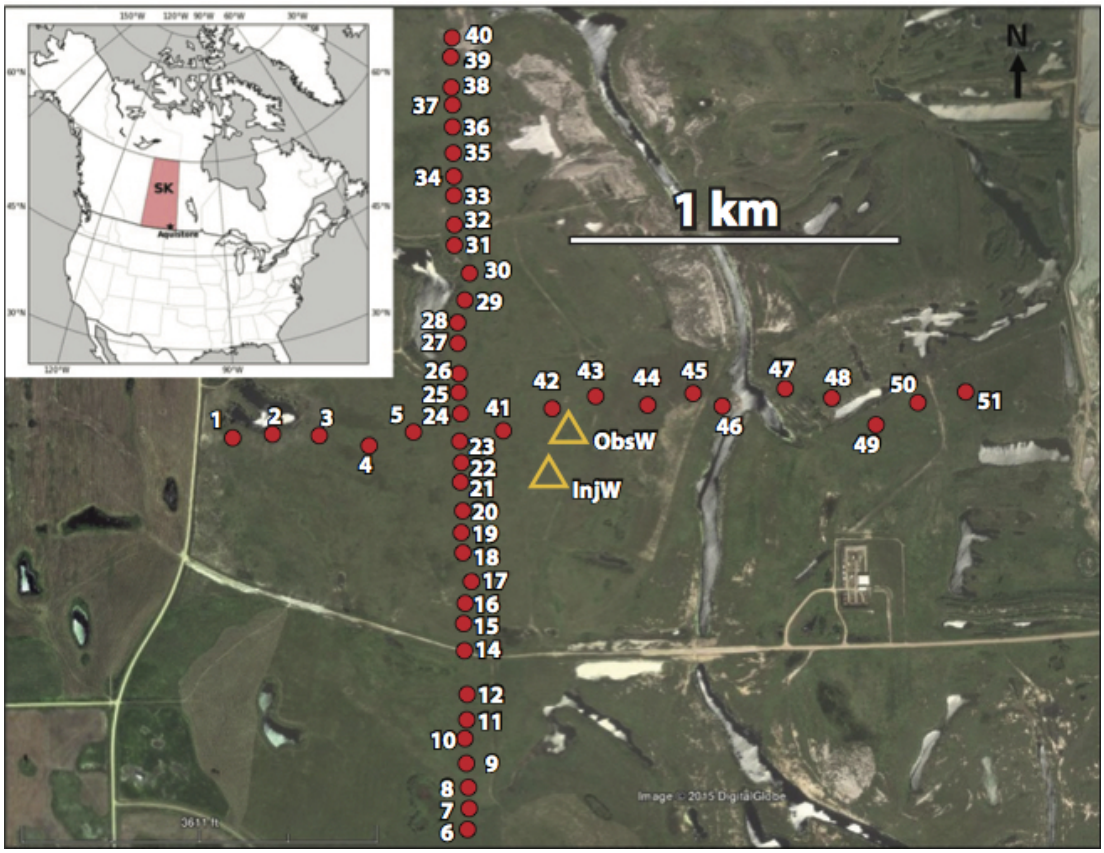

Figure 2.2: *Aquistore permanent seismic array survey geometry. Geophones are denoted by red dots alongside the station number, while the observation and injection wells are illustrated by yellow triangles.*

of 500Hz buried at a depth of 20m. A North-South (N-S) road passes close to station 1 and an East-West (E-W) road passes close to station 14. A vertical injection and a vertical observation well are located near the centre of the geophone array as illustrated by triangles in Figure 2.2. Drilling and construction of the injection well occurred between July and September 2012, and drilling and construction of the observation well occurred between September and December 2012. In this study we analyse a subset of the data from 25 July to 5 October 2012. An example of the recorded data is given in Figure 2.3. Where results are given for a week of data, these are computed from 14 August whilst for results computed for an hour these are computed from the Tuesday between 1p.m. and 2p.m.. These time samples are chosen as they are representative of the full dataset. Since the array has been recording prior to CO_2 injection, the recorded time series represents an excellent dataset on which to study non-injection related noise signals. During injection periods, additional noise signals would be present in the data, however, the techniques proposed in this study could easily be extended to include this type of noise. To preserve the noise signals of interest, no preprocessing was performed on the data.

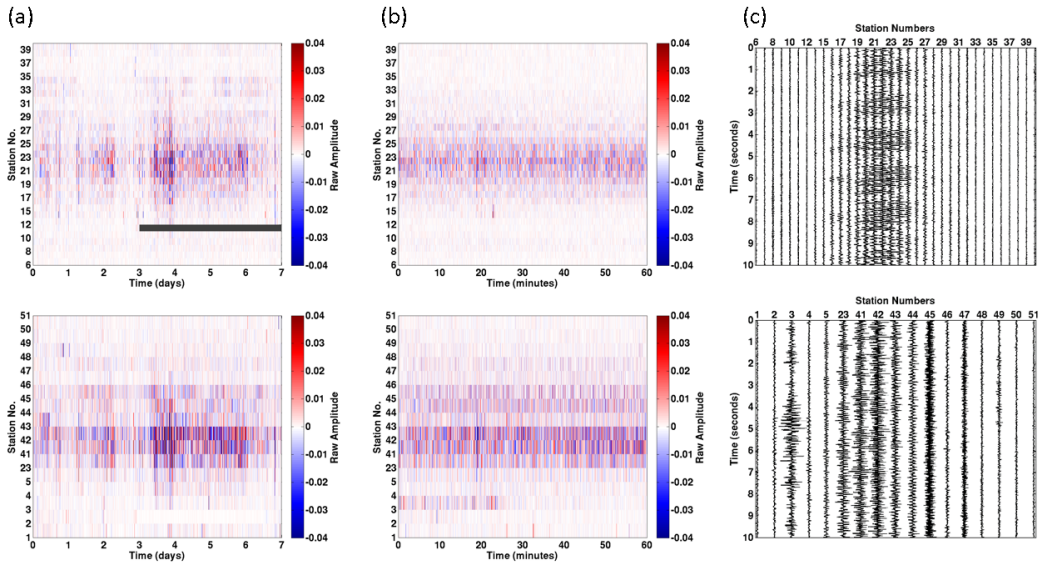

Figure 2.3: *Example of raw data used in the noise analysis for time periods of: (a) a week, (b) an hour and (c) ten seconds. Top row represents geophones on N-S profile and lower row represents geophones on E-W profile. Absent data is portrayed by a grey box.*

2.4 Noise Characterisation

2.4.1 Noise analysis

The stationarity results for a single week are illustrated in Figure 2.4. There is a clear trend of larger magnitude mean and variance values around the centre of the array with an observable decrease in mean and variance away from the array centre. Similar large magnitude mean and variance values are observed at station 1, where the large mean values are observed for shorter periods of time and are not observed during the night-time. It is likely that the increased values observed at the centre of the array are associated with noise originating from the well site and the increased values at station 1 are likely due to noise arising from road traffic.

PSDs and STFTs for three stations across the EW geophone profile are shown in Figure 2.5. Comparison of the three PSDs shows that the power spectrum varies significantly across the array, with station 42 in particular experiencing higher energy content at higher frequencies than stations 1 and 51. Station 51 has a constant power spectra across the hour (as shown in the STFT plots), station 1 experiences several spikes across all frequencies, and station 42 experiences a break in the power spectral trend for about a minute at approximately 46 minutes. Figure 2.6 illustrates the distribution of energy across the array, where higher energy levels are observed around the well

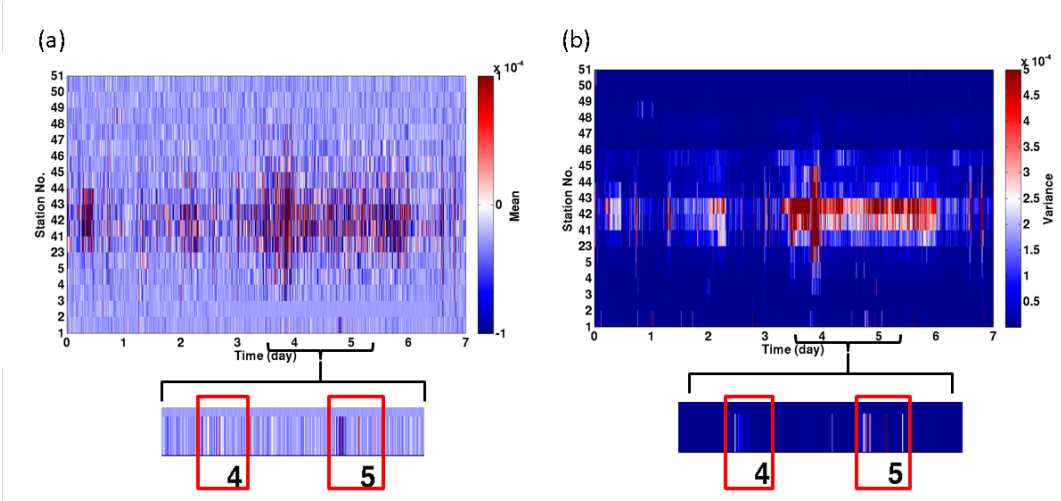

Figure 2.4: *(a) Mean and (b) variance results from sliding window analysis on a week of data from E-W geophone profile. Bottom inserts are zoomed in on roadside station (station 1) with daytime illustrated by the red boxes.*

site. Therefore, not only are the individual power spectrums non-white, but the energy across the array is also not equally distributed.

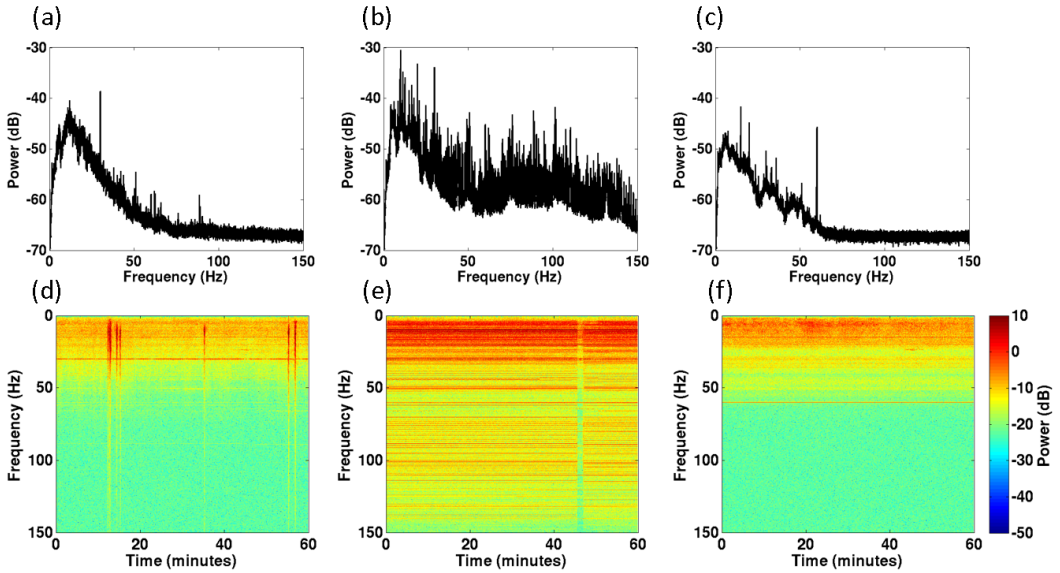

Figure 2.5: *Top row is the power spectral density from one hour of data at (a) station 1, (b) 42 and (c) 51. Lower row represents amplitude spectra calculated from a STFT for the same stations. Prior to converting to dB, each spectrum has been normalised to allow easy comparisons of the shapes of the spectra, this is required due to the uneven distribution of energy across the array as illustrated in Figure 2.6.*

Figure 2.7 illustrates the distribution of raw amplitudes for three 5-seconds windows with varying levels of Gaussianity. Each plot has a Gaussian probability density function overlain on it that has been computed from the mean and variance of the am-

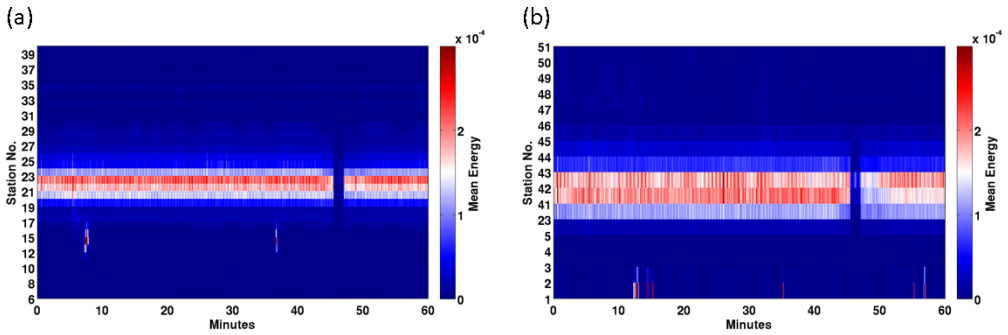

Figure 2.6: *Seismic energy (i.e., amplitude squared) across array for an hour of data from (a) N-S and (b) E-W profiles.*

plitudes observed in the respective windows. Due to the finite sample length of each window, numerically computed skewness and excess kurtosis values for the Gaussian surrogate noise are non-zero (see Table 2.1). However, comparison of the Gaussian surrogate with the recorded Aquistore values shows that the recorded noise variations are significantly higher. Table 2.1 illustrates that the average skewness for the recorded noise is close to zero. Yet, the maximum and minimum values are substantially higher than that of the Gaussian noise. For the excess kurtosis values of the recorded noise the mean is noticeably less than zero and over 70% of the values are less than zero. For the Gaussian surrogates there are no values for either skewness or kurtosis that have a magnitude greater than 1. For the recorded noise 4% of excess kurtosis values have a magnitude greater than one, demonstrating that values of kurtosis have a higher variability in the recorded noise than the Gaussian surrogates. Despite the higher variations in both skewness and excess kurtosis values for the recorded noise, the spatial and temporal trends are much less clear than those observed for the mean and variance in the stationarity analysis, as shown in Figure 2.8.

Table 2.1: *Calculated skewness and excess kurtosis values for an hour of recorded Aquistore data and Gaussian surrogate values.*

	Skewness		**Excess kurtosis**	
	Aquistore	*Gaussian*	*Aquistore*	*Gaussian*
Mean	-0.002	0.000	-0.109	-0.002
Maximum	49.98	0.27	2496.00	0.80
Minimum	-19.58	-0.26	-1.65	-0.41
% >0	49.71	50.00	26.45	47.15
% <0	50.29	50.00	73.55	52.85
% >1	0.01	0.00	2.68	0.00
% <-1	0.04	0.00	2.71	0.00

Figure 2.8 shows the bicoherence and tricoherence values for the recorded noise and the Gaussian surrogate noise (Figure 2.8e,f and 2.8g, h respectively). While the background

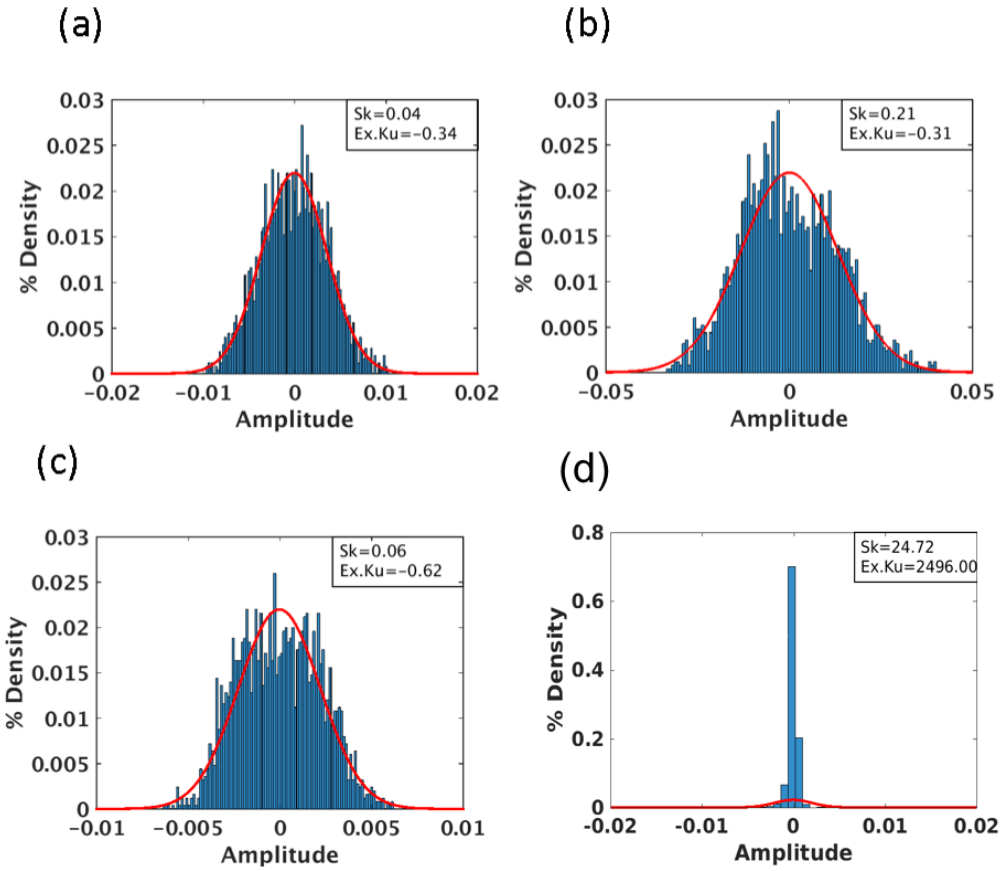

Figure 2.7: *Examples of three amplitude distributions and their skewness and excess kurtosis values for five seconds of data recorded from (a) station 45 at about 2 minutes (background noise), (b) station 42 at about 30 minutes (wellsite noise), (c) station 12 at about 12 minutes (traffic noise), and, (d) station 2 at about 15 minutes. Overlain on each histogram is their respective Gaussian distribution. As all histograms have the same number of bins, note the different y-axis scale required for (d) to account for the leptokurtic nature of the distribution.*

trends for the bicoherence and tricoherence analyses are reasonably similar in magnitude to the Gaussian surrogate noise values, there is an observable spatio-temporal structure to the values. The areas of strongest non-Gaussianity are at stations 1 and 2 for times between 13 and 16 minutes, at 35 minutes and between 56 and 58 minutes. At these points both the bicoherence and tricoherence values of the recorded noise are double that of the Gaussian surrogate noise. Other areas of significant non-Gaussianity occur for stations around the well site (i.e., stations 23 to 45), which have on average 20% higher bicoherence and tricoherence magnitudes than the reference Gaussian values. Station 41 appears to display the least Gaussianity with respect to both bicoherence and tricoherence. As well, there are 2 minutes of increased non-Gaussianity

between 46 to 47 minutes across stations 23 to 45. As with the method of statistical moments, the variations of kurtosis are greater than skewness.

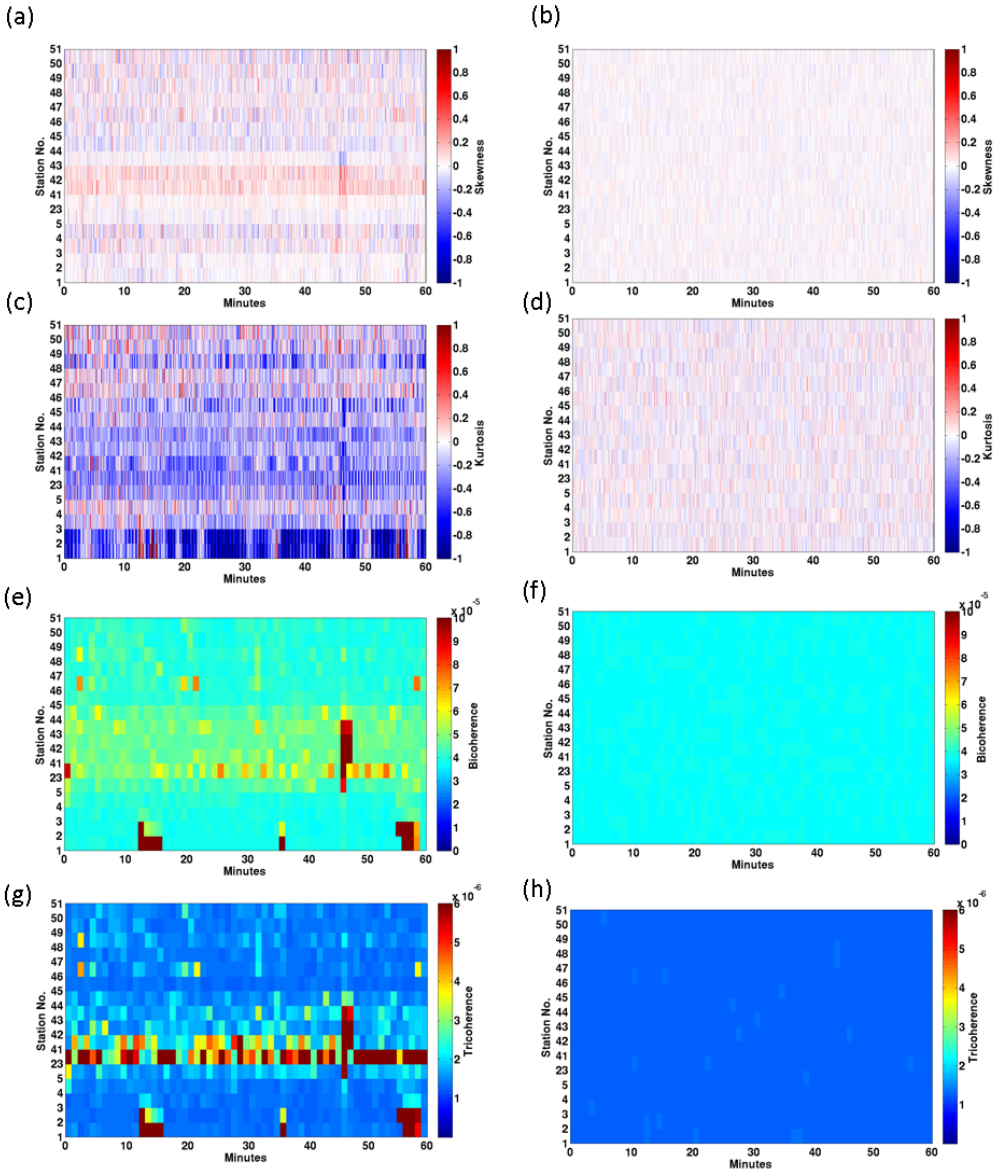

Figure 2.8: *(a),(b) Skewness for Aquistore and Gaussian surrogate noise respectively and (c),(d) kurtosis for Aquistore and Gaussian surrogate noise respectively, all calculated from sliding window analysis. (e),(f) Bicoherence for Aquistore and surrogate Gaussian noise respectively, and (g),(h) tricoherence for Aquistore and surrogate Gaussian noise respectively of an hour of data.*

2.4.2 Noise classification

Next we consider what noise sources may be present in the data and identify three separate noise signals, as illustrated in Figure 2.9. The first signal (Figure 2.9a,d) is a constant 60 Hz signal recorded at station 51 to the far east of the array and is believed to be due to electrical interference between power cables and the recording instruments. The second identified signal (Figure 2.9b,e) is observed on stations adjacent to the

roadside (stations 1 and 14), where the signal is characterised by a burst of energy that lasts about one minute with peak energy around the middle of the signal duration. The signal consistently appears as a broad-band burst and the wavelet shape in time is highly variable. In some instances the noise can be observed on neighbouring stations. The final identified noise signal (Figure 2.9c,f) is characterised by a strong frequency banding with intermittent pauses. The signal is centred around the well site, yet is observable on stations up to 500 metres away with associated attenuation of higher frequency bands.

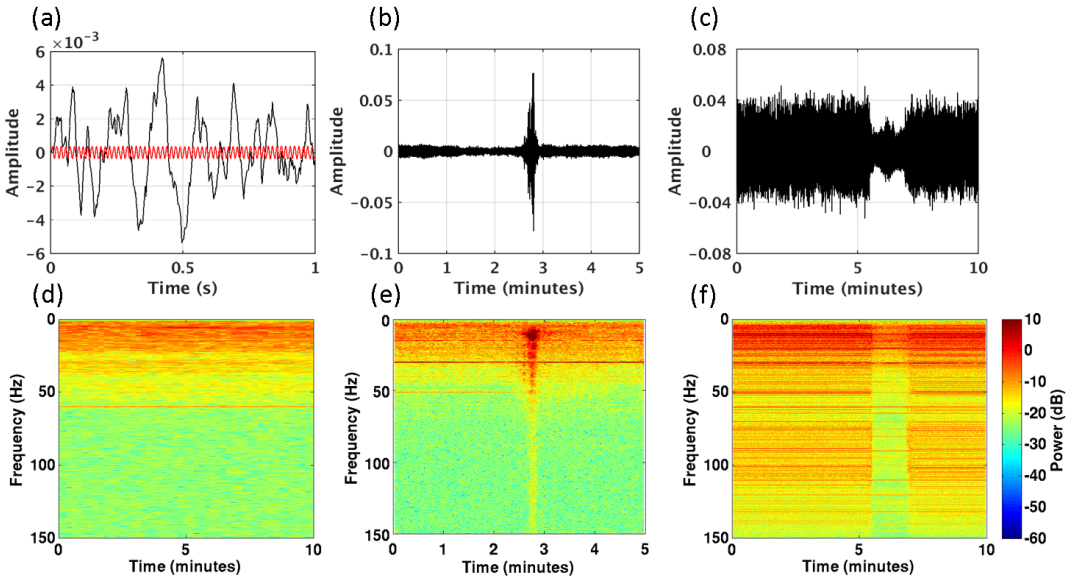

Figure 2.9: *Individual noise signals, (a),(d) stationary electrical interference observed at station 51 with red-trace denoting 60Hz band passed trace, (b),(e) non-stationary traffic signal observed at station one, and (c),(f) pseudo-non-stationary well site noise observed at station 42. Top row shows signals in time domain while portrays signals in the frequency domain.*

The presence of at least three broadly different noise signals across the array leads us to postulate that instead of considering the noise field as a single statistical phenomenon, it is more realistic to consider it as the sum of multiple phenomena, each with their own spatial, temporal, frequency and statistical distribution properties as illustrated in the following equation:

$$n(x,t) = a(x,t) + b(x,t) + c(x,t) + \ldots, \tag{2.11}$$

where x is the spatial coordinate, t is time, n is the full noise field, and a, b, c, $\ldots$ are individual noise sources. Similar to the work of *Priestley* (1988), we propose that, for modelling purposes, noise is split into the following three classifications dependent on their temporal properties with respect to a specified event detection window (EDW):

1. *Stationary noise*: a constant signal over the EDW, such as that observed at

station 51,

2. *Non-stationary noise*: a signal that does not last for a significant period with respect to the EDW, such as that observed at station 1, and
3. *Pseudo-non-stationary noise*: a constant signal for a significant period with respect to the EDW, yet is not constant over the full EDW, such as that observed at station 41.

In this study the EDW is one hour.

2.5 Noise Modelling Results

Shown in Figure 2.10 are the noise modelling results and the recorded noise on which they were based. For the CONV modelling, the hour of recorded noise is split into one minute time windows and modelled. These models are then concatenated to represent the temporal location of the recorded noise window from which they have been computed. The COVA method uses a spatial patch length (N_x) of 50, a temporal patch length (N_t) of one second and 3600 realisations (K) while these parameters vary across individual models in the ICOVA modelling method. For COVA and ICOVA modelling the modelled time lengths are shorter than the recorded noise, therefore a Monte-Carlo simulation is performed to create multiple models from Gaussian basis vectors that are concatenated to create the full time window. Figure 2.11 displays the modelled noise signals (identified in Figure 2.9) for the first three noise models (WGN, CONV and COVA) in the time domain and is based on considering the noise field as a whole. Figure 2.12 is the frequency domain representation of the modelled noise signals shown in Figure 2.11.

Due to the WGN model being independent of the recorded noise, it is not surprising that this model has little visual similarity with the recorded data. The CONV model shows a good visual correlation in the time domain (Figure 2.10(c)). However, when analysing the power spectrum for the individual noise signals (i.e., in Figure 2.9), it is clear that the CONV model fails to characterise the traffic noise (Figure 2.11(e) and 2.12(e)). This is expected as this method requires noise to be stationary over the modelling time window and this is not the case for traffic noise. The COVA model also fails to accurately represent traffic noise (Figure 2.11(h) and 2.12(h)) due to the modelling requirement that patches must have the same statistical properties. The presence of traffic noise in a handful of patches has resulted in the inclusion of traffic noise in the covariance matrix and therefore also into every modelled noise patch. This is also the case for well-site noise, where the pause at around 46 minutes is not observed in the COVA model (Figure 2.11(i) and 2.12(i)).

Figure 2.10(e) shows the result of ICOVA modelling, where noise signals have been

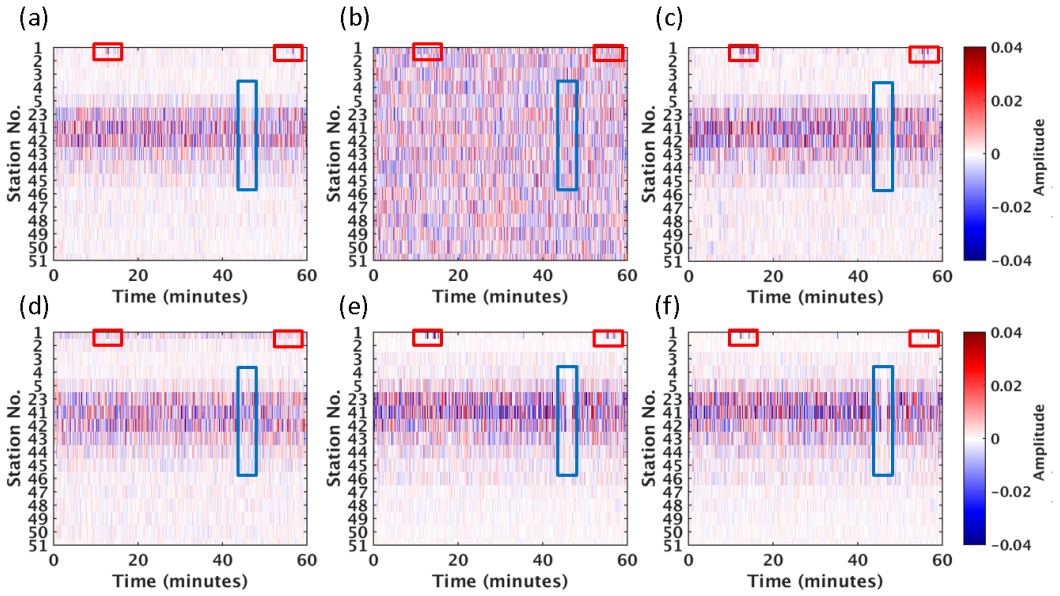

Figure 2.10: *(a) Hour of noise data from E-W profile used for modelling, where the red boxes indicate non-stationary traffic events at station 1 and the blue boxes indicate a pause in well site noise across the middle of the array. (b) WGN model, (c) CONV noise model, (d) single COVA noise field model, (e) sum of multiple COVA noise signal models, and (f) the combination of LPF and ICOVA noise models.*

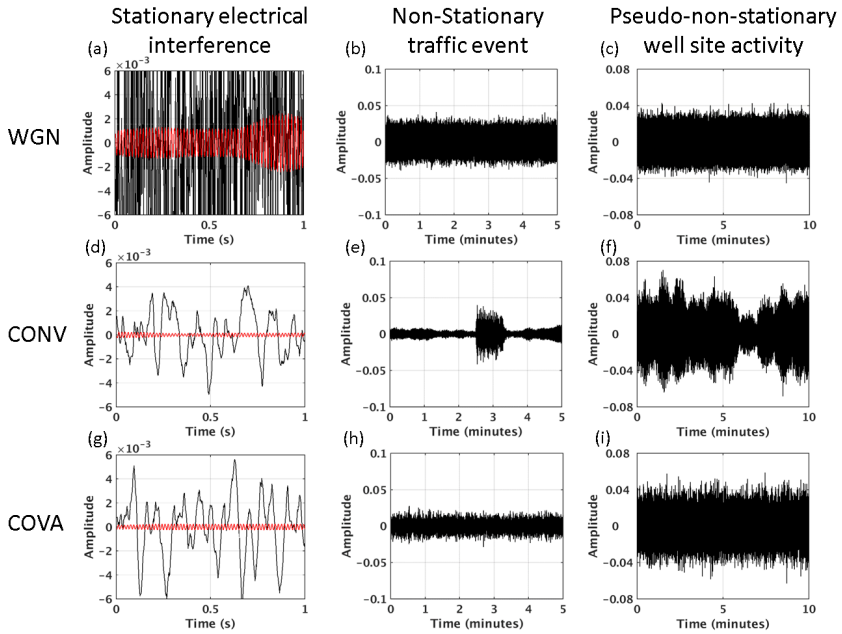

Figure 2.11: *Individual noise signals traces of stationary electrical interference (a,d,g), non-stationary traffic noise (b,e,h) and pseudo-non-stationary well site noise (c,f,i). The top row has traces from WGN model, the middle row has traces from the CONV model and the bottom row has traces from the COVA model. The red traces on the first column denote a 60Hz bandpassed trace.*

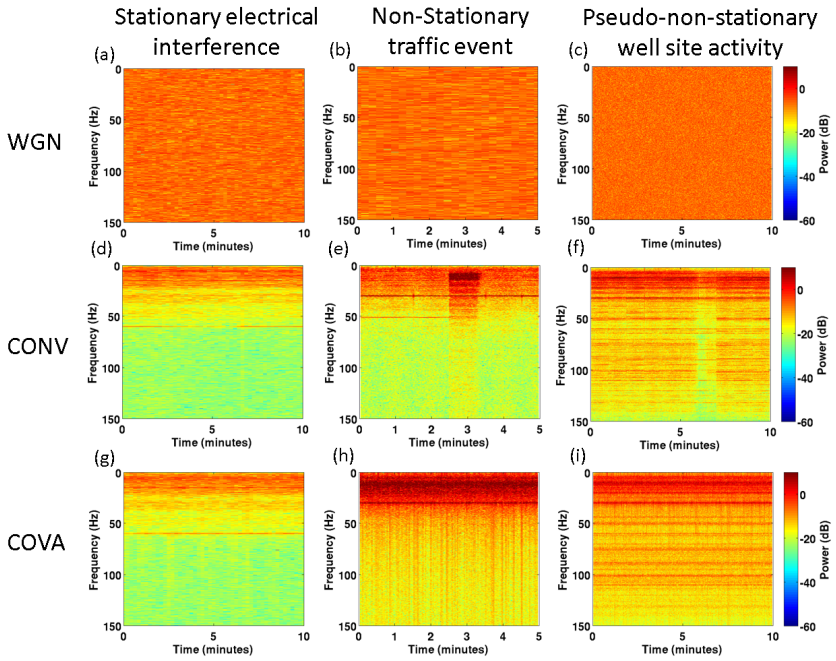

Figure 2.12: *Individual noise signals amplitude spectrum's of stationary electrical interference (a,d,g), non-stationary traffic noise (b,e,h) and pseudo-non-stationary well site noise (c,f,i). The top row has spectra from WGN model, the middle row has spectra from the CONV model and the bottom row has spectra from the COVA model.*

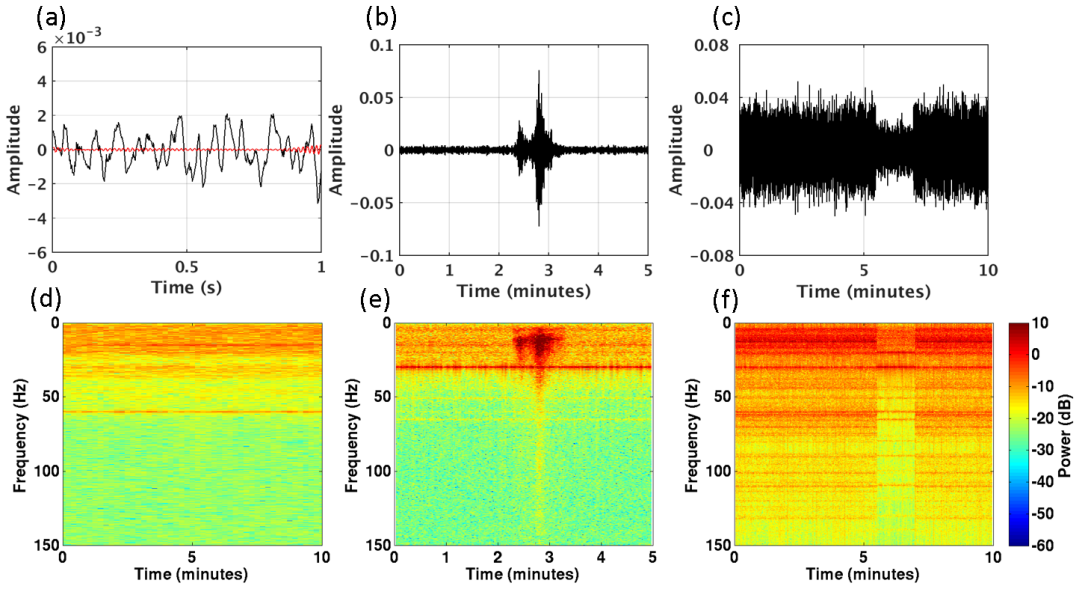

Figure 2.13: *Individual noise signals modelled by a sum of COVA models, (a),(d) stationary electrical interference observed at station 51 with red-trace denoting 60Hz band passed trace, (b),(e) non-stationary traffic signal observed at station 1, and (c),(f) pseudo-non-stationary well site noise observed at station 42. Top row shows signals in time domain while the second row portrays signals in the frequency domain.*

isolated and modelled individually. Traffic noise events and the pause in well site noise reflect the times that they occur in the recorded noise. Similar to Figure 2.9, the individual modelled noise signals are shown in Figure 2.13. The 60 Hz band-passed trace is of constant amplitude in time yet it is of lower magnitude in comparison to the recorded 60 Hz noise. In the frequency domain, the modelling has resulted in a smearing of the 60 Hz noise across nearby frequencies. The smearing of frequencies is observed on all noise signal models, particularly on the well site noise which experiences strong frequency banding. The car signal model provides a good approximation although the duration of the event is of slightly different shape and lasts longer than in the identified traffic noise (Figure 2.9(b)).

To provide a quantitative measure of how accurately the ICOVA models represent the original noise model realisations, MWW tests were performed to give a probability of the likelihood that the two datasets originate from the same distribution. For each noise signal model the MWW tests were performed between recorded noise and the modelled noise, over the modelling realisation parameters, with the results shown in Table 2.2. All the noise models have over 65% of MWW results with a greater than 50% probability of arising from the same distribution. The well site noise has the greatest likelihood of models and patches arising from the same distribution with only 4% of MWW results having a probability of less than 25%. All models have less than 12% of realisations with a low chance ($P < 25\%$) of arising from the same distribution

Table 2.2: *Percent of patch to model realisations likely to arise from the same distributions based on MWW tests*

Noise Signal Models	Percent of realisations with $P > 75\%$	Percent of realisations with $75\% > P > 50\%$	Percent of realisations with $50\% > P > 25\%$	Percent of realisations with $P < 25\%$
Background	34.5	30.6	23.3	11.7
Well site	41.9	34.2	19.2	4.4
Traffic	36.4	30.1	22.5	10.4

therefore the models provide a reasonable representation of the statistics of the recorded noise signals.

Figure 2.10(f) illustrates the result of the ICOVA-LPF model, where the LPF method has been used to gain a more realistic representation of the traffic event. The stationary background noise and pseudo-non-stationary well noise were modelling using the ICOVA method while the traffic noise, shown in Figure 2.14, is modelled using the ICOVA-LPF method. Modelling traffic events using an ICOVA-LPF provides a closer representation of the recorded noise signal and results in less frequency smearing, as is observable at 60Hz on Figure 2.14. However, the full hour of recorded noise for modelling has seven different traffic events and to fully represent the variability of traffic

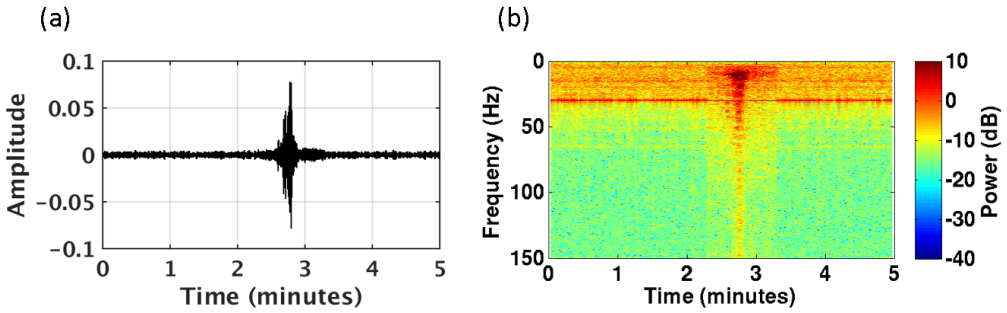

Figure 2.14: *A single traffic event, in time (a) and frequency (b), modelled using the auto-correlation method of AR modelling with background noise added from COVA noise model.*

noise then each event must be modelled individually.

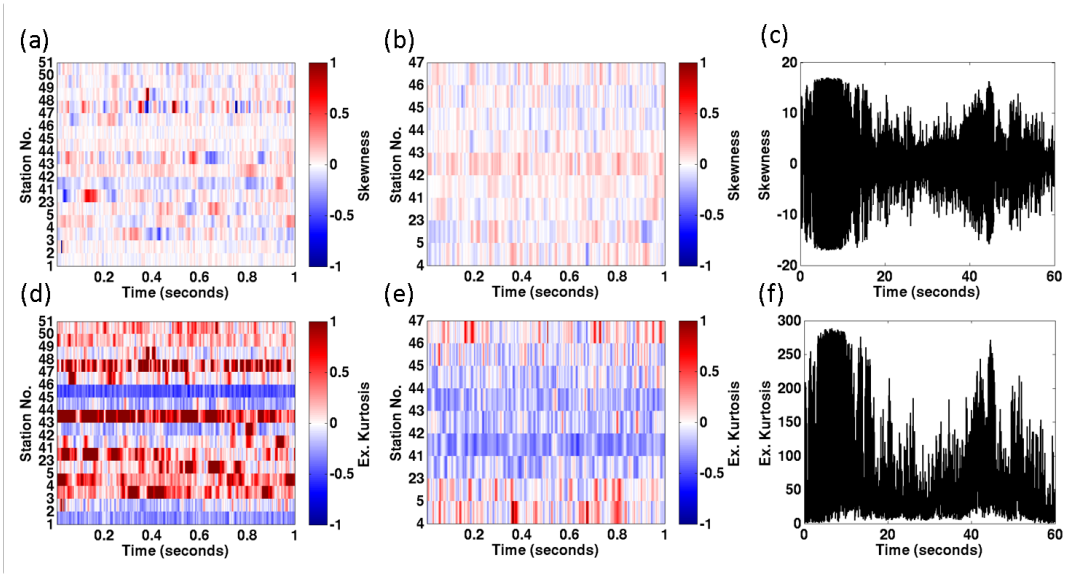

Figure 2.15: *Skewness (top row) and kurtosis (bottom row) of patch index points for (a) ICOVA stationary background noise model, (b) ICOVA pseudo-non-stationary well site noise model, and (c) ICOVA non-stationary traffic noise model.*

Figure 2.15 shows the skewness and excess kurtosis calculated across the realisations for each spatio-temporal patch position. As seen in the initial Gaussianity analysis, kurtosis is the dominant property for identifying non-Gaussianity. The well site noise realisations are the nearest to a multivariate Gaussian distribution and this may explain their higher MWW results while the traffic noise is highly non-Gaussian. To provide a constraint on the minimum number of patches required to get a stable estimation of the sample mean, Figure 2.16 shows the convergence of the sample mean for increasing number of patches for each noise type. It can be seen that for all noise types more than 200 realisations are required to get a near-convergence of the sample mean. Beyond 200, the change in mean through the addition of patches still fluctuates however they are of a significantly lower amplitude and so are considered negligible.

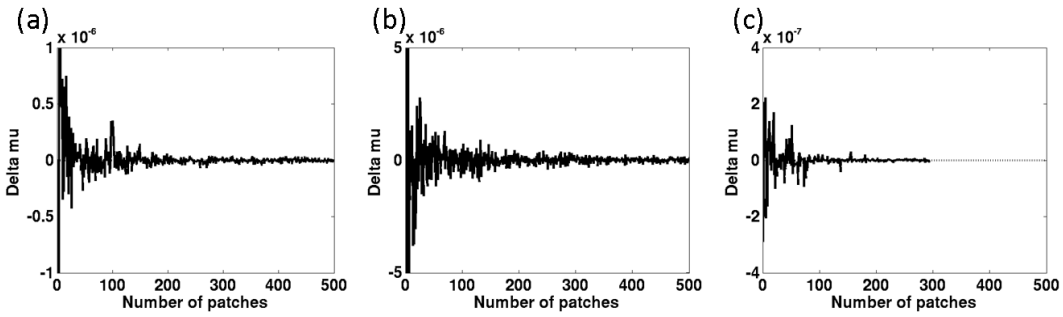

Figure 2.16: *Sample mean convergence over increasing number of noise patches for (a) ICOVA stationary background noise model, (b) ICOVA pseudo-non-stationary well site noise model, and (c) ICOVA non-stationary traffic noise model.*

2.6 Discussion

Based on the noise analysis, it is evident that the spatial and temporal trends observed in the passive seismic data contradict the assumption of stationary, white and Gaussian noise. For example, Figure 2.4 shows considerable changes in the variance throughout the data. The figure also shows variance of the sample mean which we believe could come from one of two sources. Firstly, the variation maybe an artefact of long-period drift of the sensor system. The second possibility is that these variations are the imprint of changes in the variability of trace amplitudes on the measurement of the sample means.

With respect to the Gaussianity of the full noise field, the method of statistical moments did not detect any spatio-temporal trends in the recorded noise field. The excess kurtosis results displayed a significantly higher variation than the skewness results implying that the fourth mathematical moment is likely to be the most effective property for identifying non-Gaussianity of the noise distribution. While both the bicoherence and tricoherence analyses highlight the same spatial and temporal zones as being non-Gaussian (i.e., around the well site and the roadside stations), the amplification of the non-Gaussianity of these aspects observed on the tricoherence analysis complements the observation that kurtosis is the dominant non-Gaussian property of the noise. Based on the study by *Groos and Ritter* (2009), the negative excess kurtosis observed is likely to be due to dominating periodic signals from anthropogenic seismic sources such as generators.

The ICOVA modelling method assumes that the noise field conforms to a multivariate Gaussian distribution as opposed to the single Gaussian distribution assumed in WGN modelling. In other words, under the WGN model the amplitude of noise behaves independently of space and time, whereas this is not the case for the COVA and ICOVA model. This allows each index point on a single recorded patch to have a separate

mean and variance value (i.e., each index point can originate from a different Gaussian distribution). This condition requires that each index point across the patch realisations must arise from the same Gaussian distribution.

A significant benefit of modelling realistic noise, as opposed to directly incorporating recorded noise, is the ability to build a noise database of individual noise signals' covariance matrix and mean vector. A database containing the necessary parameters for modelling a number of different noise signals provides the opportunity for creating 'bespoke' noise models without any data collection or analysis required. This would provide flexibility around the occurrence of noise signals that is not possible when using recorded noise. The automation of noise signal identification and modelling which will significantly reduce manual labour time. From this study, there is the possibility for the incorporation of realistic noise into synthetic seismic datasets to test the robustness of detection and imaging algorithms against the different noise signals and magnitude. Furthermore, the identification of these noise signals and characteristics within the recorded data provides the possibility that the statistical properties of noise can be exploited for noise removal purposes.

2.7 Conclusions

This paper has introduced a novel method for improved realism of modelling noise observed in seismic data. The noise analysis determined that the noise field is not white or stationary and does not conform to a single Gaussian distribution, contrary to conventional assumptions in noise modelling techniques. We have shown that noise is made up of multiple signals that should be modelled separately to maintain their individual properties. We propose doing this using the isolated covariance modelling method, where the noise is assumed to arise from a multi-variate Gaussian distribution. Linear prediction filter modelling was demonstrated as an alternative modelling technique when the assumptions for isolated covariance modelling are not met. We have developed a workflow to incorporate realistic noise models within synthetic seismic datasets. In the future this will provide a more robust opportunity to test and analyse how detection and imaging algorithms respond under realistic noise conditions. Furthermore, the developed workflow can be used to classify individual noise signals and their properties (for example, 2.9) which could possibly be used to guide noise removal techniques. This is becoming increasingly important given recent interest in stochastic interferometric methods for passive seismic data that are based on the assumption that noise (i.e., sources) have random distribution and amplitude characteristics (i.e., not coherent) (*Schuster*, 2009).

Acknowledgements

The authors would like to thank Ray Chambers, Frans Kets and Lisa Roach for valuable discussions during this study. We would like to thank the Petroleum Technology Research Centre (PTRC) for access to Aquistore Data. Aquistore an independent research and monitoring project managed by the PTRC which intends to demonstrate that storing liquid carbon dioxide deep underground (in a brine and sandstone water formation), is a safe, workable solution to reduce greenhouse gases. C. Birnie is funded by the NERC Open CASE studentship NE/L009226/1 and Pinnacle-Halliburton. D. Angus acknowledges the Research Council UK (EP/K035878/1; EP/K021869/1; NE/L000423/1) for financial support.

References

Asten, M., and J. Henstridge (1984), Array estimators and the use of microseisms for reconnaissance of sedimentary basins, *Geophysics*, *49*(11), 1828–1837. 2.1

Asten, M. W. (1978), Geological control on the three-component spectra of rayleigh-wave microseisms, *Bulletin of the Seismological Society of America*, *68*(6), 1623–1636. 2.1

Barajas-Olalde, C., and A. Jeffreys (2014), Seismic wind noise experiments using a portable wind tunnel, in *76th EAGE Conference and Exhibition 2014*. 2.1

Bardainne, T., E. Gaucher, F. Cerda, D. Drapeau, et al. (2009), Comparison of picking-based and waveform-based location methods of microseismic events: Application to a fracturing job, in *2009 SEG Annual Meeting*, Society of Exploration Geophysicists. 2.1

Bartelt, H., A. W. Lohmann, and B. Wirnitzer (1984), Phase and amplitude recovery from bispectra, *Applied Optics*, *23*(18), 3121–3129. 2.2.1

Bekara, M., L. Knockaert, A. Seghouane, and G. Fleury (2003), Seismic signal denoising using model selection, in *Signal Processing and Information Technology, 2003. ISSPIT 2003. Proceedings of the 3rd IEEE International Symposium on*, IEEE. 2.1

Belayouni, N., A. Gesret, G. Daniel, and M. Noble (2015), Microseismic event location using the first and reflected arrivals, *GEOPHYSICS*, *80*, WC133–WC143. 2.1

Berkhout, G., and G. Blacquière (2015), From removing to using ghost reflections, in *SEG Technical Program Expanded Abstracts 2015*. 2.1

Berkner, K., and R. O. Wells Jr (1998), Wavelet transforms and denoising algorithms, in *Signals, Systems & Computers, 1998. Conference Record of the Thirty-Second Asilomar Conference on*, vol. 2, pp. 1639–1643, IEEE. 2.1

Bloomfield, V. A. (2014), *Using R for Numerical Analysis in Science and Engineering*, CRC Press. 2.2.2

Bonnefoy-Claudet, S., F. Cotton, and P.-Y. Bard (2006), The nature of noise wavefield and its applications for site effects studies: a literature review, *Earth-Science Reviews*, *79*(3), 205–227. 2.1

Borgnat, P., P. Flandrin, P. Honeine, C. Richard, and J. Xiao (2010), Testing stationarity with surrogates: A time-frequency approach, *Signal Processing, IEEE Transactions on*, *58*(7), 3459–3470. 2.1, 2.2.1

Chambers, K., J. Kendall, S. Brandsberg-Dahl, J. Rueda, et al. (2010), Testing the ability of surface arrays to monitor microseismic activity, *Geophysical Prospecting*, *58*(5), 821–830. 2.1

Chandran, V., S. Elgar, and B. Vanhoff (1994), Statistics of tricoherence, *Signal Processing, IEEE Transactions on*, *42*(12), 3430–3440. 2.2.1

Collis, W., P. White, and J. Hammond (1998), Higher-order spectra: the bispectrum and trispectrum, *Mechanical systems and signal processing*, *12*(3), 375–394. 2.2.1

Dean, T., J. C. Dupuis, and R. Hassan (2015), The coherency of ambient seismic noise recorded during land surveys and the resulting implications for the effectiveness of geophone arrays, *Geophysics*, *80*(3), P1–P10. 2.1

Draganov, D., K. Wapenaar, and J. Thorbecke (2004), Passive seismic imaging in the presence of white noise sources, *The Leading Edge*, *23*, 889892. 2.1

Drew, J., P. Primiero, K. Brook, D. Raymer, T. Probert, A. Kim, and D. Leslie (2012), Microseismic monitoring field test using surface, shallow grid and downhole arrays, in *SEG Expanded Abstracts*, vol. 31. 2.1

Fisher, R. A. (1930), Moments and product moments of sampling distributions, *Proceedings of the London Mathematical Society*, pp. 199–238. 2.2.1

Forghani-Arani, F. (2013), Analysis and suppression of passive noise in surface microseismic data, Ph.D. thesis, Colorado School of Mines. 2.1

Forghani-Arani, F., M. Batzle, J. Behura, M. Willis, S. S. Haines, and M. Davidson (2012), Noise suppression in surface microseismic data, *The Leading Edge*, *31*(1496–1501), 1496–1501. 2.1

Green, P. J., E. J. Kelly, and M. Levin (1966), A comparison of seismic array processing methods, *Geophysical Journal of the Royal Astronomical Society*, *11*, 6784. 2.1

Grion, S., R. Telling, and J. Barnes (2015), Adaptive de-ghosting by kurtosis maximisation, in *77th EAGE Conference and Exhibition 2015*. 2.1

Groos, J., and J. Ritter (2009), Time domain classification and quantification of seismic noise in an urban environment, *Geophysical Journal International*, *179*(2), 1213–1231. 2.1, 2.6

Gutenberg, B. (1958), Microseisms, *Advances in Geophysics*, *5*, 53–92. 2.1

Kahrizi, A., M. Emdadi, and H. Karslı (2014), Efficiency of complex trace analysis to attenuate ground-roll noise from seismic data, *Journal of Applied Geophysics*, *106*, 50–59. 2.1

Li, Y.-G., K. Aki, D. Adams, A. Hasemi, and W. H. Lee (1994), Seismic guided waves trapped in the fault zone of the landers, california, earthquake of 1992, *Journal of Geophysical Research: Solid Earth (1978–2012)*, *99*(B6), 11,705–11,722. 2.1

Lunedei, E., and D. Albarello (2015), Horizontal-to-vertical spectral ratios from a full-wavefield model of ambient vibrations generated by a distribution of spatially correlated surface sources, *Geophysical Journal International*, *201*(2), 1142–1155. 2.1

Massart, D. L., B. Vandeginste, S. Deming, Y. Michotte, and L. Kaufman (1988), *Chemometrics: a textbook*, Elsevier Amsterdam. 2.2.2

Maxwell, S. (2014), *Microseismic Imaging of Hydraulic Fracturing: Improved Engineering of Unconventional Shale Reservoirs*, 17, SEG Books. 2.1

Nørmark, E. (2011), Wind and rain induced noise on reflection seismic data, in *Near Surface 2011-the 17th European Meeting of Environmental and Engineering Geophysics*. 2.1

O'Brien, P. (1974), Aspects of seismic research in the oil industry, *Geoexploration*, *12*(2), 75–96. 2.2.2

Pearce, R., and B. Barley (1977), The effect of noise on seismograms, *Geophysical Journal International*, *48*(3), 543–547. 2.1, 2.2.2, 2.2.2, 2.2.2

Pflug, L. A. (2000), Principal domains of the trispectrum, signal bandwidth, and implications for deconvolution, *Geophysics*, *65*(3), 958–969. 2.2.1

Pierce, R. D. (1997), Application of the positive alpha-stable distribution, in *Higher-Order Statistics, 1997., Proceedings of the IEEE Signal Processing Workshop on*, pp. 420–424, IEEE. 2.1

Price, D., D. Angus, K. Chambers, and G. Jones (2015), Surface microseismic imaging in the presence of high-velocity lithological layers, *Geophysics*, *80*, WC117–WC131. 2.1

Priestley, M. B. (1988), *Non-linear and non-stationary time series analysis*, Academic Press London. 2.4.2

Riahi, N., and P. Gerstoft (2015), The seismic traffic footprint: Tracking trains, aircraft, and cars seismically, *Geophysical Research Letters*, *42*(8), 2674–2681. 2.1

Riahi, N., A. Goertz, B. Birkelo, and E. H. Saenger (2013), A statistical strategy for ambient seismic wavefield analysis: investigating correlations to a hydrocarbon reservoir, *Geophysical Journal International*, *192*(1), 148–162. 2.1

Roach, L. A., D. J. White, and B. Roberts (2015), Assessment of 4d seismic repeatability and co2 detection limits using a sparse permanent land array at the aquistore co2 storage site, *Geophysics*, *80*(2). 2.3

Scharf, L. L. (1991), *Statistical signal processing*, vol. 98, Addison-Wesley Reading, MA. 2.2.2

Schilke, S., T. Probert, I. Bradford, A. Özbek, and J. Robertsson (2014), Use of surface seismic patches for hydraulic fracture monitoring, in *76th EAGE Conference and Exhibition 2014*. 2.1

Schuster, G. T. (2009), *Seismic interferometry*, vol. 1, Cambridge University Press Cambridge. 2.7

Shao, J., J. Tang, C. Sun, D. Wu, and N. Li (2015), Micro-seismic data denoising based on sparse representations over learned dictionaries, in *77th EAGE Conference and Exhibition 2015*. 2.1

Sylvette, B.-C., C. Cécile, B. Pierre-Yves, C. Fabrice, M. Peter, K. Jozef, and D. Fäh (2006), H/v ratio: a tool for site effects evaluation. results from 1-d noise simulations, *Geophysical Journal International*, *167*(2), 827–837. 2.1

Trifu, C., D. Angus, and V. Shumila (2000), A fast evaluation of the seismic moment tensor for induced seismicity, *Bulletin of the Seismological Society of America*, *90*(6), 1521–1527. 2.1

Trojanowski, J., and L. Eisner (2015), Comparison of migration-based detection and location methods for microseismic events, in *77th EAGE Conference and Exhibition 2015*. 2.1

Walden, A. T., and M. L. Williams (1993), Deconvolution, bandwidth, and the trispectrum, *Journal of the American Statistical Association*, *88*(424), 1323–1329. 2.2.1

White, R. E. (1984), Signal and noise estimation from seismic reflection data using spectral coherence methods, *Proceedings of the IEEE*, *72*(10), 1340–1356. 2.1

Zhong, T., Y. Li, N. Wu, P. Nie, and B. Yang (2015), A study on the stationarity and gaussianity of the background noise in land-seismic prospecting, *Geophysics*, *80*(4), V67–V82. 2.1, 2.2.2, 2.2.2

Chapter 3

On the importance of benchmarking algorithms under realistic noise conditions

Claire Birnie[1], Kit Chambers [2], Doug Angus [1,a], and Anna L. Stork [3]

[1] *School of Earth and Environment, University of Leeds, United Kingdom*
[2] *Nanometrics Inc., United Kingdom*
[3] *School of Earth Sciences, University of Bristol, UK*
[a] *now at ESG Solutions, Canada*

This chapter is an adaptation of the paper:
Birnie, C., Chambers, K., Angus, D, and Stork, A., *under review*, Effect of noise on microseismic event detection and imaging procedures using ICOVA statistical noise modelling method. *Journal of Applied Geophysics*

The following adaptations have been made to the submitted version:

1. Figure 3.1 has been edited and enlarged to allow easier identification of receivers and wells,
2. A new discussion has been added on double-couple, volumetric and explosive components of moment tensor (including Figure 3.13), and
3. further justification has been provided on the use of automated trigger detection (STA/LTA) considered in this study.

Abstract

Testing with synthetic datasets is a vital stage in an algorithm's development for benchmarking the algorithm's performance. A common addition to synthetic datasets is White, Gaussian Noise (WGN) which is used to mimic noise that would be present in recorded datasets. The first section of this paper focusses on comparing the effects of WGN and realistic modelled noise on standard microseismic event detection and imaging algorithms using synthetic datasets with recorded noise as a benchmark. The datasets with WGN under-perform on the trace-by-trace algorithm whilst over-performing on algorithms utilising the full array. Throughout, the datasets with realistic modelled noise perform near identically to the recorded noise datasets. The study concludes by testing an algorithm which simultaneously solves for the source location and moment tensor of a microseismic event. Not only does the algorithm fail to perform at the signal-to-noise ratios indicated by the WGN results but the results with realistic modelled noise highlight pitfalls of the algorithm not previously identified. The misleading results from the WGN datasets highlight the need to test algorithms under realistic noise conditions to gain an understanding of the conditions under which an algorithm can perform and to minimise the risk of misinterpretation of the results.

3.1 Introduction

Synthetic datasets are used on a daily basis by geophysicists to test hypotheses, test the sensitivity of algorithms and to provide confidence limits. Unfortunately, in the real world noise contaminates all seismic recordings to varying degrees. *Forghani-Arani et al.* (2012) highlighted that the presence of coherent noise in seismic imaging can result in the introduction of artefacts, while in seismic inversion it can lead to errors in the estimated velocity model and predicted source parameters. Therefore, to provide more realistic synthetic seismic data, noise with Gaussian characteristics is commonly added.

In general, the choice of Gaussian noise is primarily to simplify implementation or demonstrate mathematical properties such as optimality and unbiasedness, rather than based upon physical principles. In many ways, Gaussian noise only serves to obscure seismic arrivals or events rather than providing a sufficiently robust test of processing and imaging algorithms. Discussing the true nature of noise, *Ulrych et al.* (2009) state: 'noise is never white, and noise is seldom, if ever, Gaussian'. Despite this, the Gaussian noise assumption has resulted in many techniques being developed specifically to suppress Gaussian noise (e.g., *Green et al.*, 1966, *Berkner and Wells Jr*, 1998, *Bekara et al.*, 2003). A recent study by *Birnie et al.* (2016) introduced the Isolated COVAriance noise modelling method (ICOVA) which was shown to accurately approximate noise

through a multivariate Gaussian process.

In this paper we look at the effect of noise on the performance of microseismic event detection and imaging algorithms. Having a robust automated detection procedure is of particular importance for providing real-time calculations on the likelihood of seismic-induced hazards and complying with local regulations (*Majer et al.*, 2012). Microseismic events and their properties provide important information on not just the temporal and spatial distribution of events but also on the failure mode and prevailing stresses which aid reservoir understanding and development (*Chambers et al.*, 2014).

Using the microseismic scenario as an example, synthetic datasets were created by adding recorded noise and modelled noise to simulated microseismic events at the Aquistore carbon dioxide (CO_2) storage site. Two different types of modelled noise were generated, White, Gaussian Noise (WGN) and realistic ICOVA modelled noise, with their effects benchmarked against semi-synthetic datasets containing recorded noise. The first section of the paper aims to demonstrate the similar behaviour of standard microseismic event detection and imaging algorithms when handling recorded noise and ICOVA modelled noise, whereas very different behaviour is observed on datasets with WGN. The latter part of the paper focusses on demonstrating the requirement of developing and testing algorithms under realistic noise conditions. Introducing an iterative moment tensor inversion procedure the results illustrate how not only are different thresholds for performance identified but also how the behaviour of the technique changes between WGN and realistic noise conditions. This highlighted pitfalls that are vital to know to avoid misinterpretation of results when applying the algorithm to field data.

3.2 Data

The data used in this study are a combination of recorded noise data, modelled noise data and synthetic waveform data.

3.2.1 Noise data

The recorded noise data comes from a permanent surface array installed at the Aquistore CO_2 storage site, located in South Saskatchewan, Canada in the northern part of the Williston Basin (*Roach et al.*, 2015). The array has been recording since 2012 July 25 and consists of 51 buried, vertical component geophones with a cross-shaped geometry as illustrated in Figure 3.1. A subset of the data from 25 July to 5 October 2012 is used in this study. A previous noise analysis by *Birnie et al.* (2015) identified and characterised noise signals from this recording and labelled them as stationary, non-

stationary and pseudo-non-stationary dependant on their temporal properties. In this study we consider the following 3 noise scenarios,

1. stationary noise,
2. stationary noise with increased noise levels around the centre of the array, and
3. the onset of the increased noise levels, i.e., the transition between scenario 1 and 2.

Examples of recorded noise for each scenario are given in Figure 3.2(a-c). Due to the low number of traces on which a non-stationary noise signal is present it is not included in this study.

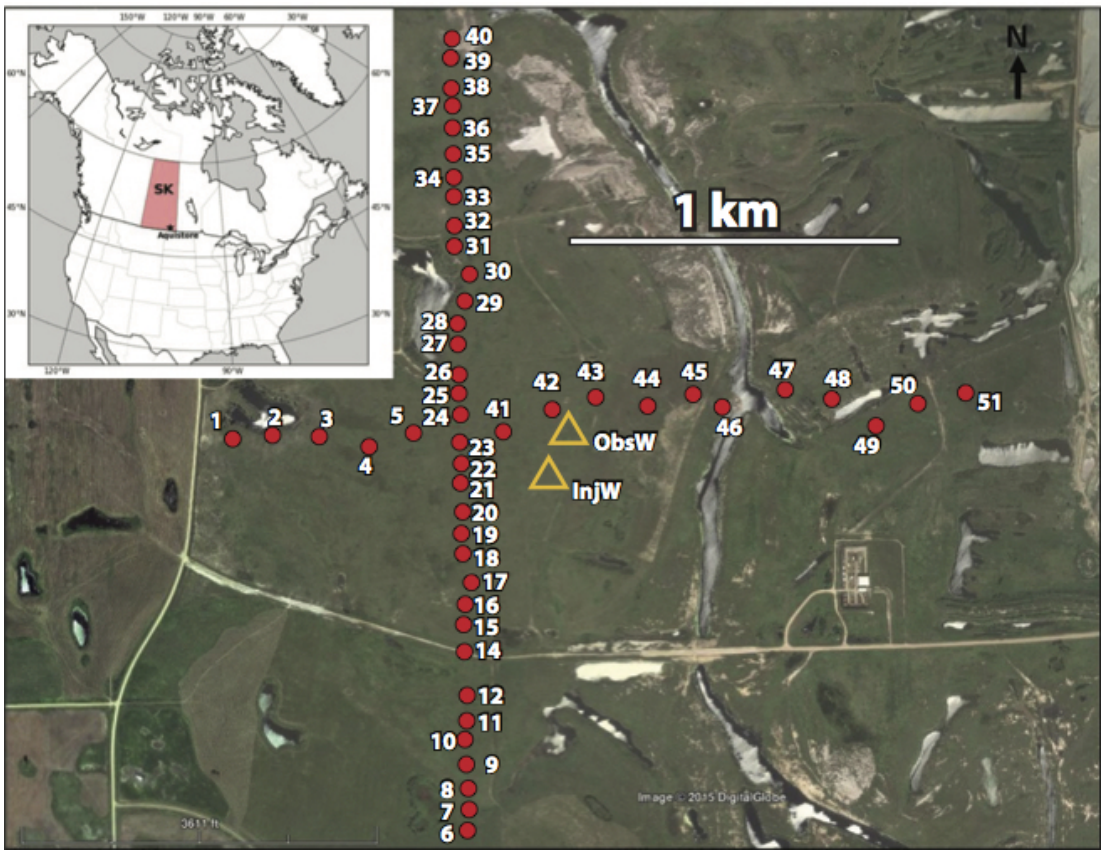

Figure 3.1: *Permanent seismic array survey geometry at Aquistore CO_2 storage site in Saskatchewan, Canada. Geophones are denoted by red dots alongside the station number, while the observation and injection wells are illustrated by yellow triangles. (Appeared as figure 2 in (Birnie et al., 2016).)*

The modelled noise data is computed using two different approaches: the standard WGN approach and the novel ICOVA approach. The modelled data are generated and later scaled when combined with the waveform data. To create WGN, a matrix the same shape as the recorded noise data section is generated using random samples from a standard normal distribution (i.e. a Gaussian distribution with zero mean and

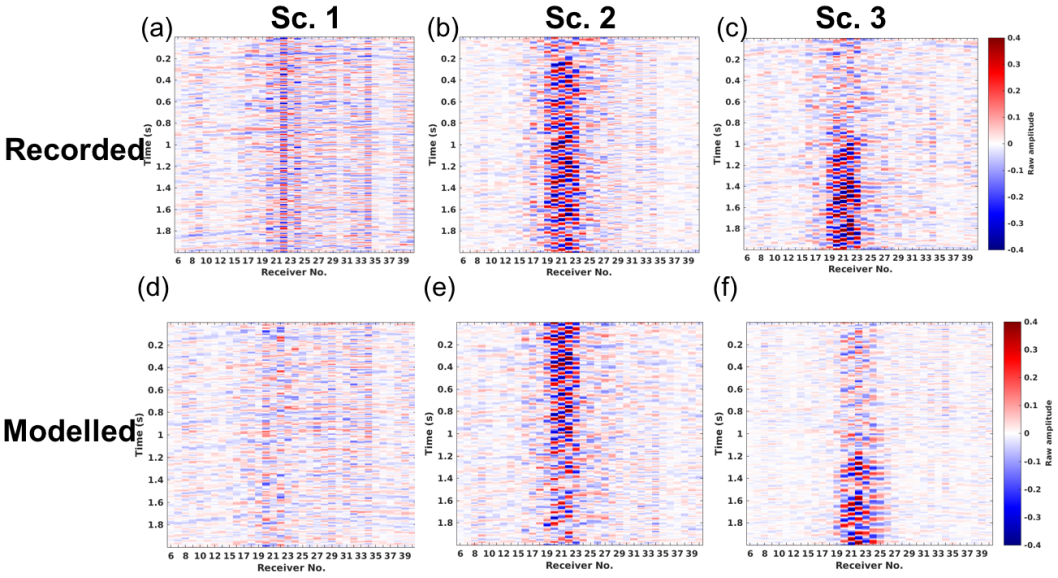

Figure 3.2: *Noise scenarios investigated with the top row being recorded noise examples and the bottom row being ICOVA modelled noise examples. The left-hand column is the first noise scenario with a reasonably even distribution in noise energy across the array, the middle column is the second noise scenario with an area of heightened noise energy around the center of the array, and the right-hand column is a transition between the first two noise scenarios.*

unit variance). The workflow for the ICOVA modelling method is given in Figure 3.3. The noise model is generated by computing the mean and covariance of recorded noise signals and uses these to generate realisations of a multi-variate Gaussian distribution with the same statistical properties as the recorded noise, as described by *Birnie et al.* (2016). Noise models are created for the 3 scenarios described above and examples of each are given in Figure 3.2(d-f). It is important to observe that the noise models are not generated to be identical to the recorded noise but instead are generated to have the same statistical properties.

For the Signal-to-Noise Ratio (SNR) analysis and event detection procedure all three noise scenarios are investigated. Due to the varying nature of noise, 100 realisations of both recorded noise and modelled noise are used for each scenario. Excluding scenario 3 for recorded noise where only one example of this is present in the recorded data.

The imaging procedures are significantly more expensive computationally, therefore only 1 realisation of each noise model has been used focussing on comparing the first and second noise scenarios, i.e. where the relative strength of the noise is roughly constant across the array versus where there is a clear area of heightened noise in the center of the array.

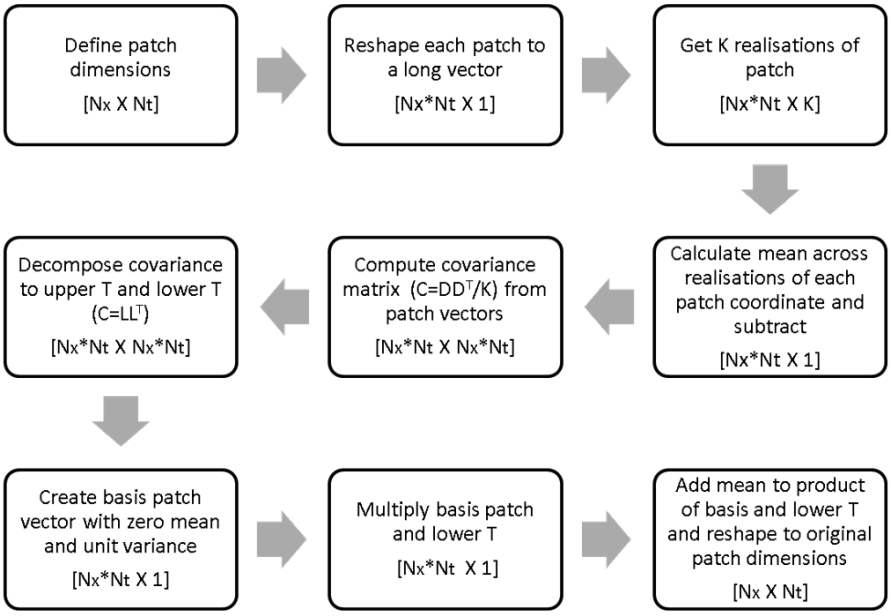

Figure 3.3: *Workflow for covariance-based noise modelling. (Appeared as figure 1 in (Birnie et al., 2016).)*

3.2.2 Waveform data

The waveform data is generated using E3D (*Larsen and Harris*, 1993) (an elastic wave propagation code) and aims to imitate a microseismic event at the Aquistore CO_2 storage site. Using the Aquistore subsurface model of *Roach et al.* (2015), the subsurface is modelled as a 16-layer, laterally homogeneous, isotropic medium. Figure 3.4 illustrates the subsurface model and velocity and density logs used in the wave propagation.

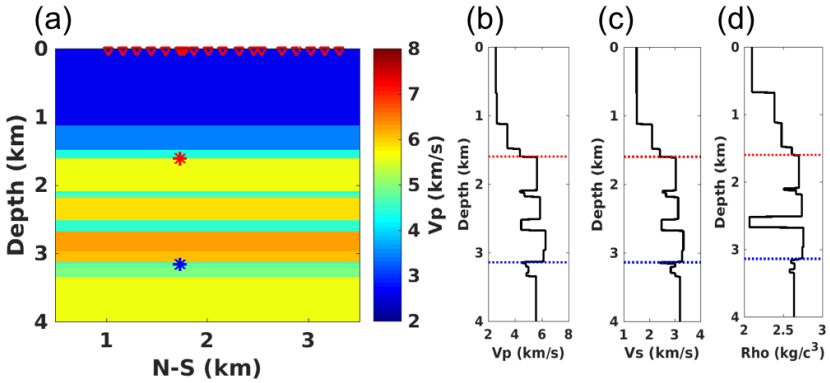

Figure 3.4: *(a) Velocity model, and (b) P-wave velocity, (c) S-wave velocity and (d) density logs. Red triangles denote receiver locations. The blue star on the velocity model and blue dashed lines on logs represent the reservoir location while the red star on the velocity model and red dashed lines on logs represent the sources location.*

Waveform data of two events at the same subsurface location were generated for this

study. The first is an explosive event used in all the analysis except for the iterative moment tensor inversion procedure where the event has been modelled to mimic a fault reactivation with a moment tensor where $M_{xx} = -1$, $M_{yy} = 1$, and $M_{zz} = M_{xy} = M_{xz} = M_{yz} = 0$ (i.e., normal thrust fault). The events occur below the centre of the receiver array and at a depth of 1600m - halfway between the surface and the reservoir. The event depth was chosen due to the relationship between model size and computational cost for Reverse Time Imaging (RTI), one of the methods investigated in the point source imaging analysis.

3.2.3 Test datasets

The datasets used in each analysis are a combination of waveform data superimposed on noise data. As described in the methodology, the root-mean-square (RMS) of the waveform data has been computed within a 0.2s window containing the direct arrival, and its inverse has been applied to produce a scaled waveform data, $\bar{S} = S/RMS_{Array}(S)$, with unit RMS. Similarly, the noise dataset has been scaled by its own RMS value and divided by the desired SNR of the test dataset, $\bar{N} = N/(RMS_{Array}(N) \cdot SNR_{Array}(D))$, prior to summing to the scaled waveform data, $D = \bar{S} + \bar{N}$. The mathematical terms are defined in the following section alongside the methodology to compute the values.

From here-on, the datasets created through the combination of recorded noise and waveform data will be referred to as semi-synthetics (SS), the datasets of WGN and waveform data will be referred to as WGN synthetics and the datasets of ICOVA modelled noise and waveform data will be referred to as ICOVA synthetics.

3.3 Methodology

This section details the techniques used to investigate the influence of noise on the results from microseismic monitoring procedures. To consider the similarity between the effect of recorded noise and modelled WGN and ICOVA noise three areas considered. These are individual stations' SNR, an event autotrigger algorithm, point source imaging using both a diffraction stack and a reverse time approach.

The study concludes with the introduction of an iterative scheme for focal mechanism determination and imaging which is tested under WGN and realistic noise conditions to identify the conditions under which the algorithm produces acceptable results.

3.3.1 Station SNR investigation

The stations' SNR investigation considers how the SNR varies across the array by computing the SNR at each receiver for a given array SNR. In order to compute the array SNR, we define $RMS_{Array}(A)$ as the RMS of amplitudes computed from all receivers over a 0.2s window around the first break,

$$RMS_{Array}(A) = \sqrt{\frac{\sum_{j=1}^{n_x}\sum_{i=1}^{n_t} A_{i,j}^2}{n_x n_t}}. \tag{3.1}$$

The station SNR requires instead the computation of $RMS_{Station}(A_j)$ defined as the RMS of amplitudes for a single station over the same 0.2s window,

$$RMS_{Station}(A_j) = \sqrt{\frac{\sum_{i=1}^{n_t} A_{i,j}^2}{n_t}} \tag{3.2}$$

where $A_{i,j}$ is the amplitude of a trace j at time point i, n_x is the number of stations, and n_t is the number of time points.

These RMS values are computed over the same time window on the waveform ($A = S$) and noise ($A = N$) data separately prior to computing SNR of the test dataset, D (i.e. the combined noise and waveform data), defined as

$$SNR_{Array}(D) = RMS_{Array}(S)/RMS_{Array}(N) \tag{3.3}$$

where $RMS_{Array}(S)$ is the array RMS derived from the waveform data and $RMS_{Array}(N)$ is the array RMS derived from the noise data. Similarly, to obtain the SNR of a single station j,

$$SNR_{Station}(D_j) = RMS_{Station}(S_j)/RMS_{Station}(N_j) \tag{3.4}$$

where $RMS_{Station}(S_j)$ is the station RMS computed from trace j of the waveform data and $RMS_{Station}(N_j)$ is the station RMS derived from the same trace j of the noise data.

Finally, to consider how SNR varies across stations, the SNR of each station has been normalised by the SNR of the array.

3.3.2 STA/LTA autotrigger

Due to the large volumes of data recorded and the computational cost of microseismic imaging algorithms it is preferable to run an autotrigger to detect potential seismic events to be imaged as opposed to running imaging procedures on the full recordings. The 'short-time-average to long-time-average' (STA/LTA) trigger works by continuously calculating the mean value of the absolute amplitudes of the seismic data within two sliding time windows. As the short time average (STA) is sensitive to seismic events and the long time average (LTA) is sensitive to the background noise then an event can be detected when the ratio of STA to LTA exceeds a predetermined value.

In an approach similar to that used by *Stork et al.* (2015), ObsPy's 'classic sta-lta' (*Beyreuther et al.*, 2010) was used with a STA window length of 0.75s and a LTA window length of 3s. For a trigger to occur the STA/LTA must be greater than 10 on a minimum of 5 stations within a trigger window.

3.3.3 Point source imaging

There are two main approaches to microseismic imaging: a diffraction stack approach and a reverse time approach (*Schuster*, 2002). While techniques have advanced to incorporate methods of handling moment tensor sources, the above two approaches still provide the fundamental building blocks of these techniques, for example *Chambers et al.* (2010) used a diffraction stack approach whereas *Artman et al.* (2010) used a reverse time approach. In this study, we return to these fundamental approaches analysing the effect of noise on the resulting source locations.

Diffraction Stack Imaging (DSI) is based on the methodology of assessing the spatial coherency of waveforms through stacking for speculative points in the subsurface (*French*, 1974). By computing a stack function throughout a volume of interest (through the selection and summation of data consistent with arrivals from speculative origin times and locations), the position and timing of a source can be inferred from the position of maximal values in the stack function (*Chambers et al.*, 2014). The step-by-step methodology used in this paper is similar to that described by *Zhebel et al.* (2011).

RTI utilises the symmetry of the wave equation which allows for the recorded wavefield to be reversed in time and back-propagated into the subsurface (*McMechan*, 1983). For the microseismic scenario, the time-reversed data are injected into the model domain at the receivers as sources and the propagation causes events to focus at the source location (*Artman et al.*, 2010). In this study we have used an acoustic wave propagation code from the Madagascar software package to propagate the recorded wavefield from the receivers into the subsurface.

3.3.4 Moment tensor imaging

Both the diffraction stack and reverse time imaging methods discussed in the previous section are relatively simple source imaging procedures. In particular they do not take account of the anisotropic radiation pattern produced by a microseismic source mechanism. This radiation pattern typically leads to a lobed pattern in standard images and can lead to a mislocation of the seismic source.

A number of techniques exist to resolve this ambiguity (for example, *Özbek et al.*, 2013, *Anikiev et al.*, 2014, *Chambers et al.*, 2014). Here we describe such a scheme which combines an imaging procedure with moment tensor inversion solving simultaneously for the location and focal mechanism. The scheme is referred to as Iterative Location and Mechanism Analysis (ILMA) and is performed using the outlined steps:

1. A standard imaging stack is performed (with no polarity correction),
2. Maxima are selected from the image and averaged to get a central source position,
3. The source position and travel times are used to select P-wave data amplitudes,
4. The source position, travel times, and receiver positions are used to construct moment tensor kernels,
5. An inversion is performed for the best fitting moment tensor, and the DC component is taken,
6. The data amplitudes are forward modelled and a vector of $+/-1$'s is constructed to flip the data traces based on the modelled data amplitudes,
7. The data traces are flipped accordingly,
8. Return to step 1 for the next iteration, replacing the input stack data with the polarity adjusted data from step 7, and the point source function is now based on the maxima of the stack function.

Before going to a new iteration a check for convergence is performed, by comparing the derived polarity flips in step 7 with those from the previous iteration. The procedure exits when all polarity flips fail to change between iterations or the maximum number of iterations has been exceeded, in this case 6.

A few extensions to the procedure have been added specifically for the Aquistore array. Prior to imaging the P-wave arrival is cleaned by cross-correlating with a reference pulse that has been estimated through an eigentrace decomposition of the original P-wave arrivals. This provides a more impulsive wavelet for the imaging procedure. The array geometry is such that for a source positioned under the centre of the array the M_{xy} component of a moment tensor sits inside the null space of the moment tensor amplitude

kernels. As such it cannot be constrained effectively; errors are likely to be projected on to the M_{xy} component; and it can cause instabilities. Therefore, to improve stability, we ignore the M_{xy} component during the imaging procedure. Another effect of the array geometry is that the image is smeared along the E-W direction due to the array being more densely sampled running N-S. To reduce this artefact, images are created for the N-S and E-W receiver profiles individually and then combined. This effectively down weights the N-S sensors relative to the E-W sensors therefore reducing the smear.

3.4 Results

3.4.1 Station SNR investigation

The SNR analysis looks at the individual station SNR for datasets with an array SNR of 1. Figure 3.5 illustrates the variation in SNR across the array for the three different noise scenarios. For all three scenarios the SS and ICOVA datasets have a decrease in SNR on receivers around the center of the array., whereas for the WGN datasets, the noise level is constant across the array therefore the receiver SNR is highest above the source location, i.e. in the center of the array. Table 3.1 illustrates the range in SNR values across the array. For all three scenarios, the WGN dataset has a range of approximately 0.6 across the array whereas the SS and ICOVA datasets have a range of approximately 3 for scenario 1 and even higher for scenario 2 and 3.

Table 3.1: *Mean range of station SNR across receiver array*

Noise type	**Scenario**		
	1	**2**	**3**
WGN	0.57	0.55	0.55
Semi-synthetic	3.36	5.98	5.76*
ICOVA	3.20	5.74	4.60

The ICOVA results closely imitate the SS results for scenarios 1 and 2 in both average station SNR and the standard deviation of the station SNR (i.e. error bar size). For scenario 3, the ICOVA results vary slightly from the SS results. This can be attributed to the ICOVA dataset being generated from over 200 examples of noise while the SS results are from a single recording and therefore may experience variations from the average noise properties that the ICOVA noise model does not account for.

3.4.2 STA/LTA autotrigger

Figure 3.6 illustrates the number of stations that trigger an event at increasing array SNRs. The SS and ICOVA datasets begin to trigger significantly earlier than the WGN

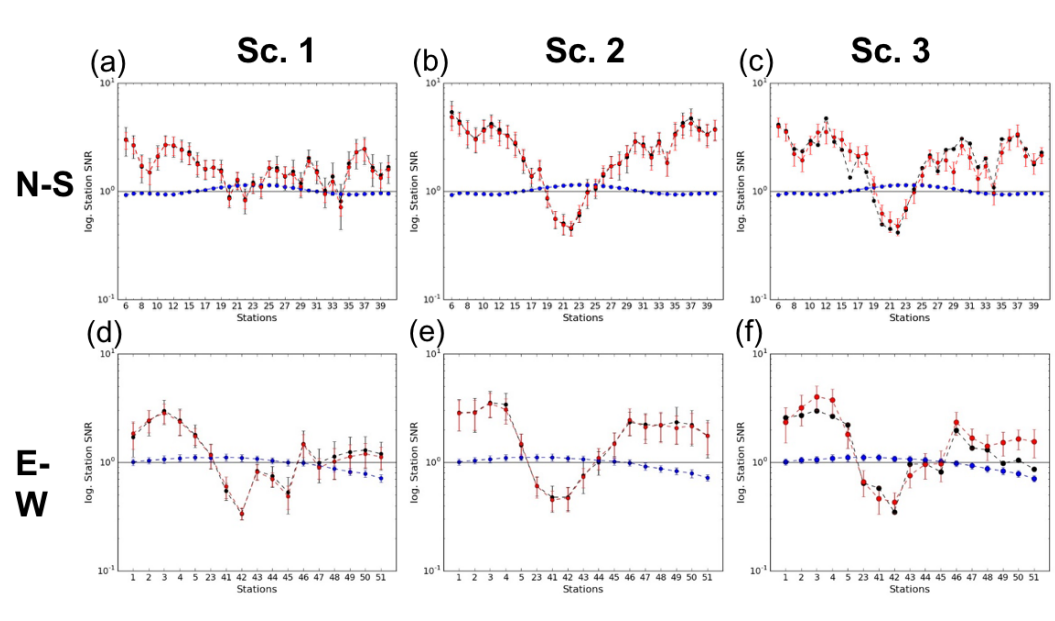

Figure 3.5: *Individual stations' SNR of waveform data with recorded noise (black), WGN (blue), and ICOVA noise (red) at an array SNR of 1. The left column represents individual station SNRs for noise scenario one, middle column for noise scenario two and final column for noise scenario three. Data points represent mean from 100 realisations, while error bars represent 2 standard deviations. Note logarithmic scale of y-axis and that there are no error bars on recorded noise for scenario three as only one realisation is available.*

dataset for all 3 noise scenarios. However once triggered the WGN has a much steeper gradient therefore having less of transition between the SNR at which a few stations are triggered and the SNR at which all stations are triggered.

Focussing on noise scenario 2, Figure 3.7 identifies the stations on the N-S receiver profile which are triggered. For the SS and ICOVA datasets the stations are triggered from the outside-in, whereas the opposite is observed with the WGN dataset. This is due to the WGN datasets have highest station SNR in the center of the array where the SS and ICOVA datasets have highest station SNRs at the receivers at the edge of the arrays. As noted above, the WGN dataset does not trigger any stations until significantly higher SNRs than the SS and ICOVA datasets but once it begins to trigger more stations are triggered than for the SS and ICOVA datasets.

3.4.3 Point source imaging

DSI and RTI was performed on datasets with array SNR of 0.1, 0.3, and 0.5 for noise scenarios 1 and 2.

Image volume slices from the DSI are illustrated in Figure 3.8. For both noise scenarios at an array SNR of 0.1, DSI identifies the correct source location for the WGN dataset however the image maxima for both the SS and ICOVA datasets correspond to artefacts

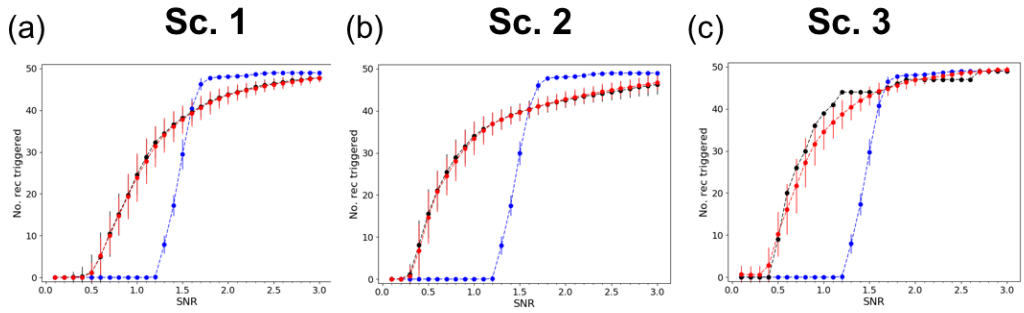

Figure 3.6: *Number of stations triggered at increasing array SNRs for noise scenarios (a) one, (b) two, and (c) three of waveform data with recorded noise (black), WGN (blue), and ICOVA noise (red). Data points represent mean from 100 realisations, while error bars represent 2 standard deviations. Note there are no error bars on recorded noise for scenario three as only one realisation is available.*

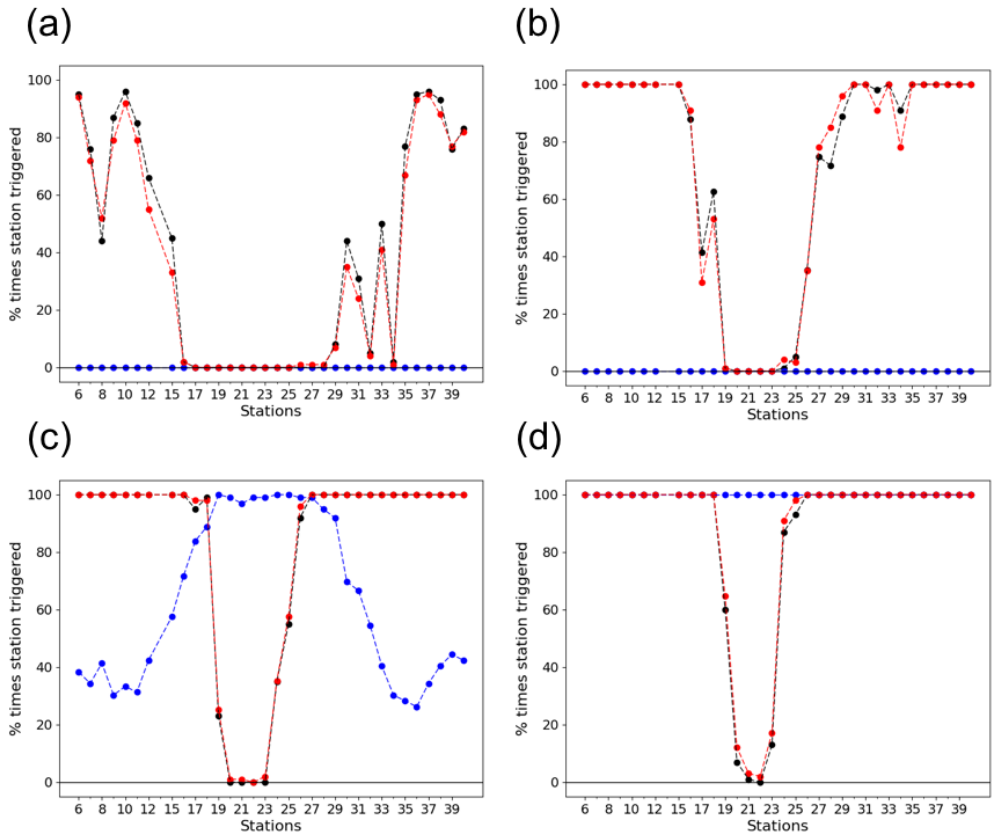

Figure 3.7: *Identification of which stations on N-S receiver line trigger at array SNR of (a)* 0.5*, (b)* 1.0*, (c)* 1.5*, and (d)* 2.0 *for waveform data with recorded noise (black), WGN (blue), and ICOVA noise (red) for noise scenario two.*

in the image. Noise artefacts are present in the WGN dataset's image volume however these have significantly lower amplitude than the seismic source maxima. While the

image maxima is in the source location for all datasets at an array SNR of 0.3, there is still a significant presence from coherent noise artefacts in the SS and ICOVA image volumes. These artefacts are reduced further as the SNR increases to 0.5 however the artefacts remain still contain a small amount of energy.

Image volume slices from the RTI are illustrated in Figure 3.9. At an array SNR of 0.1, the source location is visibly identifiable on all three image slices shown however the image maxima for the ICOVA and SS datasets are due to noise artefacts. Similar to the DSI results, there is a noticeable structure to the noise artefacts present in the SS and ICOVA image volumes however, due to the nature of WGN, the noise artefacts in the WGN image volumes are randomly dispersed. At SNR of 0.3, the maxima identify the source location for the SS and ICOVA datasets but there is still a strong presence of coherent noise artefacts. These are reduced further, but still present, at a SNR of 0.5.

3.4.4 Moment tensor imaging

ILMA was performed on datasets at array SNR of 0.1, 0.3, and 0.5 for noise scenarios 1 and 2. Figure 3.10 shows an E-W image slice from the final iteration of ILMA while Figure 3.11(a,b) illustrates the number of iterations for the polarisation corrections to converge, noting that the maximum number of iterations allowed was 6, with Figure 3.11(c,d) portraying the error in the final source location. Figure 3.12 illustrates the focal mechanisms computed by the final iteration of the iterative scheme and Table 3.2 provides a quantitative portrayal of the variance of the properties derived from the moment tensor decomposition, i.e. the eigenvalues of the moment tensor corresponding to the T-, null-, and P-axes, and the seismic moment.

WGN converges within the iteration allowance and to correct source location for all SNR with a reasonably accurate moment tensor with little variance observed in the properties derived from the moment tensor decomposition. At a SNR of 0.1 for both noise scenarios, SS and ICOVA do not converge within the iteration allowance and unsurprisingly produces an unfocussed image slice with incorrect source locations and moment tensors computed. Noise scenario 2 experiences almost double the source location error than noise scenario 1 at SNR of 0.1. For noise scenario 1, at SNR of 0.3 both the SS and ICOVA results converge well within the iteration allowance however both converge to incorrect source locations with incorrect moment tensors. At SNR of 0.5, all the datasets have converged within the iteration allowance and to the correct source location with an acceptable moment tensor. Figure 3.13 considers the decomposition of the focal mechanism into its double-couple (DC), volumetric (CLVD) and explosive (ISO) components. It's shown that for all synthetic datasets with WGN, the majority of the derived source mechanism is DC with minimal CLVD and ISO

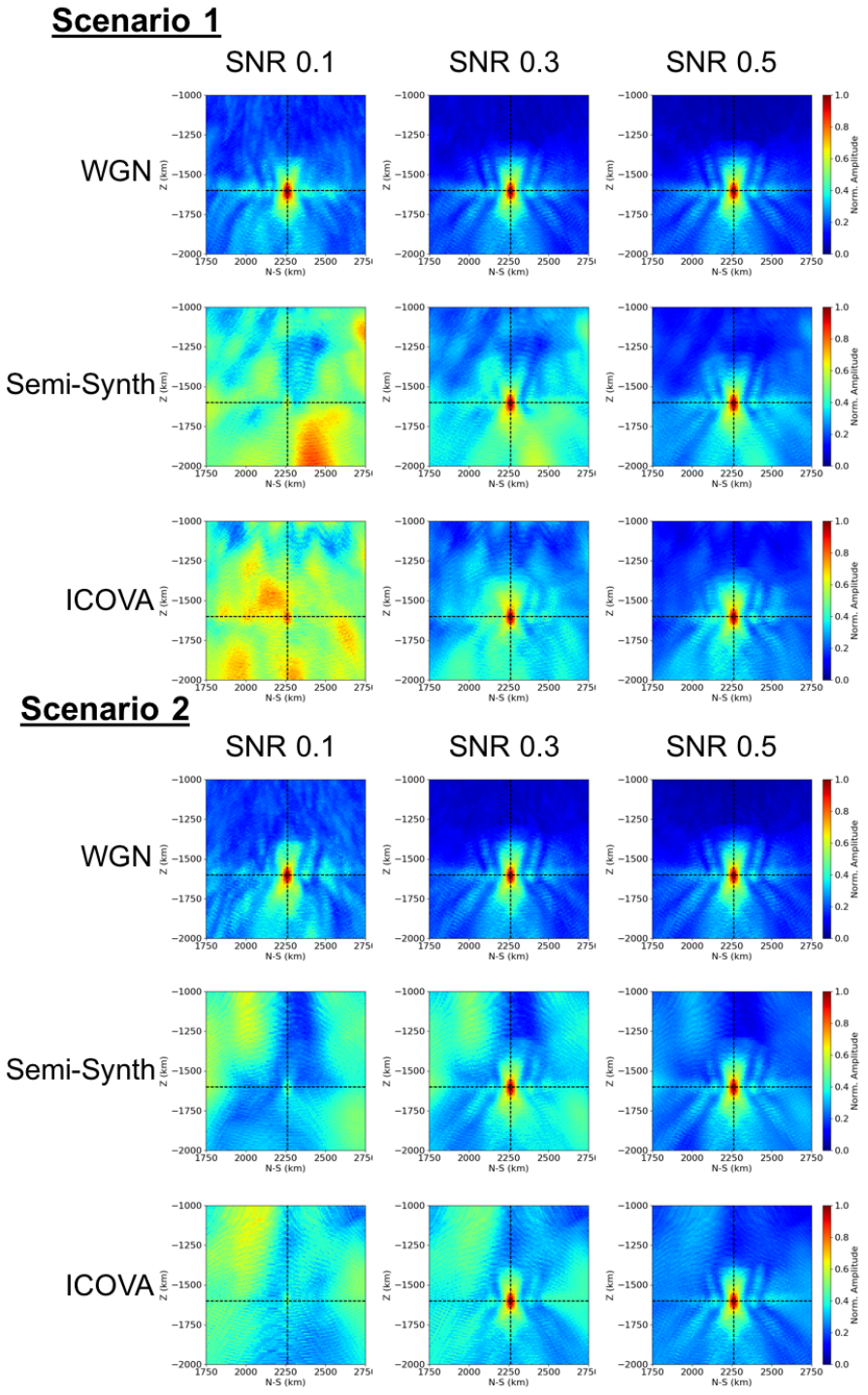

Figure 3.8: *E-W slice of diffraction stack image volumes for scenario 1 (top half) and scenario 2 (bottom half) of waveform data with WGN (top row), recorded noise (middle row) and ICOVA modelled noise (bottom row) datasets computed at SNR of 0.1 (left column), 0.3 (middle column) and 0.5 (right column). Black dashed lines represent source position on N-S and depth axis. Note amplitudes have been normalised across the full image volume.*

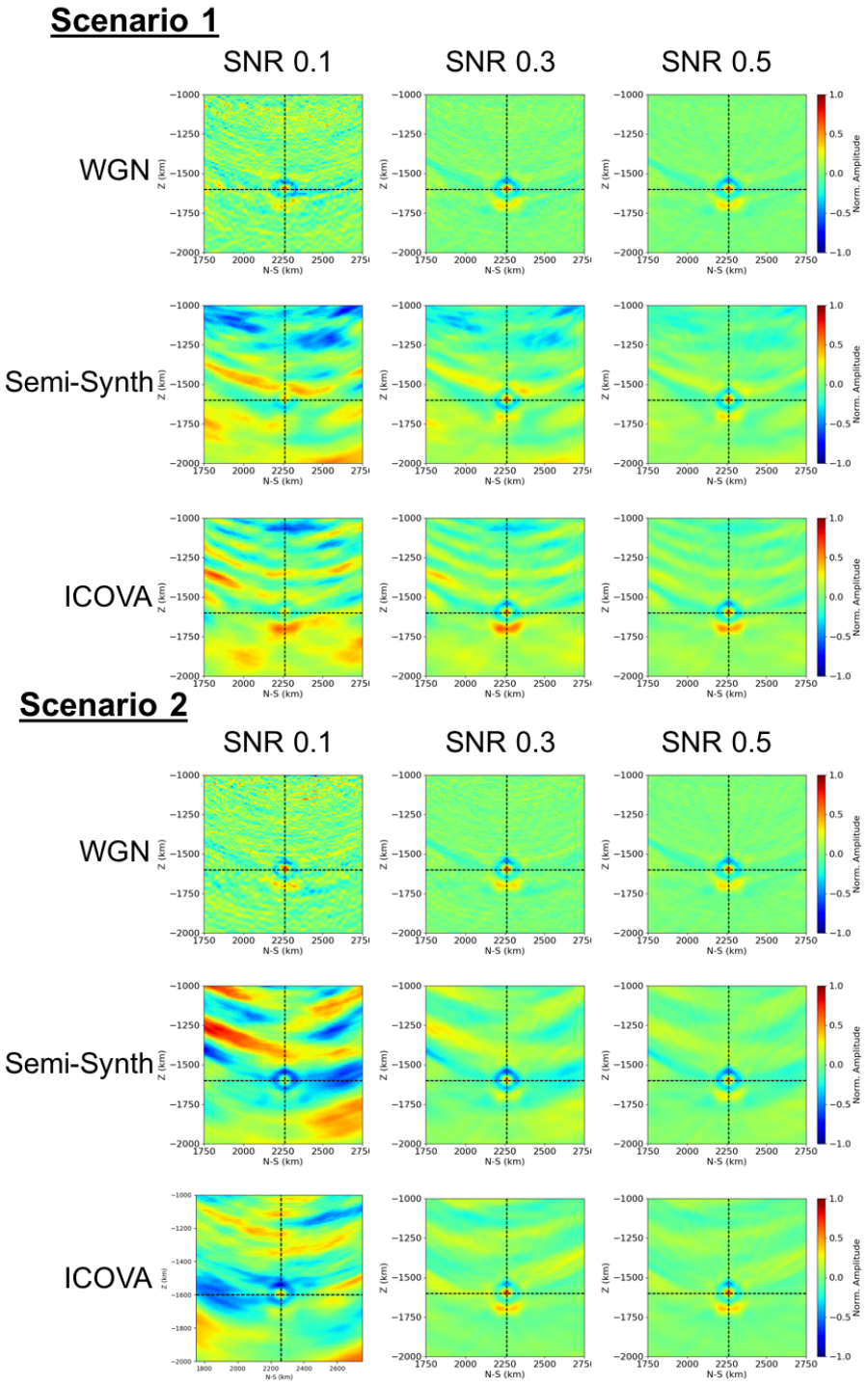

Figure 3.9: *E-W slice of reverse time image volumes for scenario 1 (top half) and scenario 2 (bottom half) of waveform data with WGN (top row), recorded noise (middle row) and ICOVA modelled noise (bottom row) datasets computed at SNR of 0.1 (left column), 0.3 (middle column) and 0.5 (right column). Black dashed lines represent source position on N-S and depth axis. Note amplitudes have been normalised across the full image volume.*

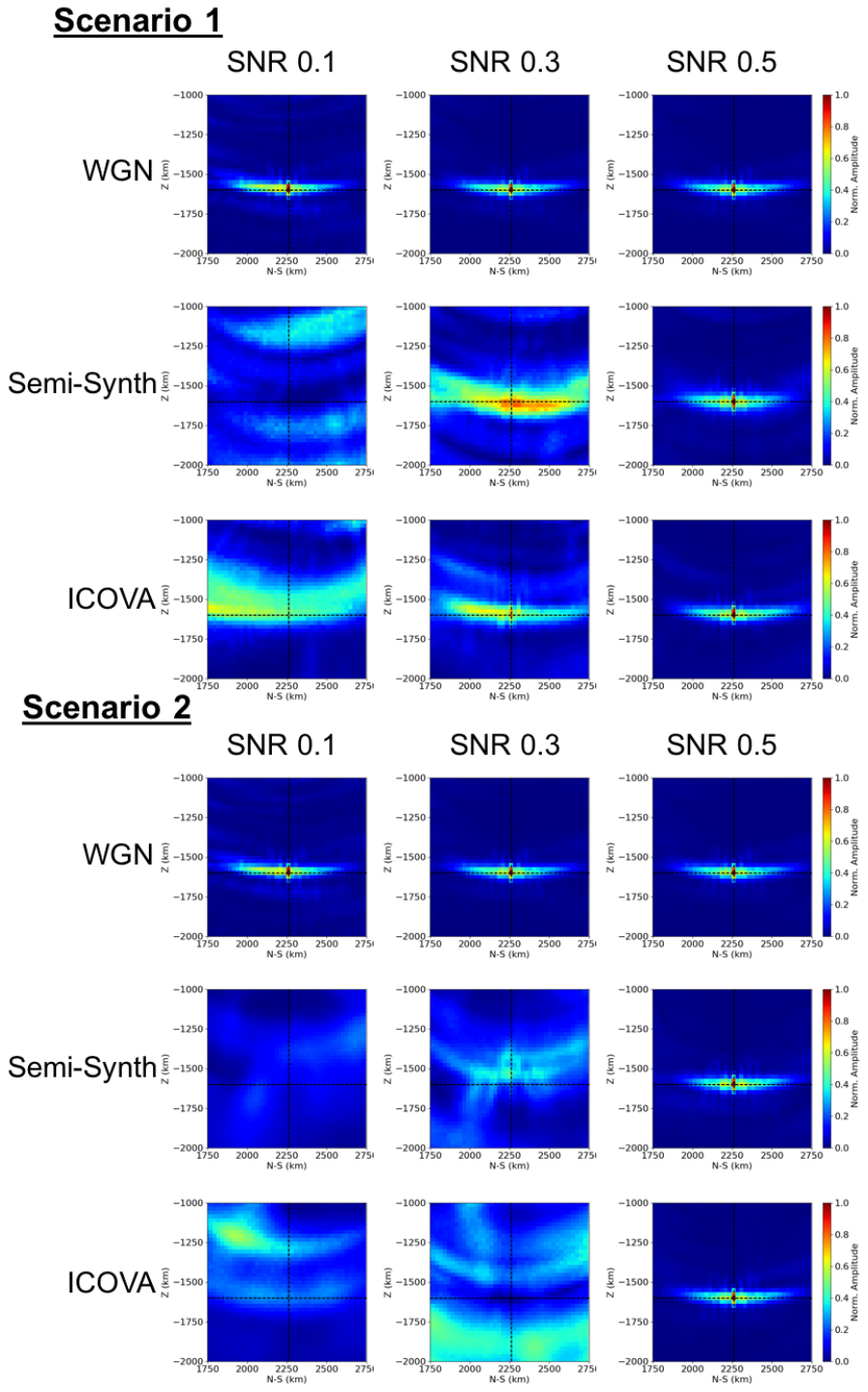

Figure 3.10: *E-W slice of ILMA image volumes for scenario 1 (top half) and scenario 2 (bottom half) of waveform data with WGN (top row), recorded noise (middle row) and ICOVA modelled noise (bottom row) datasets computed at SNR of 0.1 (left column), 0.3 (middle column) and 0.5 (right column). Black dashed lines represent source position on N-S and depth axis. Note amplitudes have been normalised across the full image volume.*

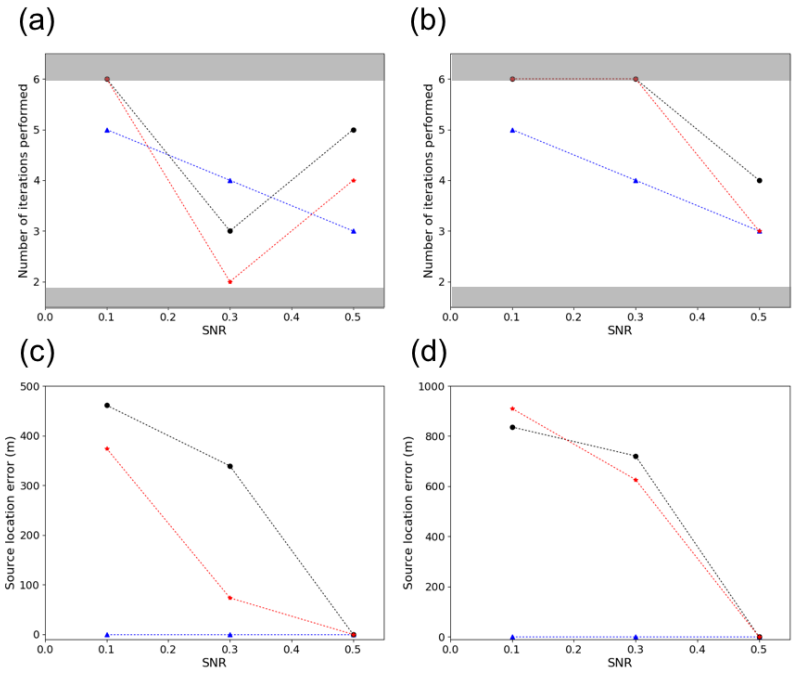

Figure 3.11: *Number of iterations utilised (top row) and source location error from final iteration source location (bottom row) results from ILMA for scenario 1 (left column) and scenario 2 (right column) for waveform data with recorded noise (black), WGN (blue), and ICOVA noise (red). Note that the minimum number of iterations is 2 and the maximum number of iterations is 6.*

Table 3.2: *Eigenvalues of the moment tensor corresponding to the T-, null-, and P-axes shown as EV(T), EV(N), and EV(P), respectively, and the seismic moment M_0 for ILMA results from scenario 1 and scenario 2, the top and bottom tables respectively. Grey cells indicate where the solution has failed to converge within the iterative allowance.*

Scenario One

	SNR 0.1			**SNR 0.3**			**SNR 0.5**		
	WGN	**SS**	**ICOVA**	**WGN**	**SS**	**ICOVA**	**WGN**	**SS**	**ICOVA**
EV(T)	-0.71	-0.74	-0.84	-0.7	-0.86	-0.81	-0.69	-0.7	-0.7
EV(N)	-0.06	-0.71	-0.55	-0.04	-0.57	-0.33	-0.05	-0.14	-0.05
EV(P)	0.70	-0.15	0.05	0.72	-0.03	0.52	0.72	0.70	0.71
$\boldsymbol{M_o}$	0.75	0.92	0.94	0.73	0.94	0.94	0.73	0.8	0.74

Scenario Two

	SNR 0.1			**SNR 0.3**			**SNR 0.5**		
	WGN	**SS**	**ICOVA**	**WGN**	**SS**	**ICOVA**	**WGN**	**SS**	**ICOVA**
EV(T)	-0.71	0.86	0.50	-0.70	0.80	-0.28	-0.69	-0.67	-0.67
EV(N)	-0.06	0.61	-0.12	-0.04	0.67	0.29	-0.05	-0.04	-0.02
EV(P)	0.7	-0.33	-0.93	0.72	-0.48	1.09	0.72	0.74	0.75
$\boldsymbol{M_o}$	0.75	1.09	0.93	0.73	1.14	1.09	0.73	0.74	0.75

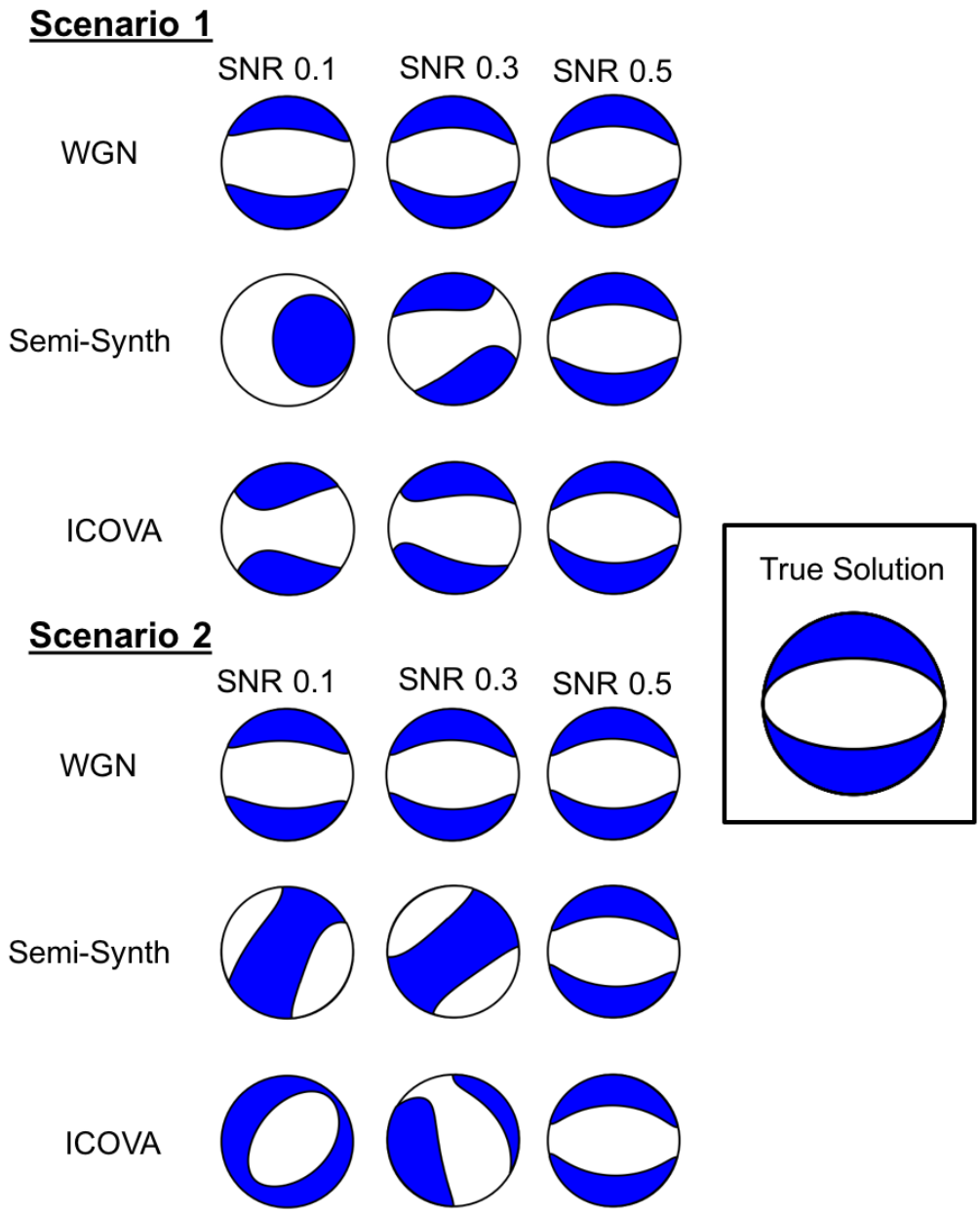

Figure 3.12: *Focal mechanism beachballs derived from ILMA for scenario 1 (top half) and scenario 2 (bottom half) of waveform data with WGN (top row), recorded noise (middle row) and ICOVA modelled noise (bottom row) datasets computed at SNR of 0.1 (left column), 0.3 (middle column) and 0.5 (right column). With the true solution given in the box to the right. The colour denotes areas of contraction.*

components. However, this is only the case for the SS and ICOVA synthetics once the SNR has reached 0.5. Below this both SS and ICOVA datasets have a significant proportion of both CLVD and ISO components present in the derived source mechanism.

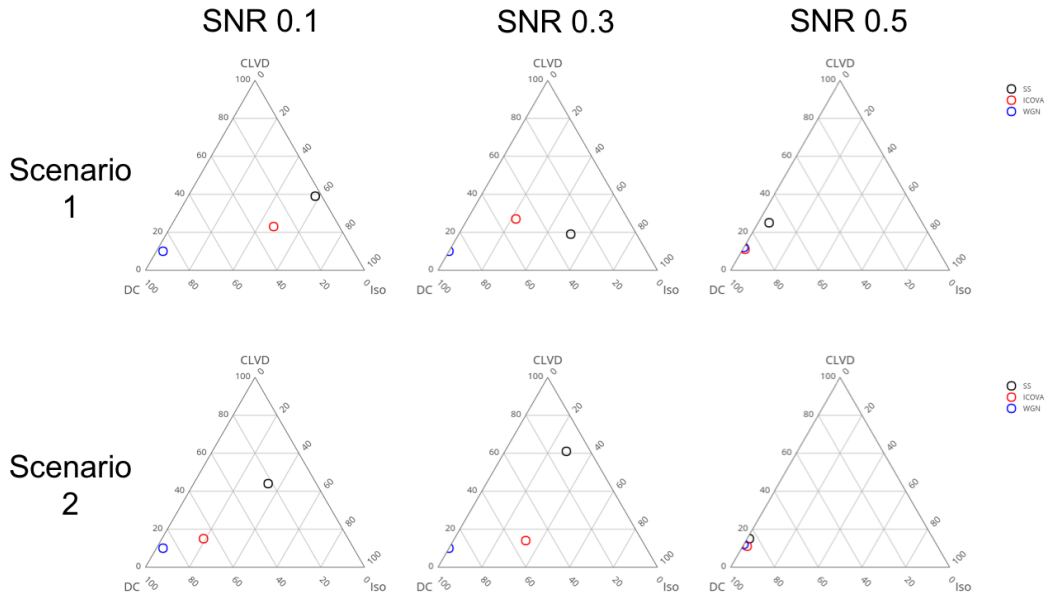

Figure 3.13: *CLVD, DC and ISO components derived from ILMA for scenario 1 (top row) and scenario 2 (bottom row) of synthetic datasets computed at SNR of 0.1 (left column), 0.3 (middle column) and 0.5 (right column). Black markers denote synthetic datasets with recorded noise, red markers datasets with ICOVA noise and blue with WGN noise. The CLVD component follows the horizontal axis, the DC follows the* 45° *axis and the ISO component follows the* -45° *axis. The true solution is 100% DC.*

3.5 Discussion

The focus of the first part of this study was to highlight the unrealistic nature of WGN and provide an alternative, more realistic, noise modelling approach, where recorded noise has been used to benchmark the results. Throughout the SNR analysis and event detection and imaging procedures, the WGN datasets continually failed to imitate the results obtained by the SS datasets which contain recorded noise. For the event detection procedure (i.e. STA/LTA) the WGN datasets significantly underestimated the SNR at which an event would trigger however in the imaging procedures the WGN datasets overestimated the algorithm's performance. As discussed by *Chambers et al.* (2010), the fact that the imaging procedures detect events at SNR beyond the STA/LTA is expected.

While WGN is the most commonly used modelling method there are a number of alternative methods. An example of one such method is where the standard deviation of the WGN is varied in order to gain a closer comparison to field data (*Gei et al.*, 2011, *Grechka et al.*, 2011). While this may make the noise more realistic it is still uncorrelated and therefore does not contain the coherent aspects of noise which cause the most trouble in imaging and inversion procedures (*Forghani-Arani et al.*, 2012).

In both DSI and RTI there is a higher similarity between the SS and ICOVA results of opposing scenarios than to the WGN results highlighting that the change in noise energy distribution across the array has less impact on the results than the presence of coherent and incoherent noise.

Where noise data are available an alternative approach is the direct incorporation of realistic noise to create semi-synthetics, for example, the SS datasets used in this study. Realistic noise modelling offers three main advantages over the semi-synthetic approach: 1) once the noise statistics have been computed, the noise data are no longer needed, 2) there is the possibility to extend beyond the geometry in which the noise was originally recorded, and 3) while the recorded noise is finite in time, limiting the extent to which you can test the effect of noise, noise models can be continually made with the same statistical properties allowing algorithms to be tested an infinite number of times. An example of the third advantage is for noise scenario 3 where there was a single example of the noise transition in the hour recording of data used for the semi-synthetic creation. However 100 noise models were created with the same statistical properties as the transition.

The latter part of the study focusses on the necessity of using realistic noise conditions when developing and testing an algorithm. An algorithm's development flow typically follows the procedure of synthetic test prior to applying to a field dataset, for example *Ŝílenỳ et al.* (1996)'s study on the theory and synthetic testing of seismic moment resolution followed by a study applying to a field dataset (*Cespuglio et al.*, 1996). This study introduced ILMA, a moment tensor imaging algorithm, and performed robustness tests with the different noise models. Similar to our previous observations, the ICOVA results are very similar to the SS results. There are notable differences in the behaviour of the technique in response to the WGN and ICOVA datasets. The SNR threshold above which ILMA produces acceptable results is 0.1 for the WGN datasets, however under realistic noise conditions this increases to 0.5. We also observed a potentially misleading convergence for the SS and ICOVA datasets for noise scenario 1 at SNR of 0.3 resulting in an incorrect focal mechanism and source location. This is an indication that convergence alone may not be enough to provide confidence in the solution. Finally, by considering Figure 3.13 the differences between the results from WGN datasets and ICOVA datasets suggests that large amounts of spurious non-DC components are created by the presence of correlated noise. This makes a strong case for whitening data prior to inverting for the MT inversion.

These results are particularly important for monitoring in industrial settings (e.g., hydrocarbon exploration) where instruments are often located close to machinery operations and infrastructure (e.g., roads), sources known to produce large quantities of coherent noise. While there are algorithms that aim to reduce coherent noise to WGN, such as *Birnie et al.* (2017), it is important to identify how successfully these

preprocessing techniques work on the noise data prior to defaulting to WGN for testing algorithms. The stark differences in how WGN and ICOVA noise is handled by ILMA highlights that not only do the realistic noise results not perform at the SNRs indicated by the WGN results but that there are potential pitfalls which are only identified when testing under realistic noise conditions. The inability of synthetic datasets with WGN to mimic the true effects of real noise on the algorithm could lead to misinterpretation of results obtained on field data tests and a misunderstanding of the conditions under which the algorithm can perform.

3.6 Conclusions

In this study we have shown that WGN does not provide any direct comparison to recorded noise and therefore does not provide a reliable indication of how an algorithm will handle noise in a field dataset. For the STA/LTA automated detection method the WGN underestimated the SNR at which an event would be detected, while for imaging procedures WGN overestimated the SNR at which an event can be located. Throughout the study realistic ICOVA modelled noise was also analysed and it continually performed in a similar manner to the recorded noise, therefore providing a reliable indication of how an algorithm will respond to noise in a field dataset. The final section of the analysis focused on the results from robustness tests performed on a moment tensor imaging algorithm. The WGN results implied that the algorithm was robust to high noise levels whereas the semi-synthetic and ICOVA noise results indicated otherwise: light was shed on previously unidentified pitfalls (e.g. the convergence criterion) and a more realistic approximation of the SNR at which the algorithm could perform was found. Understanding how an algorithm handles noise prior to applying it to a field dataset is necessary for an accurate interpretation of the results therefore it is critical that benchmarking is performed under realistic noise conditions.

3.7 Acknowledgements

The authors would like to thank the Petroleum Technology Research Centre (PTRC) for access to Aquistore Data. Aquistore an independent research and monitoring project managed by the PTRC which intends to demonstrate that storing liquid carbon dioxide deep underground (in a brine and sandstone water formation), is a safe, workable solution to reduce greenhouse gases. C. Birnie is funded by the NERC Open CASE studentship NE/L009226/1 and Pinnacle-Halliburton. D. Angus acknowledges the Research Council UK (EP/K035878/1; EP/ K021869/1; NE/L000423/1) for financial support. A.L. Stork thanks the Bristol University Microseismicity Projects (BUMPS)

sponsors for supporting this research.

References

Anikiev, D., J. Valenta, F. Staněk, and L. Eisner (2014), Joint location and source mechanism inversion of microseismic events: Benchmarking on seismicity induced by hydraulic fracturing, *Geophysical Journal International*, *198*(1), 249–258. 3.3.4

Artman, B., I. Podladtchikov, and B. Witten (2010), Source location using time-reverse imaging, *Geophysical Prospecting*, *58*(5), 861–873. 3.3.3

Bekara, M., L. Knockaert, A. Seghouane, and G. Fleury (2003), Seismic signal denoising using model selection, in *Signal Processing and Information Technology, 2003. ISSPIT 2003. Proceedings of the 3rd IEEE International Symposium on*, IEEE. 3.1

Berkner, K., and R. O. Wells Jr (1998), Wavelet transforms and denoising algorithms, in *Signals, Systems & Computers, 1998. Conference Record of the Thirty-Second Asilomar Conference on*, vol. 2, pp. 1639–1643, IEEE. 3.1

Beyreuther, M., R. Barsch, L. Krischer, T. Megies, Y. Behr, and J. Wassermann (2010), Obspy: A python toolbox for seismology, *Seismological Research Letters*, *81*(3), 530–533. 3.3.2

Birnie, C., A. Stork, L. Roach, D. Angus, and S. Rost (2015), Spatial and temporal properties of noise from the aquistore ccs pilot permanent surface array, in *The Third Sustainable Earth Sciences Conference & Exhibition*. 3.2.1

Birnie, C., K. Chambers, D. Angus, and A. Stork (2016), Analysis and models of pre-injection surface seismic array noise recorded at the aquistore carbon storage site, *Geophysical Journal International*. 3.1, 3.1, 3.2.1, 3.3

Birnie, C., K. Chambers, and D. Angus (2017), Seismic arrival enhancement through the use of noise whitening., *Physics of the Earth and Planetary Interiors*, (262), 80–89. 3.5

Cespuglio, G., P. Campus, and J. Ŝílenỳ (1996), Seismic moment tensor resolution by waveform inversion of a few local noisy recordsii. application to the phlegraean fields (southern italy) volcanic tremors, *Geophysical Journal International*, *126*(3), 620–634. 3.5

Chambers, K., J. Kendall, S. Brandsberg-Dahl, J. Rueda, et al. (2010), Testing the ability of surface arrays to monitor microseismic activity, *Geophysical Prospecting*, *58*(5), 821–830. 3.3.3, 3.5

Chambers, K., B. D. Dando, G. A. Jones, R. Velasco, and S. A. Wilson (2014), Moment tensor migration imaging, *Geophysical Prospecting*. 3.1, 3.3.3, 3.3.4

Forghani-Arani, F., M. Batzle, J. Behura, M. Willis, S. S. Haines, and M. Davidson (2012), Noise suppression in surface microseismic data, *The Leading Edge*, *31*(1496–1501), 1496–1501. 3.1, 3.5

French, W. S. (1974), Two-dimensional and three-dimensional migration of model-experiment reflection profiles, *Geophysics*, *39*(3), 265–277. 3.3.3

Gei, D., L. Eisner, and P. Suhadolc (2011), Feasibiliy of estimating vertical transverse isotropy from microseismic data recorded by surface monitoring arrays, *Geophysics*. 3.5

Grechka, V., P. Singh, and I. Das (2011), Estimation of effective anisotropy simultaneously with locations of microseismic events, *Geophysics*, *76*(6), WC143–WC155. 3.5

Green, P. J., E. J. Kelly, and M. Levin (1966), A comparison of seismic array processing methods, *Geophysical Journal of the Royal Astronomical Society*, *11*, 6784. 3.1

Larsen, S., and D. Harris (1993), Seismic wave propagation through a low-velocity nuclear rubble zone, *Tech. rep.*, Lawrence Livermore National Lab., CA (United States). 3.2.2

Majer, E., J. Nelson, A. Robertson-Tait, J. Savy, and I. Wong. (2012), Protocol for addressing induced seismicity associated with enhanced geothermal systems., *US Department of Energy*. 3.1

McMechan, G. (1983), Migration by extrapolation of time-dependent boundary values, *Geophysical Prospecting*, *31*(3), 413–420. 3.3.3

Özbek, A., T. Probert, D. Raymer, and J. Drew (2013), Nonlinear processing methods for detection and location of microseismic events, in *75th EAGE Conference & Exhibition incorporating SPE EUROPEC 2013*. 3.3.4

Roach, L. A., D. J. White, and B. Roberts (2015), Assessment of 4d seismic repeatability and co2 detection limits using a sparse permanent land array at the aquistore co2 storage site, *Geophysics*, *80*(2). 3.2.1, 3.2.2

Schuster, G. T. (2002), Reverse-time migration= generalized diffraction stack migration, in *SEG Technical Program Expanded Abstracts 2002*, pp. 1280–1283, Society of Exploration Geophysicists. 3.3.3

Ŝílenỳ, J., P. Campus, and G. Panza (1996), Seismic moment tensor resolution by waveform inversion of a few local noisy recordsi. synthetic tests, *Geophysical Journal International*, *126*(3), 605–619. 3.5

Stork, A. L., J. P. Verdon, and J.-M. Kendall (2015), The microseismic response at the in salah carbon capture and storage (ccs) site, *International Journal of Greenhouse Gas Control*, *32*, 159–171. 3.3.2

Ulrych, T., S. Taylor, B. Nedilko, and I. Weir-Jones (2009), Noise , the what , the where and the how to, in *Shiraz 2009 - First International Petroleum Conference & Exhibition*. 3.1

Zhebel, O., D. Gajewski, and C. Vanelle (2011), Localization of seismic events in 3d media by diffraction stacking, in *73rd EAGE Conference & Exhibition*. 3.3.3

Chapter 4

Seismic arrival enhancement through the use of noise whitening

Claire Birnie[1], Kit Chambers [2], and Doug Angus [1,a]

[1] *School of Earth and Environment, University of Leeds, United Kingdom*

[2] *Nanometrics Inc., United Kingdom*

[a] *now at ESG Solutions, Canada*

This chapter is an adaptation of the paper:
Birnie, C., Chambers, K. and Angus, D., 2017. Seismic arrival enhancement through the use of noise whitening. *Physics of the Earth and Planetary Interiors*, 262, pp.80-89. doi:10.1016/j.pepi.2016.11.006

The following adaptations have been made to the submitted version:

1. Figure 4.3 has been edited and enlarged to allow easier identification of receivers and wells.

Abstract

A constant feature in seismic data, noise is particularly troublesome for passive seismic monitoring where noise commonly masks microseismic events. We propose a statistics-driven noise suppression technique that whitens the noise through the calculation and removal of the noise's covariance. Noise whitening is shown to reduce the noise energy by a factor of 3.5 resulting in microseismic events being observed and imaged at lower signal to noise ratios than originally possible - whilst having negligible effect on the seismic wavelet. The procedure is shown to be highly resistant to most changes in the noise properties and has the flexibility of being used as a stand-alone technique or as a first step before standard random noise attenuation methods.

4.1 Introduction

Noise is an ever present obstacle in all seismic data recordings, often preventing the user from extracting the desired signal. As such, noise suppression is one of the main topics of interest across all seismic monitoring scenarios ranging from reflection seismics (*Yilmaz*, 2001) to surface wave tomography (*Bensen et al.*, 2007). In this paper we use the example of a surface microseismic monitoring scenario to introduce a noise suppression technique applicable to all seismic monitoring scenarios.

In surface passive seismic monitoring arrivals are often at or below the noise level of individual recordings. As such noise suppression is of particular importance for monitoring of microseismic events. These events are observed in a variety of scenarios such as volcanic settings, earthquake hazard monitoring, assessing risk and containment in geo-industrial applications including geological storage of nuclear waste and carbon dioxide (CO_2), and monitoring of petroleum and mining procedures (*Gambino et al.*, 2004, *Schorlemmer and Wiemer*, 2005, *Maxwell*, 2011, *Oye et al.*, 2013). In general Signal to Noise Ratio (SNR) is maximised during the aquisition phase through survey design (*Maxwell*, 2010, *Auger et al.*, 2013, *Staněk et al.*, 2014). However a small number of noise suppression methods have been proposed for post aquisition, such as the application of multichannel Wiener filters (*Wang et al.*, 2008), the use of matched filters to identify smaller events from a parent event (*Eisner et al.*, 2008) and separating the seismic event from noise in the $\tau - p$ domain (*Forghani-Arani et al.*, 2012).

The issue with noise suppression methods is preserving the seismic signal properties when the event is often invisible under the noise. *Birnie et al.* (2016) showed that realistic noise models can be built from a knowledge of the noise's covariance matrix. This work aims to reduce recorded noise to White, Gaussian Noise (WGN) by removing the covariance of the noise. The process of removing the covariance from a dataset is

commonly referred to as noise whitening and is a well established procedure in many aspects of signal processing (*Hom and Johnson*, 1985, *Belouchrani et al.*, 1997, *Kessy et al.*, 2015). In this paper the noise whitening procedure is tested on both recorded noise, noise free synthetic waveform data and semi-synthetic datasets (datasets where recorded noise has been imposed on top of synthetic waveform data). To analyse the impact of the noise whitening, diffraction stack imaging, similar to that used by *Zhebel et al.* (2011), is performed on the semi-synthetic data before and after noise whitening. Using the Aquistore carbon storage site as an example, this paper demonstrates that noise whitening of seismic data results in a SNR 5 times higher, through reduction of the spatio-temporal properties of noise, whilst having negligible effect on first arrivals.

4.2 Theory

Noise can be separated into two categories - ambient and source-generated. Source generated noise refers to any signal that originates due to the interaction of the wavefield from the seismic source with heterogeneous earth structures (examples include ground roll and internal multiples). While the term ambient is used here to describe all noise signals independent of the seismic event, for example meteorological noise, production noise and teleseismic events. This study focusses on ambient noise, sometimes also referred to as background noise. The majority of ambient noise signals are not consistent in either space or time, further complicating noise suppression procedures. For example, passing traffic is a common source of noise with infrequent occurrences and receivers closest to the noise source most affected (*Nørmark*, 2011a). In a similar manner a significant drop in noise levels is observed with increasing distance from an active injection platform (*Schilke et al.*, 2014). For non-cultural noise, *Nørmark* (2011b) identified varying noise levels across the array from meteorological sources dependent on vegetation, wind speed and precipitation levels. These noise studies prove that noise is correlated in space and/or time therefore an efficient noise removal procedure must account for spatio-temporal variations of the noise field. The modelling method proposed by *Birnie et al.* (2016), based on covariance modelling (*Massart et al.*, 1988, *Scharf*, 1991), accounts for these spatio-temporal variations by generating multivariate Gaussian distributions whose defining statistics are derived to be identical to that of the observed noise. A single-variate Gaussian distribution is uniquely described by a single mean and standard deviation while a multi-variate Gaussian distribution is described by its mean vector and the lower triangular part of the Cholesky decomposition of it's covariance matrix. In this section we describe how to estimate the covariance from recorded data and subsequently remove the covariance from a recorded time series.

To compute the covariance matrix the seismic recording is split into multiple realisations, where a realisation is a time segment of the data. Following the first five steps of

the noise modelling procedure (*Birnie et al.*, 2016), the realisations are reshaped into column vectors, $\boldsymbol{d}_i$, and the sample mean for each time-space point is removed (i.e. $\hat{\boldsymbol{d}} = \boldsymbol{d} - \boldsymbol{\mu}$). The covariance, $\boldsymbol{C}$, is computed using

$$\boldsymbol{C} = \hat{\boldsymbol{D}}\hat{\boldsymbol{D}}^T/K, \tag{4.1}$$

where $\hat{\boldsymbol{D}} = [\hat{\boldsymbol{d}}_1\ \hat{\boldsymbol{d}}_2\ \ldots\ \hat{\boldsymbol{d}}_{K-1}\ \hat{\boldsymbol{d}}_K]$, $\hat{\boldsymbol{D}}^T$ is the transpose of $\hat{\boldsymbol{D}}$ and K is the number of realisations. The covariance matrix is then decomposed into its upper and lower triangular matrices using a Cholesky decomposition,

$$\boldsymbol{C} = \boldsymbol{C}^{1/2}(\boldsymbol{C}^{1/2})^T, \tag{4.2}$$

where $\boldsymbol{C}^{1/2}$ is the lower triangular matrix. To whiten the noise, the inverse of the lower triangular matrix is multiplied by a realisation of recorded data, $\boldsymbol{x}$, and scaled by α, the average of the diagonal elements of $\boldsymbol{C}$,

$$\tilde{\boldsymbol{x}} = \frac{\boldsymbol{C}^{-1/2}\boldsymbol{x}}{\alpha}, \tag{4.3}$$

to return the data to having an identity covariance matrix. To get an accurate estimate of the data's covariance matrix, realisations should have similar statistical properties.

The underlying principle behind the noise whitening procedure is that the noise in the data sample, $\boldsymbol{x}$, can be effectively represented by the covariance matrix, $\boldsymbol{C}$, and will be transformed into a random sequence (for example *Hom and Johnson*, 1985, *Belouchrani et al.*, 1997, *Kessy et al.*, 2015). However, the signals in $\boldsymbol{x}$ we wish to preserve will be invariants of $\boldsymbol{C}^{1/2}$ and hence be preserved.

4.3 Methodology

The removal of the covariance has to be performed over the same time length as that of the realisations used to compute it. However recordings last significantly longer than the realisation lengths therefore, for practical purposes, we would require to attenuate noise over much longer periods. We approach this problem in two ways - the first is to separate the data for noise whitening into the realisation length, perform the noise whitening on each data realisation and concatenate the data segments back together. We refer to this as independent patch whitening. The second approach is to overlap the data realisations for noise whitening and then use a Hanning window to taper the patches for the concatenation.

The independent patch whitening procedure (referred to as IPW hereafter) forms the basis methodology for the paper and the two extension procedures discussed in this

paper - rolling noise whitening procedure (referred to as RNW hereafter) and a rolling covariance whitening procedure (referred to as RCW hereafter). The steps for IPW are given in figure 4.1.

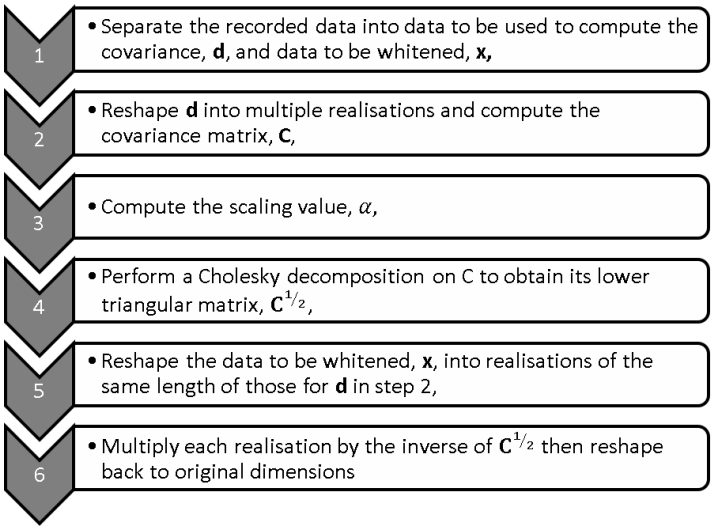

Figure 4.1: *Workflow of Independent Patch Whitening method.*

RNW is an extension of IPW by overlapping noise realisations in steps 5 and 6. This is done by extending the realisation length for both $\boldsymbol{d}$ and $\boldsymbol{x}$ in steps 2 and 5 and allowing realisations to overlap at the start and end of each patch. In step 6 when the whitened data is reshaped back to the original dimensions this is done using a Hanning window taper as illustrated in figure 4.2.

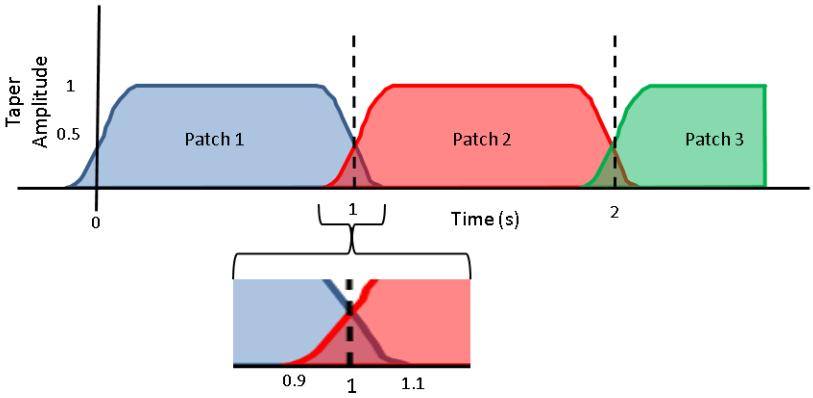

Figure 4.2: *Schematic of taper filters used for rolling noise whitening.*

The final extension to the whitening procedure incorporates a rolling covariance calculation into the RNW procedure, resulting in the RCW procedure. This involves reassigning $\boldsymbol{d}$ at predetermined points in $\boldsymbol{x}$ to be the data directly preceeding that point in $\boldsymbol{x}$. Then steps 2-4 are repeated on the updated data $\boldsymbol{d}$ prior to continuing with

the rolling noise whitening.

In this study we have used 3.5 minutes of noise recording to compute the covariance and 1s realisation lengths for the IPW, in accordance with the size and number of realisations used to compute the covariance matrix in the modelling method of (*Birnie et al.*, 2016). For RNW and RCW a realisation length of 1.2s is used, allowing a 0.1s 'buffer' either side of the realisation. Therefore, the taper transitions are 0.2s in length.

4.4 Data

The noise data utilised in this study comes from a permanent surface array installed at the Aquistore carbon dioxide (CO_2) storage site, located in South Saskatchewan, Canada in the northern part of the Williston Basin (*Roach et al.*, 2015). The array consists of 51 buried, vertical component geophones with a cross-shaped geometry as illustrated in figure 4.3. The geophones are 10Hz instruments buried at a depth of 20m with a sampling frequency of 500Hz. The noise is extracted from an hour recording beginning at 14:00 local time on 7 August 2012 and includes stationary noise signals observed constantly across the full recording, non-stationary noise signals rarely observed and pseudo-non-stationary noise signals observed for the majority of the recording however not constantly (for detailed explanation refer to *Birnie et al.* (2016)). Examples of the noise used are given in figure 4.4, where heightened noise levels are observed around the centre of the array.

Synthetic waveform data have been used in this study to identify the effect the noise balancing procedure has on signals from microseismic events. The waveform data is generated using E3D (*Larsen and Harris*, 1993). The source is placed below the middle of the N-S/E-W cross-shaped array at a depth of 1.6km, where the subsurface is modelled as a 16-layer, laterally homogeneous, isotropic medium with properties as described by *Roach et al.* (2015). A point source with a central frequency of 30Hz has been used to remove any requirement for polarity correction during the imaging of the event. The synthetic waveform data is used independently as well as combined with the recorded noise to make semi-synthetic datasets. When creating semi-synthetic data the SNR is determined by the ratio of the maximum amplitudes of the noise and waveform data.

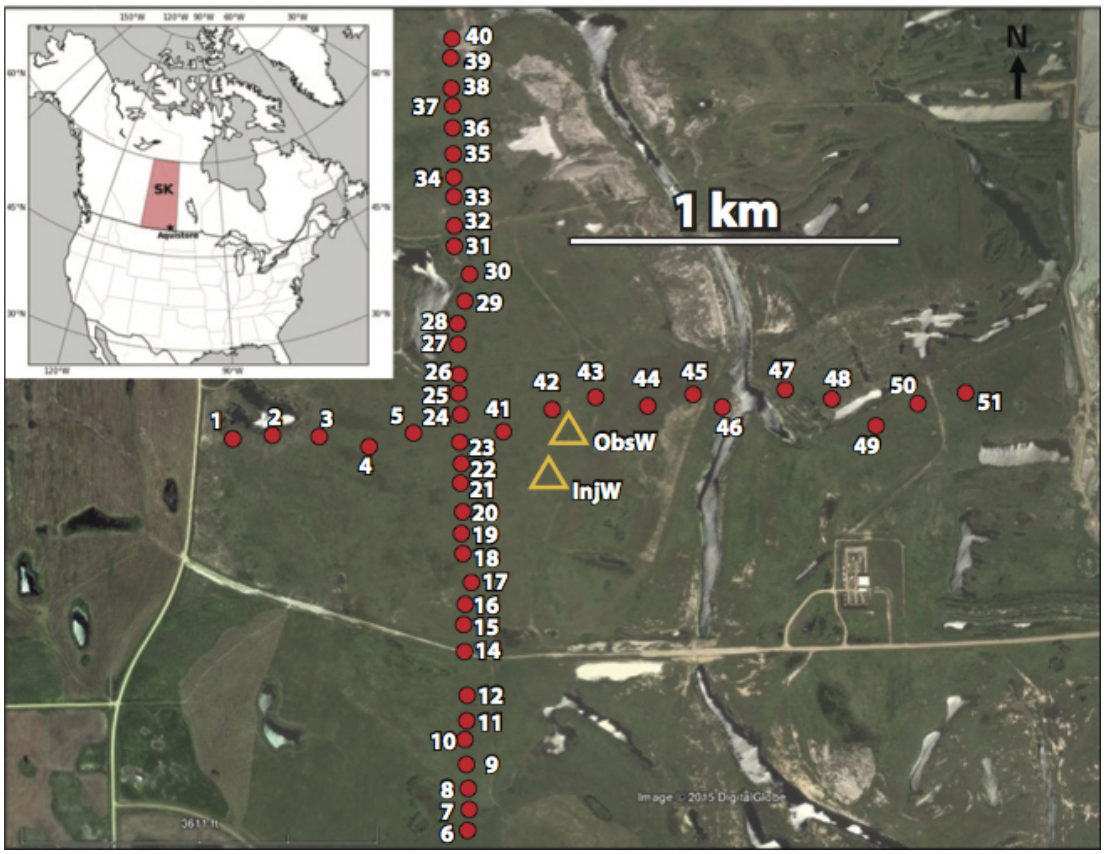

Figure 4.3: *Aquistore permanent seismic array survey geometry. Geophones are denoted by red dots alongside the station number, while the observation and injection wells are illustrated by yellow triangles.*

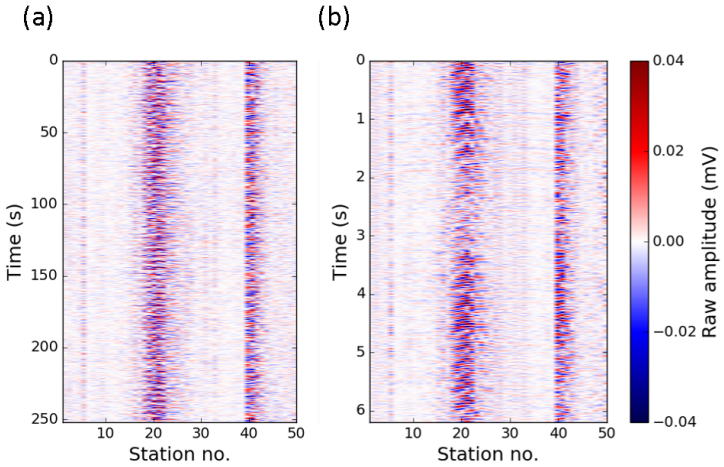

Figure 4.4: *(a) Noise data for computing covariance matrix and (b) noise data to be whitened.*

4.5 Results

4.5.1 Noise whitening

The noise data used to compute the covariance matrix and the noise to be whitened are shown in figures 4.4a and b, respectively. Figures 4.5a and b illustrate the results from IPW where the data to be whitened have been split into 1s realisations prior to removal of the covariance. We see that the noise energy has been successfully distributed across the receiver array by the whitening procedure. As detailed in table 4.1, the total energy across the array has decreased by 65% with the noisiest station (i.e. station 41) experiencing an energy decrease of 89% and the quietest station still experiencing an energy decrease by 15%. A noteable feature of figure 4.5b is the significant edge effects which occur at the beginning of each patch in the denoised data (shown as black arrows in the figure). Due to these effects the change in noise levels is calculated from 0.2s in the data window.

Figure 4.5c and d illustrate the results from RNW. While the patch transitions still occur at the same location, the tapering procedure has removed all noticeable edge effects. To provide direct comparison with the IPW, the second row of table 4.1 is the sum of energy from $0.2 - 1$s while the final row is the sum of energy for the full 6s of data. As with IPW, RNW successfully distributes the energy across the array decreasing the total noise level of the 6s of data by 84%. The noise energy at station 41 decreased by 90% while station 50 decreased by 13%. Changes in the values by which the noise decreases between IPW and RNW can be attributed to them using different lengths of realisations in the computation of the covariance matrix. Due to

Table 4.1: *Change in noise energy before and after noise whitening for a noise station (Station 41), a quiet station (Station 50) and the full array. To minimise the influence of the edge effect, the first two rows are calculated from* $0.2 - 1s$*. The final row is calculated for full 6s of whitened data.*

		Total energy		
		Station 41	**Station 50**	**Full array**
Individual patch whitening (0.8s)	**Before**	0.0682	0.0071	0.7721
	After	0.0076	0.0060	0.0942
	%Change	89	15	65
Rolling noise whitening (0.8s)	**Before**	0.0682	0.0071	0.7721
	After	0.0097	0.0051	0.1138
	%Change	86	28	62
Rolling noise whitening (6s)	**Before**	0.5769	0.0464	4.7236
	After	0.0553	0.0405	0.7405
	%Change	90	13	84

the suppression of the edge effect, RNW is the better of the two techniques.

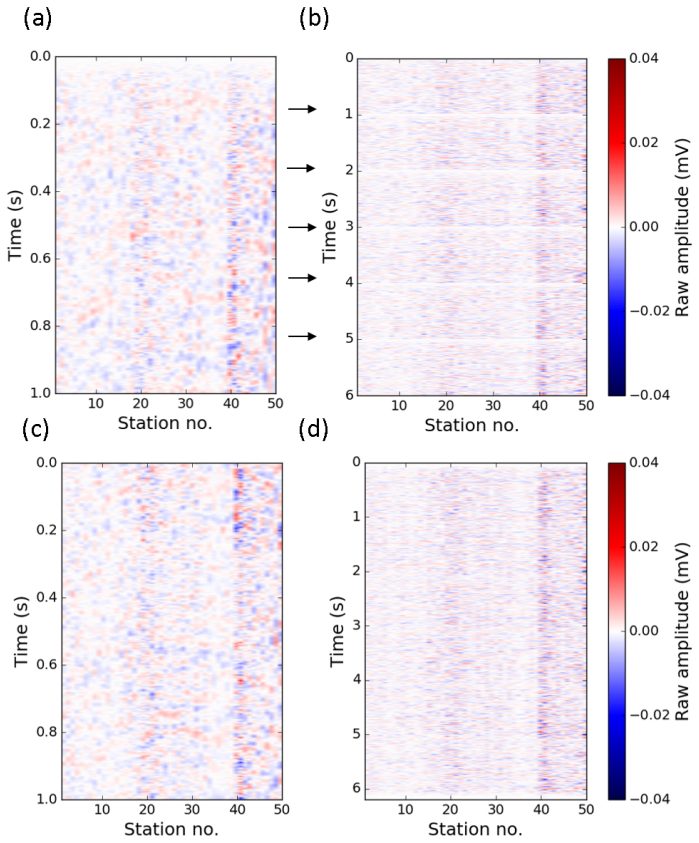

Figure 4.5: *Whitened noise data, (a) and (b) using independent patch method, IPW, (c) and (d) using rolling noise method, RNW. (a) and (c) are 1s segments of the 6s of whitened data (b) and (d). Black arrows indicate edge effect from IPW.*

The power spectrum of station 41 prior to whitening and after RNW is given in figure 4.6. While there are not equal amounts of power in each frequency band, the power spectrum for the whitened data is significantly flatter with less energy in the lower frequencies and more in the higher frequencies than that of the noise prior to whitening.

4.5.2 Effect on arrival observations

To analyse the effect of noise whitening on a signal from a microseismic event RNW was performed on a semi-synthetic dataset and on noise-free synthetic waveform data, illustrated in figure 4.7. The noise used to create the semi-synthetic dataset is the same as the noise whitened in the previous section. In the semi-synthetic case we see that the arrival is clearly retrieved by the denoising procedure, and the residual/noise section is overwhelmingly dominated by the removed noise. Due to the long period nature of the noise, the whitening process has acted similar to that of a high pass filter on some traces however it has done so automatically and with reference to the phase spectrum

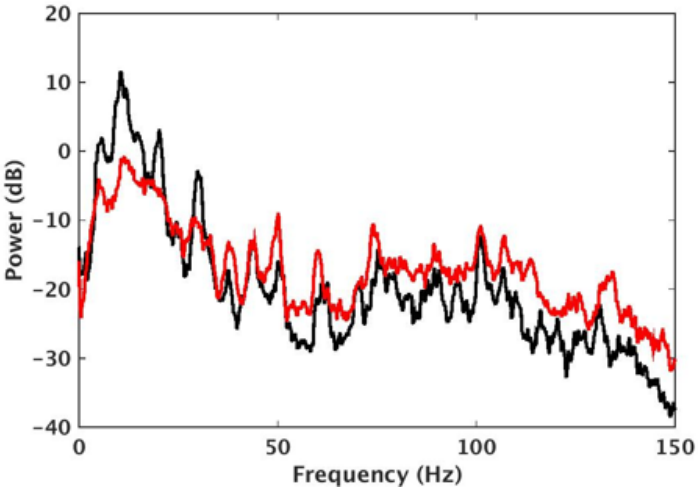

Figure 4.6: *Power spectrum of noise data at station 41 before (black) and after (red) whitening.*

as well as the amplitude spectrum of the noise. In the noise free synthetic application (figure 4.7d/e/f) we see that some of the arrival energy is attenuated by the denoising process. However, this is a negligible proportion of the amplitude that we believe is due to the small amount of regularisation added. Figure 4.8 shows the change in power spectrum and phase of station 41 for the first arrival ($0 < t < 0.4$s) of the noise-free data before and after whitening. We find that between frequencies 10 to 70Hz there is close match in both energy content and phase of the first arrival. It should be noted that the input wavelet is a 30Hz Ricker wavelet and therefore has a very limited amount of energy outside the 10-70Hz range (note the log scale in figure 4.8).

Diffraction stack imaging was performed on the semi-synthetic data prior to and after whitening to identify the benefits whitening has on event location determination. Figure 4.9 shows that at a SNR of 0.04 the image maxima for the original data is an artefact arising from the noise in the dataset. However when noise whitening has been applied these artefacts are significantly reduced resulting in the image maxima correctly locating the seismic event. At a SNR of 0.08 both the original data and whitened data have a maxima at the seismic source location however there is still significant energy from the noise creating artefacts in the image while there are no noise artefacts in the whitened data image.

4.5.3 Robustness tests

As discussed in detail by *Birnie et al.* (2016), to get a usable covariance matrix for modelling it is required that the realisations used to create the covariance have the same statistical properties. The following results are to test the extent to which this holds for the noise whitening case, i.e. to test the extent to which the noise can vary

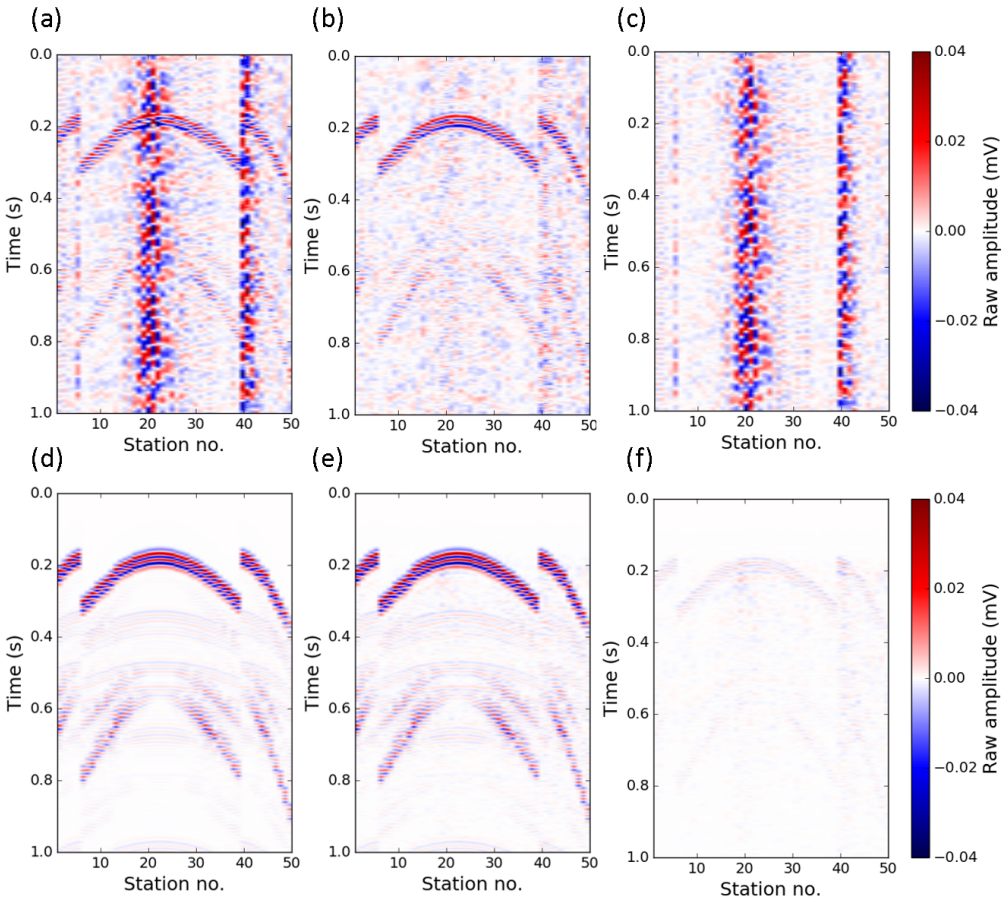

Figure 4.7: *Semi-synthetic (a) before and (b) after whitening and (c) the difference between the two, and a noise-free event (d) before and (e) after whitening and (f) the difference between the two.*

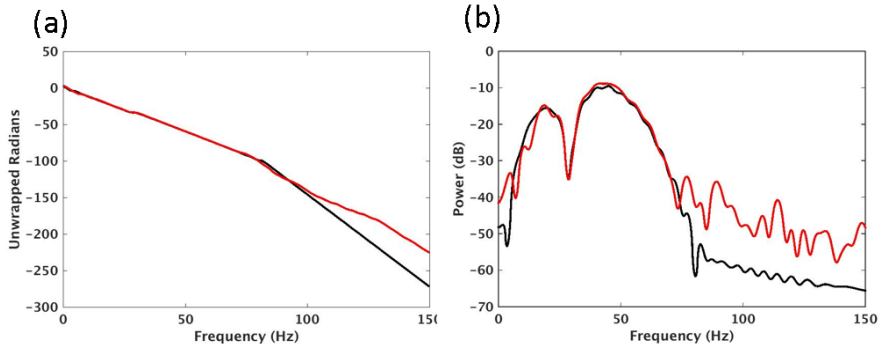

Figure 4.8: *(a) Phase and (b) power spectra of first arrival at station 41 from noise-free event before (black) and after (red) whitening. Note the logarithmic scale used in (b).*

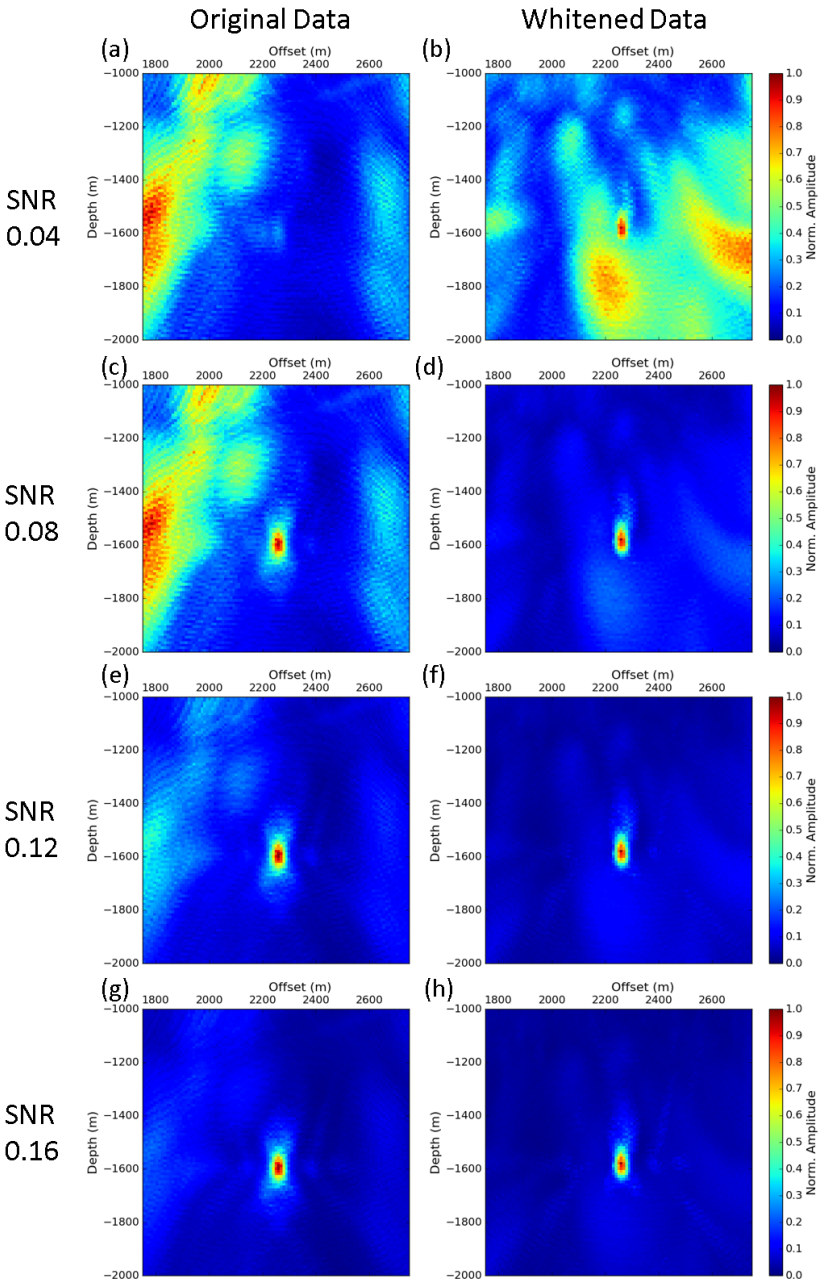

Figure 4.9: *Diffraction stack imaging of microseismic event at 1.6km depth and 2260m offset for SNR of semi-synthetic datasets before (first column) and after whitening (second column) at increasing SNRs.*

within both the dataset for computing the covariance and for whitening. The first scenario tested, Scenario 1, has a change in noise type at approximately 3s into the data from a regime consistent with the data used to estimate the covarience matrix to one where a dominant source of noise for several traces is absent (top row of Figure 4.10). Despite a very minor increase in the whitened noise level at the transition

between the two noise signals, the noise whitening procedure is successful, reducing the noise by 84% (table 4.2). Scenario 2, the second row of Figure 4.10, considers where the data used to construct the covariance matrix contains examples of the desired signals. In this case we use a swarm of 20 microseismic events, alongside a change in noise type. The whitened data appears unaffected by the signals or the changing noise types.

Table 4.2: *Change in noise energy before and after whitening for multiple scenarios tested.*

		Total energy		
		Station 41	**Station 13**	**Full array**
Scenario 1	**Before**	0.1721	0.0023	1.8732
	After	0.0187	0.0021	0.3052
	%Change	89	9	84
Scenario 2	**Before**	0.1647	0.0032	1.6527
	After	0.0252	0.0022	0.2974
	%Change	85	31	82
Scenario 3	**Before**	0.1647	0.0032	1.6527
	After	0.0204	0.0084	0.3209
	%Change	88	163 (Inc.)	81
Scenario 4	**Before**	0.1389	1.9229	3.8383
	After	0.0377	2.1322	2.9425
	%Change	73	10 (Inc.)	23

The final two scenarios utilise a high amplitude noise burst resulting from a passing car. In scenario 3, the car energy is placed in the data used to compute the covariance (third row of Figure 4.10). Visually the results show that the high energy noise burst has little to no effect on the whitening procedure: however the energy at station 13 has increased by 163% showing that the whitening does not perform as well on the stations affected by the noise burst. In scenario 4, the car energy is placed in the data to be whitened. Note that as the duration of the burst is longer than the duration of the traces in figures 4.10k and l it appears as a vertical stripe on traces $11 - 15$. The background noise has been whitened with station 41 experiencing a reduction in noise energy by 73% yet the high-energy noise due to the car has not been suppressed.

4.5.4 Extension: Rolling covariance calculation

An extension to the noise whitening procedure is RCW where the covariance matrix is updated/recomputed using a rolling window of 3.5 minutes of data prior to the data sample to be denoised. Ten minutes of data have been whitened with the covariance matrix being recalculated every 5s. Due to the size of each covariance matrix it is not possible to save them and compare the differences for every 5s therefore an event has been added at $\sim$ 2.5s into each patch and the SNR is calculated before and after whitening. Figure 4.11a shows the SNR of each 5s patch after whitening and compares

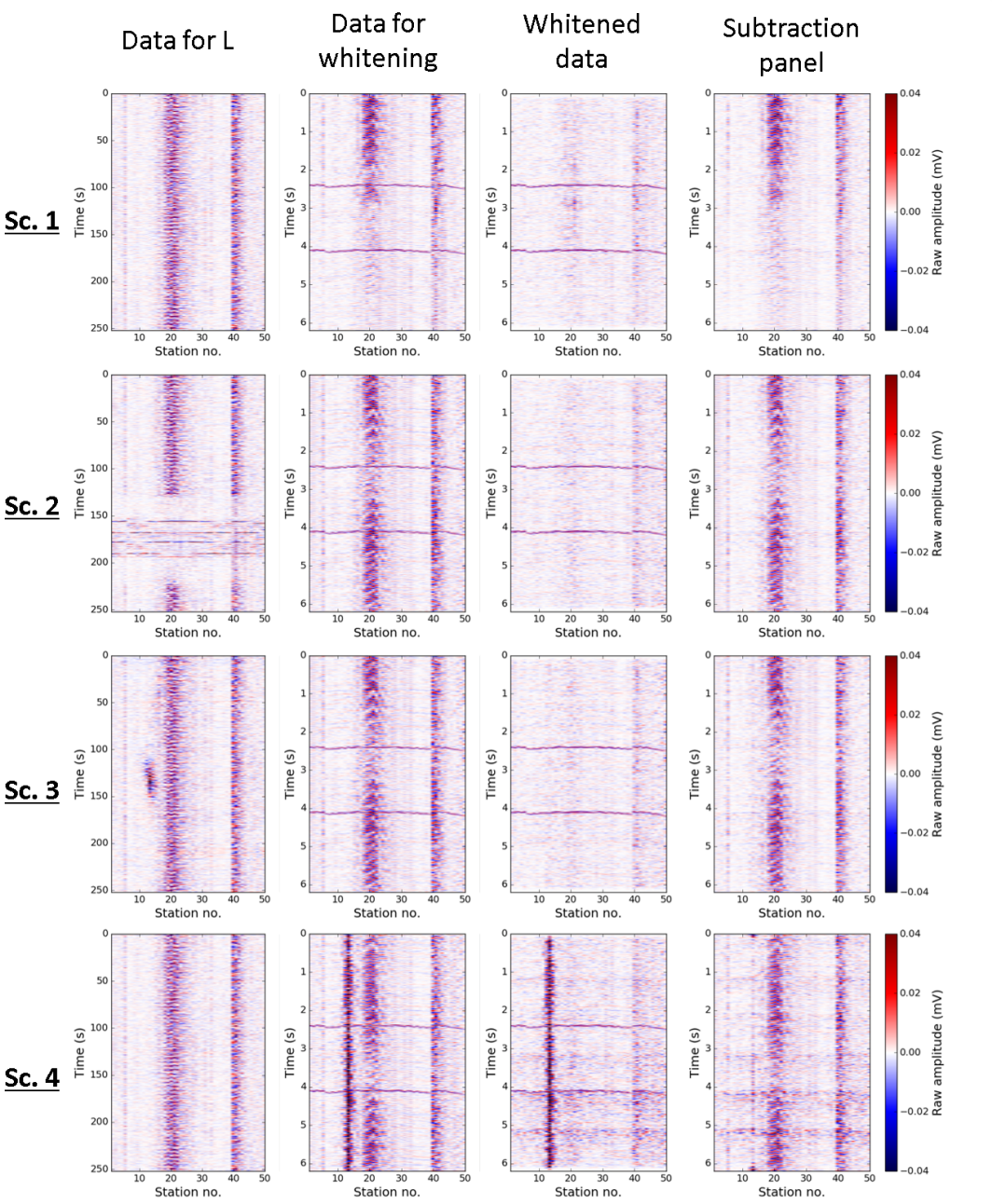

Figure 4.10: *Robustness tests. Scenario 1 involves a change in noise properties in data for whitening; Scenario 2 involves a change in noise and swarm of 20 events in data used to compute L; Scenario 3 involves a high-energy noise burst in data used to compute L; and, scenario 4 involves a high-energy noise burst in data for whitening. The first column is data to compute the covariance, the second is data to be whitened, the third is whitened data and the fourth column is the difference between the second and third.*

it with the difference for the case where a single covariance was used for whitening the full 10minutes (i.e. RNW case), while figure 4.11b shows the change in SNR after whitening for both RNW and RCW. The RNW and RCW perform very similarly, with both techniques struggling with high energy noise at approximately 3.25 and 8.6

minutes similar to the noise observed in robustness scenarios 3 and 4, and neither significantly outperform the other in increasing the SNR through whitening.

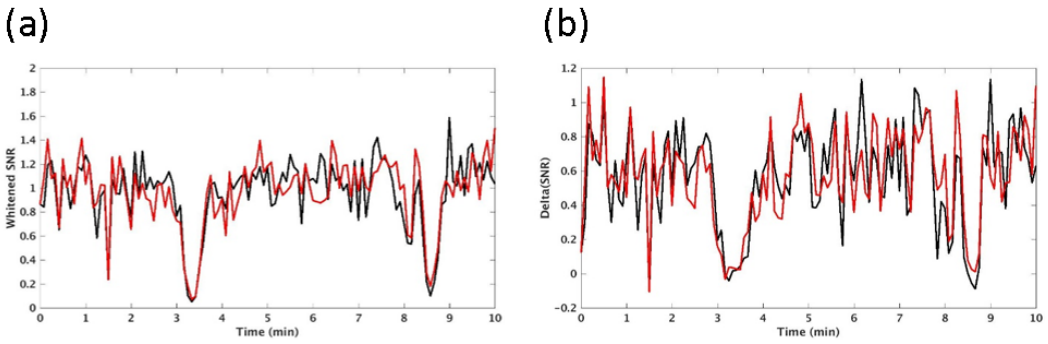

Figure 4.11: *(a) Comparison of SNR of 5s data patches after whitening for RNW (black line) and RCW (red line), where the covariance matrix is recomputed every 5s, and (b) change in SNR (i.e. delta(SNR)) before and after whitening, where negative delta corresponds to an increase in SNR after whitening.*

4.6 Discussion

In essence, noise whitening has been shown to increase SNR by randomisation of the noise. Comparing the mean noise energy of 1s on stations 1 and 41 (i.e. a 'quiet' and 'noisy' station), prior to whitening station 41 is ~ 5 times noiser than station 1, while after whitening that is reduced to ~ 3 times. Whilst the noise has been whitened it has also been reduced in amplitude with station 1 experiencing a decrease of $\sim 50\%$ and station 41 experiencing a decrease of $\sim 71\%$. While there are still observable changes in the noise levels across the array, they have been significantly reduced through whitening.

The majority of noise suppression techniques are directed approaches in which noise with a particular property is removed. For example, suppressing noise with a linear moveout (e.g. *Forghani-Arani*, 2013) or suppressing noise with a particular slowness (e.g. *Roux et al.*, 2014, *Dando et al.*, 2016). As these techniques are based on exploiting a property of the noise they therefore require knowledge of the noise's properties to effectively suppress it. The technique proposed in this paper is an example of an undirected approach which makes no assumptions on the noise's origin or the form it takes within the data. An example of another undirected approach is that of *Blunda* (2013) whose combination of time-frequency winsorisation and adaptive subtraction procedures result in a modest SNR gain of 4-12 dB.

Not only does the noise whitening technique make no assumptions on the noise but it has been shown to provide a clean separation between signal and noise even when

signals are present within the data used to compute the covariance matrix. In general, the signals of interest are very short in duration and few in number relative to the noise. Therefore when the covariance is computed the signals are averaged out by the noise resulting in a covariance matrix that models the noise with very little contribution from the signals. Provided the seismic arrivals are invariants of the covariance matrix then they are unaffected by the whitening procedure.

Whitening the data resulted in better imaging of lower SNRs without any additional processing. A benefit of this procedure is that once the covariance has been computed, the incoming data can be processed in real time, with each new patch recorded being whitened prior to the use of automated detection and location procedures. The results from the robustness tests showed that the noise whitening procedure continues to work effectively where there are significant noise variations between patches used to compute the covariance matrix, i.e. scenarios 2 and 3, as well as where there are noise variations within the data for whitening, scenario 1. However, from experience it is worth noting that to ensure the covariance represents the dominant noise signal then it should be present in approximately 50% of the patches. Our results also show that the high contrast between the base noise signal and the passing car in the final scenario results in the car noise not being whitened. For single high-energy bursts that affect a small number of receivers there are alternative methods for noise suppression, such as despiking in the time-frequency domain, which we would encourage to be used after noise whitening to remove such signals that cannot be suppressed during whitening. When combining the noise whitening procedure with diffraction stack imaging, events were detected at SNR 50% lower than without noise whitening, highlighting the benefits of performing noise whitening prior to random noise attenuation techniques.

The last section of the results focusses on extending the technique to include a rolling covariance calculation from the 3.5 minutes of data directly preceding the data for whitening. If a site experiences significantly changing noise, with respect to time, then the recalculation of the covariance may be worthwhile. However, in this case the noise was deemed sufficiently stable to provide any benefits from continually updating the covariance matrix. Other extensions to this study could include computing a covariance matrix of a single noise type and using that to whiten only that noise type.

On a concluding note, while this paper has focussed on the application to surface microseismic this technique is applicable to any time series recording where noise can be considered as a multivariate Gaussian distribution. Future studies should focus on the benefits this technique can bring to other exploration, global and hazard monitoring applications.

4.7 Conclusions

In this study we have shown that noise whitening provides a robust method for increasing SNR in surface seismic data. Applicable in any situation with one or more receivers, this method has the ability to be used after data has been collected or continually on new data as it is being recorded, and as a pre-cursor to random noise attenuation procedures or as a stand-alone method. Noise whitening has a negligible effect on a seismic wavelet whilst significantly reducing noise energy resulting in improved event detection and imaging at lower SNR than originally possible. For the microseismic monitoring scenario, the ability to push the imaging capabilities to significantly lower SNR will allow improved characterisation of fracture systems, due to the higher number of low energy events in comparison to the lower number of high energy events (*Gutenberg and Richter*, 1944). The technique performs exceptionally well in robustness tests on data experiencing varying noise properties, reducing the noise energy by at least 23% even when there are noise signals present that are not whitened, such as spurious high energy bursts. In this paper we have demonstrated that noise whitening is a powerful and flexible noise attenuation method, and as such is a valuable addition to the geophysicists' toolbox.

Acknowledgements

The authors would like to thank Frans Kets for valuable discussions during this study. We would like to thank the Petroleum Technology Research Centre (PTRC) for access to Aquistore Data. Aquistore an independent research and monitoring project managed by the PTRC which intends to demonstrate that storing liquid carbon dioxide deep underground (in a brine and sandstone water formation), is a safe, workable solution to reduce greenhouse gases. C. Birnie is funded by the NERC Open CASE studentship NE/L009226/1 and Pinnacle-Halliburton. D. Angus acknowledges the Research Council UK (EP/K035878/1; EP/K021869/1; NE/L000423/1) for financial support.

References

Auger, E., E. Schisselé-Rebel, and J. Jia (2013), Suppressing noise while preserving signal for surface microseismic monitoring: The case for the patch design, in *2013 SEG Annual Meeting*, Society of Exploration Geophysicists. 4.1

Belouchrani, A., K. Abed-Meraim, J.-F. Cardoso, and E. Moulines (1997), A blind source separation technique using second-order statistics, *IEEE Transactions on signal processing*, *45*(2), 434–444. 4.1, 4.2

Bensen, G., M. Ritzwoller, M. Barmin, A. Levshin, F. Lin, M. Moschetti, N. Shapiro, and Y. Yang (2007), Processing seismic ambient noise data to obtain reliable broad-band surface wave dispersion measurements, *Geophysical Journal International*, *169*(3), 1239–1260. 4.1

Birnie, C., K. Chambers, D. Angus, and A. Stork (2016), Analysis and models of pre-injection surface seismic array noise recorded at the aquistore carbon storage site, *Geophysical Journal International*. 4.1, 4.2, 4.3, 4.4, 4.5.3

Blunda, C. K., Y. (2013), A generic procedure for noise suppression in microseismic data., in *CSPG/CSEF/CWLS Geo Convention*. 4.6

Dando, B., K. Iranpour, V. Oye, S. Bussat, and L. Bjerrum (2016), Real-time microseismic monitoring in the north sea with advanced noise removal methods, in *SEG Technical Program Expanded Abstracts 2016*, pp. 2657–2661, Society of Exploration Geophysicists. 4.6

Eisner, L., D. Abbott, W. B. Barker, M. P. Thornton, and J. Lakings (2008), Noise suppression for detection and location of microseismic events using a matched filter, in *2008 SEG Annual Meeting*, Society of Exploration Geophysicists. 4.1

Forghani-Arani, F. (2013), Analysis and suppression of passive noise in surface microseismic data, Ph.D. thesis, Colorado School of Mines. 4.6

Forghani-Arani, F., M. Batzle, J. Behura, M. Willis, S. S. Haines, and M. Davidson (2012), Noise suppression in surface microseismic data, *The Leading Edge*, *31*(1496–1501), 1496–1501. 4.1

Gambino, S., A. Mostaccio, D. Patanè, L. Scarfì, and A. Ursino (2004), High-precision locations of the microseismicity preceding the 2002–2003 mt. etna eruption, *Geophysical research letters*, *31*(18). 4.1

Gutenberg, B., and C. F. Richter (1944), Frequency of earthquakes in california, *Bulletin of the Seismological Society of America*, *34*(4), 185–188. 4.7

Hom, R. A., and C. R. Johnson (1985), *Matrix analysis*, Cambridge University Express. 4.1, 4.2

Kessy, A., A. Lewin, and K. Strimmer (2015), Optimal whitening and decorrelation, *eprint arXiv:1512.00809*. 4.1, 4.2

Larsen, S., and D. Harris (1993), Seismic wave propagation through a low-velocity nuclear rubble zone, *Tech. rep.*, Lawrence Livermore National Lab., CA (United States). 4.4

Massart, D. L., B. Vandeginste, S. Deming, Y. Michotte, and L. Kaufman (1988), *Chemometrics: a textbook*, Elsevier Amsterdam. 4.2

Maxwell, S. (2010), Microseismic: Growth born from success, *The Leading Edge*, *29*(3), 338–343. 4.1

Maxwell, S. (2011), Microseismic hydraulic fracture imaging: The path toward optimizing shale gas production, *The Leading Edge*, *30*(3), 340–346. 4.1

Nørmark, E. (2011a), Suppression of traffic noise on vibroseismic data, in *Near Surface 2011-the 17th European Meeting of Environmental and Engineering Geophysics*. 4.2

Nørmark, E. (2011b), Wind and rain induced noise on reflection seismic data, in *Near Surface 2011-the 17th European Meeting of Environmental and Engineering Geophysics*. 4.2

Oye, V., E. Aker, T. M. Daley, D. Kühn, B. Bohloli, and V. Korneev (2013), Microseismic monitoring and interpretation of injection data from the in salah co 2 storage site (krechba), algeria, *Energy Procedia*, *37*, 4191–4198. 4.1

Roach, L. A., D. J. White, and B. Roberts (2015), Assessment of 4d seismic repeatability and co2 detection limits using a sparse permanent land array at the aquistore co2 storage site, *Geophysics*, *80*(2). 4.4, 4.4

Roux, P.-F., J. Kostadinovic, T. Bardainne, E. Rebel, M. Chmiel, M. Van Parys, R. Macault, and L. Pignot (2014), Increasing the accuracy of microseismic monitoring using surface patch arrays and a novel processing approach, *first break*, *32*(7), 95–101. 4.6

Scharf, L. L. (1991), *Statistical signal processing*, vol. 98, Addison-Wesley Reading, MA. 4.2

Schilke, S., T. Probert, I. Bradford, A. Özbek, and J. Robertsson (2014), Use of surface seismic patches for hydraulic fracture monitoring, in *76th EAGE Conference and Exhibition 2014*. 4.2

Schorlemmer, D., and S. Wiemer (2005), Earth science: Microseismicity data forecast rupture area, *Nature*. 4.1

Staněk, F., L. Eisner, and T. Jan Moser (2014), Stability of source mechanisms inverted from p-wave amplitude microseismic monitoring data acquired at the surface, *Geophysical Prospecting*, *62*(3), 475–490. 4.1

Wang, J., F. Tilmann, R. White, H. Soosalu, and P. Bordoni (2008), Application of multichannel wiener filters to the suppression of ambient seismic noise in passive seismic arrays, *The Leading Edge*, *27*(2), 232–238. 4.1

Yilmaz, Ö. (2001), *Seismic data analysis*, vol. 1, Society of Exploration Geophysicists Tulsa. 4.1

Zhebel, O., D. Gajewski, and C. Vanelle (2011), Localization of seismic events in 3d media by diffraction stacking, in *73rd EAGE Conference & Exhibition*. 4.1

Chapter 5

Discussion and conclusions

For specific discussions and conclusions related to the different stand-alone publications, I refer the reader to the individual discussions and conclusions in Chapters 2 through 4. This chapter presents a brief discussion on recommendations for future research to improve the modelling and whitening procedures. This is followed by a concise (recipe-like) description on how to implement the modelling and whitening procedures along with a discussion on their potential uses outwith the land, surface microseismic monitoring scenario discussed in this thesis. The chapter is rounded up with a general conclusion of this thesis.

5.1 Discussion on future research

In Chapter 2 I devised a new family of methods for modelling of realistic seismic noise which rely on covariance-based modelling procedures and benchmarked against a number of approaches present in the literature. Table 5.1 provides a summary of the advantages and disadvantages of the different methodologies. While each method presents both advantages and disadvantages highlighting that, as yet, no technique is perfect, the proposed ICOVA-LPF modelling represents the most robust technique offering noise models that realistically imitate all noise signals ranging from sporadic traffic events to near-continuous injection noise. Future development of the modelling procedure could however reduce some of its own disadvantages which could benefit both the quality of the modelling and the related denoising technique proposed in Chapter 4.

One of the most severe restrictions of the ICOVA method is that the noise realisations are constrained to the same spatial geometry as the input data used to compute the noise statistics. Being able to interpolate such noise realisations (or their noise statistics) to a dense, regular geometry would allow the combination of noise collected on

Table 5.1: *Overview of the advantages and disadvantages of the noise modelling procedures discussed in this thesis.*

Model	Brief methodology	Advantages	Disadvantages	Reference
WGN	extract random samples from a standard normal distribution	1. No requirement of noise beforehand 2. Fast 3. Computationally cheap and easy to implement 4. No geometry restrictions	1. Little to no imitation of recorded noise	*O'Brien* (1974)
CONV	On a trace-by-trace basis, convolve recorded noise with a random Gaussian trace	1. Mimics frequency content of noise 2. Fast 3. Computationally cheap and easy to implement	1. Requires pre-recorded noise 2. Noise must be stationary 3. Trace-by-trace process removes coherency of noise 4. Restricted to geometry of recorded noise	*Pearce and Barley* (1977)
Distributed surface sources	Surface sources are propagated where source properties are randomly distributed	1. No requirement of noise beforehand 2. Similar characteristics to recorded noise 3. No geometry restrictions	1. Lack full complexity of noise generated by field conditions, e.g., geological, geographical, meteorological 2. Computationally expensive	*Sylvette et al.* (2006)
COVA	Generates a multi-variate Gaussian distribution based on the statistics of the recorded noise field	1. Mimics frequency content of noise 2. Similar characteristics to recorded noise	1. Requires pre-recorded noise 2. Restricted to geometry of recorded noise 3. Noise must be repetitive over modelling window length	*Birnie et al.* (2016)
ICOVA	Noise signals are separated prior to modelling individual signals with COVA methodology	1. Mimics properties of noise in frequency and time domain 2. Can combine different modelled signals to generate tailored noise models 3. Can model signals on full range of stationarity 4. Noise statistics can be saved in a database	1. Requires pre-recorded noise 2. Restricted to geometry of recorded noise 3. Requires noise signal separation prior to modelling 4. Requires adequate representation of noise signals to build statistics	*Birnie et al.* (2016)
ICOVA-LPF	Non-repetitive signals are modelled using a LPF while remaining signals are modelled with ICOVA methodology	1. All the benefits of ICOVA 2. incorporation of LPF allows modelling of less repetitive signals	1. Requires pre-recorded noise 2. Restricted to geometry of recorded noise 3. Requires noise signal separation prior to modelling	*Birnie et al.* (2016)
Semi-Synthetics [1]	Directly incorporate recorded noise into synthetic waveform data	1. Allows incorporation of realistic noise 2. Computationally cheap and easy to implement	1. Requires pre-recorded noise 2. Restricted to duration of recorded noise 3. Restricted to geometry of recorded noise 4. Cannot modify temporal and spatial characteristics of noise in a methodological manner	*Wang et al.* (2008)

[a] Although not strictly a modelling procedure, its frequent usage as an approach to include noise in synthetic datasets justifies its presence in this table.

different arrays and the testing of various array geometries. This would have great advantages for the noise whitening procedure for sites where acquisition geometries change over the monitoring duration, or as a method for handling inconsistent sensor activity (for example, dead traces).

Interpolation could be applied at 3 different stages of the procedure: prior to creating the noise statistics, on the noise statistics, or on the noise model. The first and third options would be performed on the wavefield data and could leverage from a variety of approaches specifically developed for interpolation of seismic data, e.g., trace interpolation in the F-X domain (*Spitz*, 1991) or in $\tau - p$ domain (*Kabir and Verschuur*, 1995). Alternatively, the second option would instead be interpolation of the noise statistics (i.e., mean and covariance).

At this stage I conjecture that the most computationally efficient approach would be to perform the interpolation on the noise statistics. Given that an unlimited number of models can be generated from a single set of statistics, it makes sense to perform the interpolation only once on the noise statistics as opposed to interpolating each time a new modelled noise patch is generated. Similarly, the noise statistics are typically generated from > 150 noise patches, therefore interpolation of the input data would be significantly more effort than interpolation of the noise statistics.

Furthermore, different approaches could be taken for the spatial interpolation required to move away from the original array geometry. For a fairly regular, reasonably dense array simple approaches such as nearest-neighbour interpolation or least-squares 2D splines could be utilised. However, for very sparse geometries, such as the Aquistore array discussed in this thesis, I envisage that statistical methods for spatial interpolation, such as Kriging (*Li and Heap*, 2008), may allow the extension of the noise modelling away from the current receiver locations. For example, as depicted in Figure 5.1, acting on subsets of the covariance matrix that refer to a single point in time, a new covariance at any spatial location of interest could be produced as a linear combination of the surrounding noise statistics.

The second disadvantage is the requirement of separating the different noise signals prior to modelling. Whilst this has been carried out in a manual fashion in this thesis, such a problem lends itself naturally to a machine learning approach. Provided the availability of a number of manually classified noise patches, this could become the training dataset for a supervised classification scheme speeding up the collection of the necessary number of noise patches required to determine the noise statistics. A noise classification scheme also has great potential for real-time noise suppression procedures allowing for targeted noise suppression procedures to be applied without manual detection of noises. This idea has initially been investigated as part of a recent collaboration with NORSAR and findings will be reported in the near future. Moreover, although

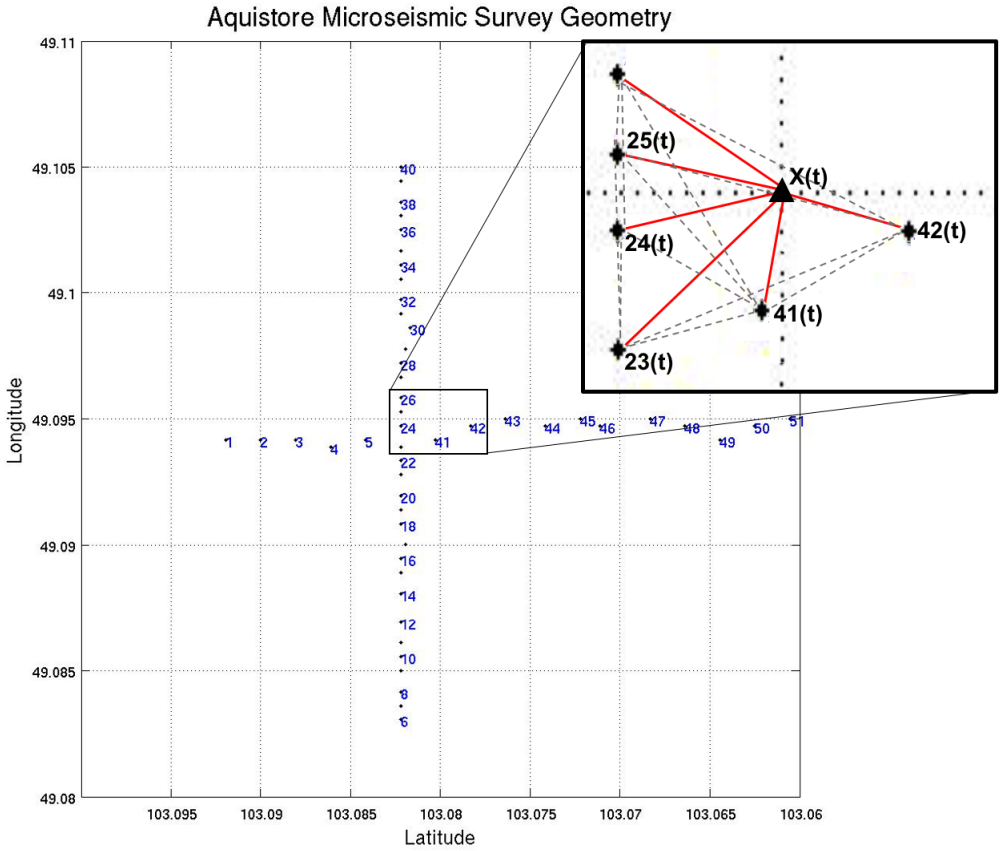

Figure 5.1: *Schematic representation of the suggested spatial interpolation approach for the Aquistore array. For each time sample t the corresponding values of the noise statistics at the available receivers can be used to estimate the kriging weights needed to estimate the sample $X(t)$ at the desired location. Dashed lines indicate the relationships between the available receivers while the solid lines indicate the relationship between the available receivers and desired location.*

more challenging as an initial selection procedure, unsupervised clustering techniques combined with manual review could provide an alternative approach to separating different noise signals without requiring manually classified patches. A study by *Galvis et al.* (2017) used k-means clustering to automatically detect and classify surface waves in seismic data while a study by *Huot et al.* (2017) performed classification of noise in seismic data using a combination of continuous wavelet transforms and hierarchical clustering. The success of these studies provides encouragement that this is an appropriate application to the problem of noise classification prior to applying the ICOVA modelling and whitening procedures.

Finally, as shown in Table 5.1, all modelling methods proposed in this thesis (i.e., COVA, ICOVA, and ICOVA-LPF) require recorded noise in order to compute the noise statistics and modelling parameters. At first this can be seen as a hurdle given the lim-

ited availability of open-source data and the often unwillingness of companies/institutes to share data (i.e., metadata). However, it is important to emphasise that my modelling and denoising procedures only require noise statistics. In other words, it is possible to perform modelling and denoising using only the noise statistics without sharing the data. This opens up the opportunity for an ever-growing, open-source database of noise statistics without any requirement of seismic data sharing.

5.2 A recipe for the implementation of noise modelling and whitening

In this section I provide a simple step-by-step recipe for the implementation of the ICOVA noise modelling and whitening approaches presented in this thesis. Note that while chapters 2 and 4 detail the modelling and whitening procedures, respectively, in great detail, this section focuses on a high level implementation of the procedure and aims to serve as guidelines on the use of these procedure on new datasets. Figure 5.2 illustrates the workflow from data collection through to the implementation of the modelling/whitening algorithms and beyond.

The first step is to identify and isolate the individual noise signals contained in the reference dataset and determine whether the ICOVA modelling or whitening procedures are appropriate for the identified noise signals, i.e., do they have adequate realisations of the noise signal with the same statistical properties. If noise is too infrequent or highly varying then a different approach should be considered. For example, for a random energy burst a linear prediction filter can be used for modelling (as illustrated in Chapter 2) or a despike filter may be used for suppression. As discussed above, I recommend that a noise classification algorithm is included in future as a substitute for the manual inputs currently required to identify and isolate noise signals within a dataset.

After isolating the noise signals, the data should be separated into noise patches and the covariance and mean can be computed as outlined in the equations 2.6 to 2.8. I recommend that these noise statistics are computed only once and stored to disk to avoid unnecessary re-computation during the subsequent modelling (or whitening) procedures. At this stage, I would also recommend saving an interpolated version of the statistics (generated for a denser array) to allow use of these noise signal models in studies where there is no previously collected data.

For modelling, the noise statistics can be used to generate an unlimited duration of modelled noise by iterating over equation 2.9 with different random base vectors, as shown in Chapter 2. Different noise models can be combined to create a dataset

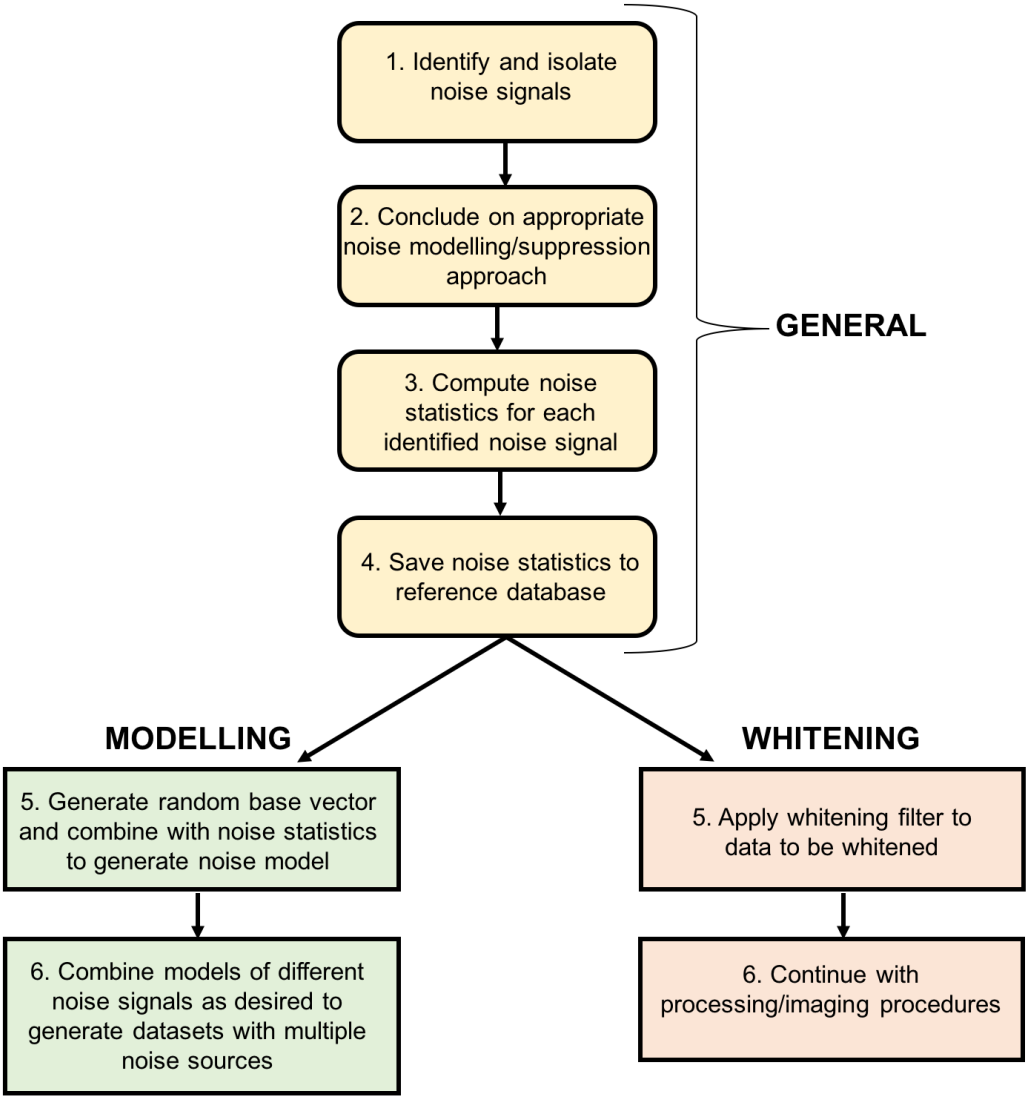

Figure 5.2: *Schematic illustration of the workflow for the implementation of ICOVA noise modelling and whitening.*

containing a large number of noise signals, such as combining a passing car, drill noise and noise from a nearby wind turbine.

For whitening, once the statistics are created, the whitening filter (i.e., the inverse of the lower triangular of the covariance) can be applied to the data to be whitened. This can be applied by one of the three methods described in Chapter 4: IPW, RNW, and RCW. Once the data has been filtered, other noise suppression techniques, in particular random noise suppression procedures, may be applied or the data can be used directly for imaging or inversion.

5.3 Further potential applications

Microseismic surface monitoring has been used in this thesis as the test case for the development and validation of noise modelling and whitening procedures. Although the Aquistore site was particularly suitable due to the permanent receiver locations and the long duration of recording, allowing adequate time to capture the noise statistics, these methods are not strictly valid only for this specific monitoring scenario and they could be easily applicable to other seismic monitoring applications. Ocean Bottom Cable (OBC), for example, presents a strong case for use of this approach, due to the consistent receiver locations: assuming the noise has not drastically changed between recording periods (e.g., a new platform has not been added between surveys), the noise statistics from a baseline survey can be used for subsequent surveys. Figure 5.3 illustrates platform and vessel noise recording on an OBC at the bottom of the North Sea. Due to the repetitive nature of these noise signals they provide a great example of where noise whitening would be effective. Moreover, it is worth noting that with the increased interest in permanent reservoir monitoring systems (*Thompson*, 2017), continuous recording of noise could lead to real time updates of noise statistics and even better noise suppression at various monitoring steps. Other passive monitoring scenarios such as geothermal monitoring, CCS monitoring, and volcanic arrays are all good candidates for both noise modelling and whitening due to their long recording durations.

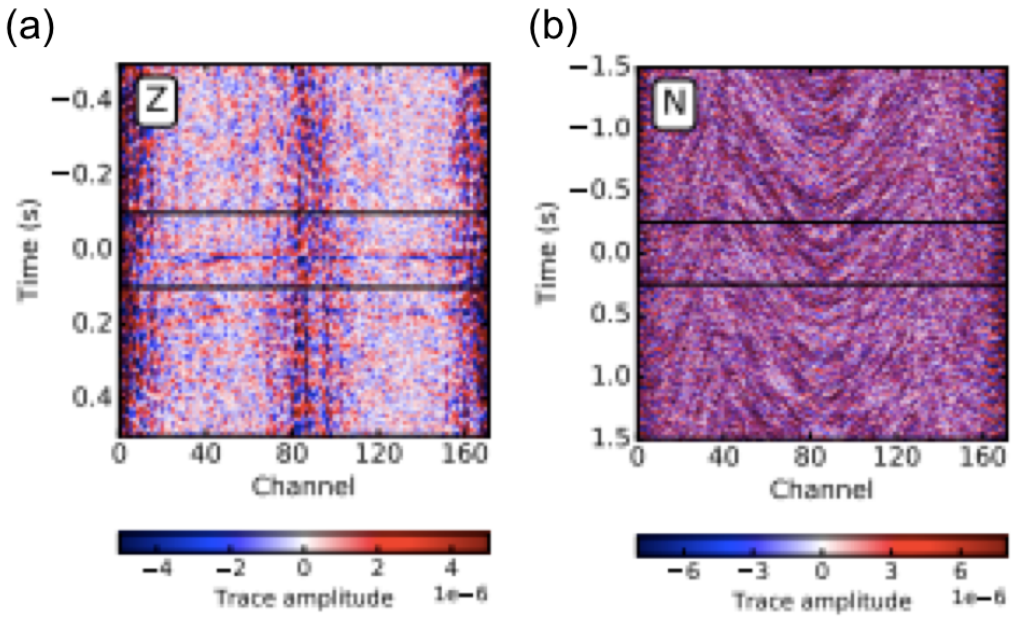

Figure 5.3: *Noise signals from the North Sea attributed to (a) platform noise and (b) vessel noise where the black box denotes a seismic event's arrival (adapted from Dando et al. (2016)).*

Active seismic monitoring typically has much shorter continuous recording periods therefore it may not always be possible to collect noise for a sufficient amount of time to reliably compute the noise statistics from a single recording. Nevertheless, noise realisations collected from multiple recordings could be combined as long as the noise properties are consistent across recordings. Therefore, due to the large number of shots, it may be possible to gather enough noise realisations from the raw data of individual shots. This would be particularly useful at land sites where there are permanent physical bodies creating noise sources, for example a seismic shoot over a producing field with active 'donkey' pumps.

Active marine seismic monitoring poses the additional complication of moving receivers as well as sources. This phenomenon should be for example taken into account when considering coherent noise such as platform noise, which may slide across the various shot gathers as the boat moves towards and away from the platform. I therefore believe that applying the procedure to a test dataset would be the only way to truly evaluate the effectiveness of the noise whitening method for marine seismic recordings .

Finally, it is also important to re-iterate that the noise whitening is not a black-box solution that can always suppress all types of noise, rather an addition to a geophysicist's arsenal of noise suppression tools. Therefore, if the most dominant noise signals are not statistically stationary and randomly varying from recording to recording, whitening alone will not result in a significant gain in SNR.

5.4 Concluding remarks

Perhaps the most significant contribution of my thesis is the development of a noise modelling methodology for the generation of realistic seismic noise models that reject the commonly used WGN assumption. In Chapter 2, a statistical characterisation of the pre-injection noise recorded in the Acquistore site provided the basis for the generation of such noise models. This was accomplished as a filtering process of random samples from a standard normal distribution (i.e., a Gaussian distribution with zero mean and unit variance) using a modelling operator related to the spatio-temporal covariance matrix estimated directly from the recorded noise. Based on the observation that any noise is a filtered version of a white, Gaussian noise, an 'inverse' procedure was proposed in Chapter 4 that is shown to be a robust noise whitening technique, reducing the overall noise energy by a factor of 3.5. Allowing successful imaging of microseismic events at previously undetectable SNRs. On the other hand, Chapter 3 leveraged the ability of the ICOVA methodology to generate as many realizations of noise as desired. This allowed for the first time to statistically analyse the performance of various microseismic event detection and imaging algorithms under realistic noise conditions.

Ultimately, it also provides an opportunity to understand the limitations under which an algorithm performs and to identify pitfalls that arise due to the presence of coherent noise. Whilst the applications illustrated in this thesis have focussed on the surface microseismic monitoring scenario, the methodologies proposed could provide benefits to the majority of array seismology applications, ranging from global to exploration.

References

Birnie, C., K. Chambers, D. Angus, and A. Stork (2016), Analysis and models of pre-injection surface seismic array noise recorded at the aquistore carbon storage site, *Geophysical Journal International*. 5.1, 5.1, 5.1

Dando, B., K. Iranpour, V. Oye, S. Bussat, and L. Bjerrum (2016), Real-time micro-seismic monitoring in the north sea with advanced noise removal methods, in *SEG Technical Program Expanded Abstracts 2016*, pp. 2657–2661, Society of Exploration Geophysicists. 5.3

Galvis, I. S., Y. Villa, C. Duarte, D. Sierra, and W. Agudelo (2017), Seismic attribute selection and clustering to detect and classify surface waves in multicomponent seismic data by using k-means algorithm, *The Leading Edge*, *36*(3), 239–248. 5.1

Huot, F., Y. Ma, R. Cieplicki, E. Martin, and B. Biondi (2017), Automatic noise exploration in urban areas, in *SEG Technical Program Expanded Abstracts 2017*, pp. 5027–5032, Society of Exploration Geophysicists. 5.1

Kabir, M. N., and D. Verschuur (1995), Restoration of missing offsets by parabolic radon transform, *Geophysical Prospecting*, *43*(3), 347–368. 5.1

Li, J., and A. D. Heap (2008), A review of spatial interpolation methods for environmental scientists. 5.1

O'Brien, P. (1974), Aspects of seismic research in the oil industry, *Geoexploration*, *12*(2), 75–96. 5.1

Pearce, R., and B. Barley (1977), The effect of noise on seismograms, *Geophysical Journal International*, *48*(3), 543–547. 5.1

Spitz, S. (1991), Seismic trace interpolation in the fx domain, *Geophysics*, *56*(6), 785–794. 5.1

Sylvette, B.-C., C. Cécile, B. Pierre-Yves, C. Fabrice, M. Peter, K. Jozef, and D. Fäh (2006), H/v ratio: a tool for site effects evaluation. results from 1-d noise simulations, *Geophysical Journal International*, *167*(2), 827–837. 5.1

Thompson, M. (2017), Eage e-lecture: The startup of permanent reservoir monitoring for snorre and grane, E-lecture. 5.3

Wang, J., F. Tilmann, R. White, H. Soosalu, and P. Bordoni (2008), Application of multichannel wiener filters to the suppression of ambient seismic noise in passive seismic arrays, *The Leading Edge*, *27*(2), 232–238. 5.1

Appendix A

Journals' permission and copyright information

- *Geophysical Journal International* (https://academic.oup.com/journals/pages/access_purchase/rights_and_permissions/publication_rights):
  Rights retained by ALL Oxford Journal authors - The right to include the article in full or in part in a thesis or dissertation, provided that this not published commercially;
- *Journal of Applied Geophysics* (https://www.elsevier.com/about/our-business/policies/copyright/permissions):
  Authors can include their articles in full or in part in a thesis or dissertation for non-commercial purposes.
- *Physics of the Earth and Planetary Interiors* (https://www.elsevier.com/about/our-business/policies/copyright/permissions):
  Authors can include their articles in full or in part in a thesis or dissertation for non-commercial purposes.